UNIVERSITY OF BERGEN

MASTER'S THESIS IN PHYSICAL OCEANOGRAPHY

Circulation and Ocean Driven Glacial Melting in a Greenland Fjord

Student

Philipp ANHAUS

Supervisor

Lars Henrik SMEDSRUD

and

Marius ÅRTHUN

November 20, 2017

UNIVERSITY OF BERGEN
GEOPHYSICAL INSTITUTE

Abstract

The Nioghalvfjerdsbræ (79NG) is a floating ice tongue on Northeast Greenland draining a large part of the Greenland Ice Sheet. New hydrographic observations show that Atlantic Water (AW, T > 0 °C, S > 34.3 psu) recirculates across Fram Strait and flow onto the continental shelf having a mean temperature of about 0.6 °C. The AW is steered by complex bathymetry from the shelf toward the main glacier front of 79NG and into the cavity below its 80 km ice tongue. AW presence is documented with a mean maximum temperature of 1.8 °C at 350 m depth in a trough on the continental shelf with a cold halocline layer between 40 m and 100 m. A CTD profile from a rift on the ice tongue close to the northern front of 79NG shows a maximum temperature of approximately 1 °C at 610 m in the cavity. An Ice-Tethered Mooring deployed in the cavity measures velocities between $5\,\mathrm{cm\,s^{-1}}$ - $10\,\mathrm{cm\,s^{-1}}$ over 160 days. Analysis of a Progressive Vector Diagram suggest that the major inflow into the cavity takes place at 250 m and 370 m depth. Further, waters appear to reach the grounding line within 30 days. The mean tidal velocity extracted from these data is with $1.18\,\mathrm{cm\,s^{-1}}$ small. AW present in the cavity most likely drive submarine melting along the ice base. Melt rates are simulated by a 1D numerical Ice Shelf Water plume model. The plume is initiated at the grounding line depth (600 m) and rises along the ice base as a result of buoyancy contrast to the underlying AW. As the plume entrains warm AW ice melts. The plume dynamics and mass, momentum, heat, and salt conservation at the ice-ocean boundary, and, hence, the melting are parameterized using an entrainment coefficient and a drag coefficient. Tides are found neither to influence the plume dynamics nor the melt rates. Maximum melt rates are 50 - $75\,\mathrm{m\,yr^{-1}}$ within 10 km of the grounding line. Within a zone of rapid decay between 10 km and 20 km melt rates drop to roughly $6\,\mathrm{m\,yr^{-1}}$. Further downstream, melting increases again for about 5 km to approximately $15\,\mathrm{m\,yr^{-1}}$ before relatively steady mean melt rates of $6\,\mathrm{m\,yr^{-1}}$ are maintained. Mean and maximum melt rates increase quadratically with rising AW temperatures. The travel time of the plume from the grounding line toward the main glacier front is roughly 9 days. Long-term variability in AW properties are examined using ocean reanalysis (ECCOv4) for 1992-2015. AW temperature and layer thickness in a trough on the continental shelf range between 0.1 °C - 1.3 °C and 45 m - 100 m. Using the simulated range for AW in the plume model gives a range in mean melt rates along the centreline between $10\,\mathrm{m\,yr^{-1}}$ and $19\,\mathrm{m\,yr^{-1}}$. The corresponding freshwater flux ranges between $19\,\mathrm{km^3\,yr^{-1}}$ (0.6 mSv) and $36\,\mathrm{km^3\,yr^{-1}}$ (1.1 mSv).

Acknowledgements

Contents

1. Introduction

In the past two decades the mass loss of the Greenland Ice Sheet (GrIS) has quadrupled (Shepherd et al., 2012). With a total area of $1\,707\,400\,\text{km}^2$ and an ice volume of about $2\,850\,000\,\text{km}^3$, the GrIS has a sea level rise potential of about $7\,\text{m}$ (Warrick et al., 1996; Reeh et al., 1999). From 1992-2000 to 2000-2011 the mass loss increased from $51\pm65\,\text{km}^3\,\text{yr}^{-1}$ to $211\pm37\,\text{km}^3\,\text{yr}^{-1}$ (Shepherd et al., 2012). In form of freshwater this accounts for about one quarter ($7.5\,\text{mm}$) of the total global sea level rise - an alarming number (Church et al., 2011). Causes of the enhanced mass loss are found in increased surface melt, and retreat and speed up of marine-terminating glaciers (Enderlin et al., 2014). The amount of freshwater that enters the ocean triggers changes in the estuarine circulation in the adjacent fjords, glacier dynamics, the marine ecosystem, and atmospheric temperatures (Bamber et al., 2012). It is expected that even the large scale ocean circulation might be impacted (Bamber et al., 2012; Straneo and Cenedese, 2015). The pathways through which the ice and freshwater are channeled and finally reach the ocean are the marine-terminating glaciers of Greenland which are an important interface between the GrIS and the surrounding ocean. According to Enderlin et al. (2014), 15 of the largest glaciers are responsible for 50 % of the mass loss. It is most likely that increased submarine melting of the glaciers are a result of a warming ocean and higher air temperatures and contributes significantly to the mass loss (Straneo and Heimbach, 2013). Many of these marine-terminating glaciers drain into fjords where they interact with the ocean (Straneo and Cenedese, 2015). Due to melting the glaciers retreat and the ice flow accelerates (Straneo and Heimbach, 2013). The net mass loss is believed to be directly caused by the retreat of the outlet glaciers due to melting at grounding line depth (Thomas et al., 2009). Melting at this point leads to an inward migration of the grounding line and an accelerated transport of the glaciers (Thomas et al., 2009). Thus, it has become important to study the causes and consequences of the GrIS mass loss and the submarine melting of Greenland′s marine-terminating glaciers.

In this study, submarine melting of one of Greenland′ major marine-terminating glaciers is investigated. The Nioghalvfjerdsbræ (also referred to as 79 North Glacier, hereafter 79NG) is a $80\,\text{km}$ long (Schaffer et al., 2017) floating ice tongue located in Northeast Greenland. It drains into Nioghalvfjerdsfjorden. Its terminus is separated by land which causes it to split into

two glacier fronts (Thomsen et al., 1997). The main front which is about 30 km wide stretches toward east whereas a smaller front about 8 km wide (Schaffer et al., 2017) terminates north in a neighboring, narrow fjord termed Dijmphna Sund. Wilson et al. (2017) find that 79NG is subject to the highest melt rates of the remaining ice tongues in Greenland. This place it into the focus of recent studies not only because its retreat will cause major changes in buttressing the Northeast Greenland Ice Stream (NEGIS).

79NG is one of three marine-terminating glaciers of the NEGIS (Fahnestock et al., 1993). NEGIS drains a very large area of the GrIS, about half of the northern sector (Wilson and Straneo, 2015). The bedrock of the system is below sea level for about 150 km inland from the coast (Thomas et al., 2009). This makes the system vulnerable to submarine melting, fast retreat, and destabilization.

It is hypothesized that warm and salty Atlantic Water (AW) present in the cavity below the floating ice tongue of 79NG drives melting along the ice base. Freshwater released at depth stems mainly from surface runoff and subglacial discharge that drains through the glacier via a channelized network. Due to the density contrast between the freshwater and the AW a plume evolves that rises along the ice base entraining AW which drives melting producing cold, fresh, and buoyant Ice Shelf Water (ISW). This water mass contributes to the estuarine fjord circulation. Wilson and Straneo (2015) and Schaffer et al. (2017) suggest that AW flows into the cavity via the main glacier front. In the cavity, AW is modified due to melting and subglacial discharge. The outflow is believed to take place via the main front and the northern front toward Dijmphna Sund (Wilson and Straneo, 2015). From there, portions of the freshwater might drain into the East Greenland Current (EGC) and is transported further south to areas where dense bottom waters are formed, e.g., Greenland Sea, Irminger Sea, and Labrador Sea. Anomalous high amounts of freshwater can alter this formation. Dense water formation plays a key role in the thermohaline circulation which transports mass, momentum, heat, salt, and nutrients along the Atlantic Ocean, into and from the Arctic and Southern Ocean.

The main goal of this study is to improve our understanding of the processes involved in submarine melting and to quantify melt rates in order to asses the stability of the 79NG ice tongue. This includes AW circulation and variability across Fram Strait, at the continental shelf of Northeast Greenland, and in cavity below the 79NG ice tongue. The focus lies on the evolution and dynamics of a buoyant plume and associated melt rates.

The scientific background needed to perform the addressed study is outlined in Chapter 2. The data and methods used to carry out this work are presented in Chapter 3. Results of new hydrographic data, a 1D ISW plume model to simulate melt rates, and variability in melting due to AW temperature and layer thickness variations are covered in Chapter 4. This follows by a discussion in Chapter 5. Chapter 6 aims to give a conclusion and suggest future work that can be done to improve our understanding of the considered topics.

2. Background

2.1 Atlantic Water Circulation and Variability

A potential driver for submarine melting of Greenland's marine-terminating glaciers is warm and saline AW. It is plausible that melt rates are controlled by the variability in both AW temperature and volume (layer thickness). Therefore, it is relevant to investigate the circulation, the properties, and both the inter-annual and decadal fluctuations of AW.

The circulation pattern of AW is determined by the northernmost extension of the Gulf Stream, the North Atlantic Current. AW flows trough the Nordic Seas, northward toward the Fram Strait, and finally into the Arctic Ocean (Beszczynska-Möller et al., 2012; Årthun and Eldevik, 2016) (Figure 2.1). The Nordic Seas consist of the Iceland Sea, the Norwegian Sea, and the Greenland Sea. Beszczynska-Möller et al. (2012) define AW being warmer than 2 °C which is present roughly between 50 m and 750 m with the AW core at about 250 m. As AW flows from the North Atlantic through the Nordic Seas, passing Fram Strait, into the Arctic Ocean it loses heat toward the atmosphere and due to contact with sea ice. Mean AW temperatures are indicated by numbers in Figure 2.1.

According to Orvik and Niiler (2002) and Beszczynska-Möller et al. (2012), the North Atlantic Current splits into a western and an eastern branch before it enters the Nordic Seas (Figure 2.1). The western branch enters the Nordic Seas through the channel between Iceland and the Faroe Islands. Due to its baroclinic component, the current is steered along the front between AW and Polar Water (PW) which coincides roughly with the winter sea ice extent (not shown, Årthun and Eldevik (2016); Beszczynska-Möller et al. (2012)). It is termed the Norwegian Atlantic Front Current (NwAFC). As Beszczynska-Möller et al. (2012) suggest, this current flows along the Mohn Ridge and the Knipovich Ridge. Before this limb reaches north of Spitsbergen, a part recirculates westward towards the continental shelf of Northeast Greenland south of Molloy Hole at roughly 78 °50′N (Beszczynska-Möller et al., 2012). The observations are based on moorings and supported by Hattermann et al. (2016) using a combined eddy-resolving regional ocean model (high-resolution Svalbard 800 m model, S800-model, and a coarser 4 km Arctic setup, A4-model) together with trajectories of neutrally buoyant floats and mooring data.
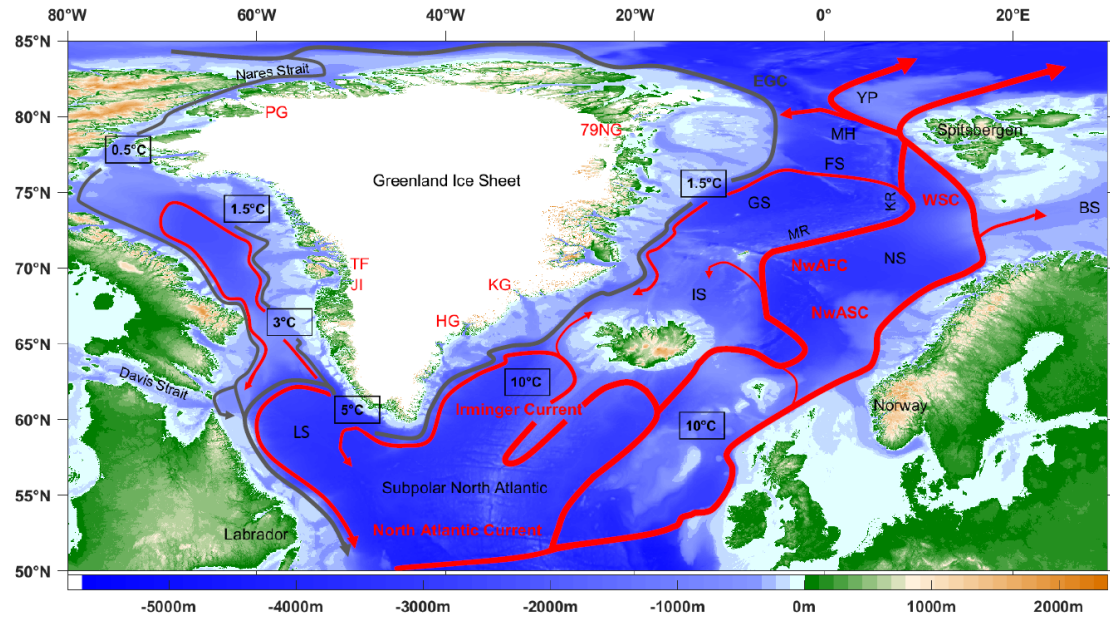
Figure 2.1: *Schematic of the Atlantic Water (AW, red) and Polar Water (PW, gray) circulation in the North Atlantic and Nordic Seas, and partly in the Arctic Ocean (Orvik and Niiler, 2002; Beszczynska-Möller et al., 2012; Straneo and Cenedese, 2015; Årthun and Eldevik, 2016; Schaffer et al., 2017). Currents transporting AW are indicated red: North Atlantic Current, Irminger Current, Norwegian Atlantic Slope Current (NwASC), Norwegian Atlantic Front Current (NwAFC), and West Spitsbergen Current (WSC). The East Greenland Current (EGC) transporting PW is indicated gray. Numbers show the mean AW temperature circulating offshore (Straneo et al., 2012). The black abbreviations indicate seas: Labrador Sea (LS), Iceland Sea (IS), Norwegian Sea (NS), Greenland Sea (GS), Barents Sea (BS), Fram Strait (FS). Topographic features are marked black: Mohn Ridge (MR), Knipovich Ridge (KR), Molloy Hole (MH), and Yermark Plateau (YP). The red abbreviations mark the locations of six major marine-terminating glaciers of the Greenland Ice Sheet: Petermann Glacier (PG), 79 North Glacier (79NG), Kangerdlugssuaq Glacier (KG), Helheim Glacier (HG), Jakobshavn Isbræ (JI), and Torssukatak Fjord (TF) (Straneo et al., 2012; Straneo and Cenedese, 2015). The bedrock is the RTopo2 (Schaffer et al., 2016).*

The eastern branch access the Nordic Seas between the Faroe Islands and the Shetland Islands and follows the bathymetry along the continental shelf of Norway as the Norwegian Atlantic Slope Current (NwASC) contributing the areas temperate climate. Hattermann et al. (2016) state that the current follows f/H contours owing its strong barotropic component, where f is the Coriolis parameter and H the depth of the water column. Further downstream, north of terrestrial Norway, the NwASC divides into an eastern part entering the Barents Sea and another part which flows northward along the west coast of Svalbard as the West Spitsbergen Current (WSC). The WSC confluences with the NwAFC further north. Two smaller parts of the WSC enter the Arctic Ocean crossing the Yermark Plateau whereas the largest part recirculates north of Molloy Hole (Hattermann et al., 2016) at about 80 °N.

The results of the eddy-resolving ocean model yield considerable details and partly new insights

into the recirculation pathways of AW in Fram Strait. In this aspect, the westward transport of AW is found to be associated with eddies. To examine the connection between westward flow and the eddy transport, Hattermann et al. (2016) calculated the difference between the mean kinetic energy (MKE) and the eddy kinetic energy (EKE). As a conclusion, MKE is responsible for a northward transport of AW towards the Arctic Ocean and EKE causes the flow to recirculate westwards. It is thus commonly accepted that these westward pathways are possible and fairly probable processes explaining how AW flow toward and onto the continental shelf of Northeast Greenland and to 79NG.

The two AW recirculation pathways originate from different water masses (Hattermann et al., 2016). The waters carried within the northern recirculation pattern are simulated to be warmer and saltier than the waters in the southern branch related to the faster WSC which lead to a reduced heat loss to the atmosphere. Both the southern and northern recirculation pattern merge with the southward flowing EGC (Figure 2.1). The EGC is guided along the continental shelf of East Greenland. It carries cold and fresh PW at the surface originating in the Arctic Ocean, modifications of AW due oceanic heat loss and freshwater input in the Arctic Ocean, and glacial modified water from marine-terminating glaciers (De Steur et al., 2014). Further, it acts as a surface and subsurface barrier restricting AW flow onto the continental shelf of Northeast Greenland.

Both the AW temperatures and the volume transport are of great importance to be able to determine submarine melt rates of marine-terminating glaciers. Årthun and Eldevik (2016) modeled the ocean heat content and found that anomalies are mainly transported poleward along the AW pathway. Further, Hátún et al. (2005) and Årthun and Eldevik (2016) conclude that changes in the Subpolar Gyre lead to variability in temperature and volume of the inflowing AW and, thus, in the poleward heat transport.

Beszczynska-Möller et al. (2012) describes the variability of AW temperature using mooring data for the period 1997-2012. The maximum temperature of 4.4 °C is found offshore Spitsbergen between the surface and 150 m (Figure 2.2). This is consistent with results from the S800-model simulating temperatures above 4 °C at 250 m (Hattermann et al., 2016). The mean temperature found by Beszczynska-Möller et al. (2012) is 3.1 ± 0.1 °C. AW cools across Fram Strait toward the continental shelf of Northeast Greenland. The recirculation across Fram Strait is evident in the westward extension of temperatures higher than 2 °C between 300 m and 400 m (Figure 2.2). The decrease in temperature toward west is, according to Beszczynska-Möller et al. (2012), explained by mixing of AW with PW of Arctic origin transported southward by the EGC.

AW temperature and temperature anomalies vary both in space and time on monthly and inter-annual scales (Figure 2.3) (Beszczynska-Möller et al., 2012). Two periods of intensified warming and spreading were observed (Figure 2.3a). In late 1999-2000 AW reached as far as 4 ° west and confluenced with the EGC. Between late 2004 and 2008 AW warmed and advanced
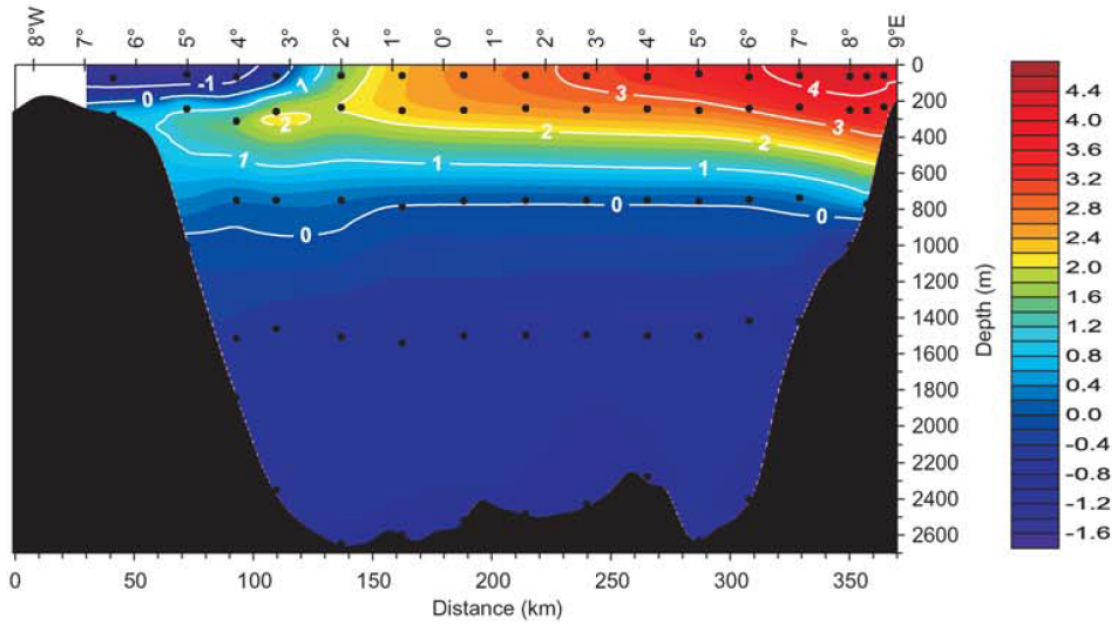
Figure 2.2: Mean AW temperature in °C across Fram Strait based on mooring data for the period 1997-2012. Gray shading is the bedrock (Beszczynska-Möller et al., 2012).

greatly. During this period AW reached as far west as the continental shelf of Northeast Greenland.

An alternating pattern of cold and warm periods in the temperature anomaly is clearly evident (Figure 2.3b). The positive western anomaly in late 2005/2006 close to the continental shelf of Northeast Greenland (3° to 6° west) is separated from the anomaly further east. This indicates that the western anomaly stems from the recirculation north of rather than south of Molloy Hole as the eastern one does (Beszczynska-Möller et al., 2012).

2.2   Glacier Mass Balance

Until the 1990s the GrIS was relatively stable (Bamber et al., 2012). However, since then the total freshwater discharge, both in solid and liquid form, has accelerated with an alarming rate and rose above $3200 \pm 358 \, \text{km}^3$ ($101.4 \pm 11.3 \, \text{mSv}$) since 1995 (Bamber et al., 2012). Since 2002, the monthly freshwater flux has increased by $0.1 \, \text{Sv}$ (Figure 2.4). The yearly increase in the freshwater flux since 1992 is estimated to $16.9 \pm 1.7 \, \text{km}^3 \, \text{yr}^{-1}$ ($0.5 \pm 0.1 \, \text{mSv}$) and, by 2003, to about $1\,200 \, \text{km}^3 \, \text{yr}^{-1}$ ($38.0 \, \text{mSv}$) which corresponds to an increase of 39 % per year.

 Freshwater discharge is not evenly spread around the GrIS, but rather concentrated through major marine-terminating glaciers (Figure 2.1). These glaciers drain into fjords and channel large volumes of freshwater into the ocean.

The following explanation of the glacier mass balance is mainly adopted from Benn and Evans
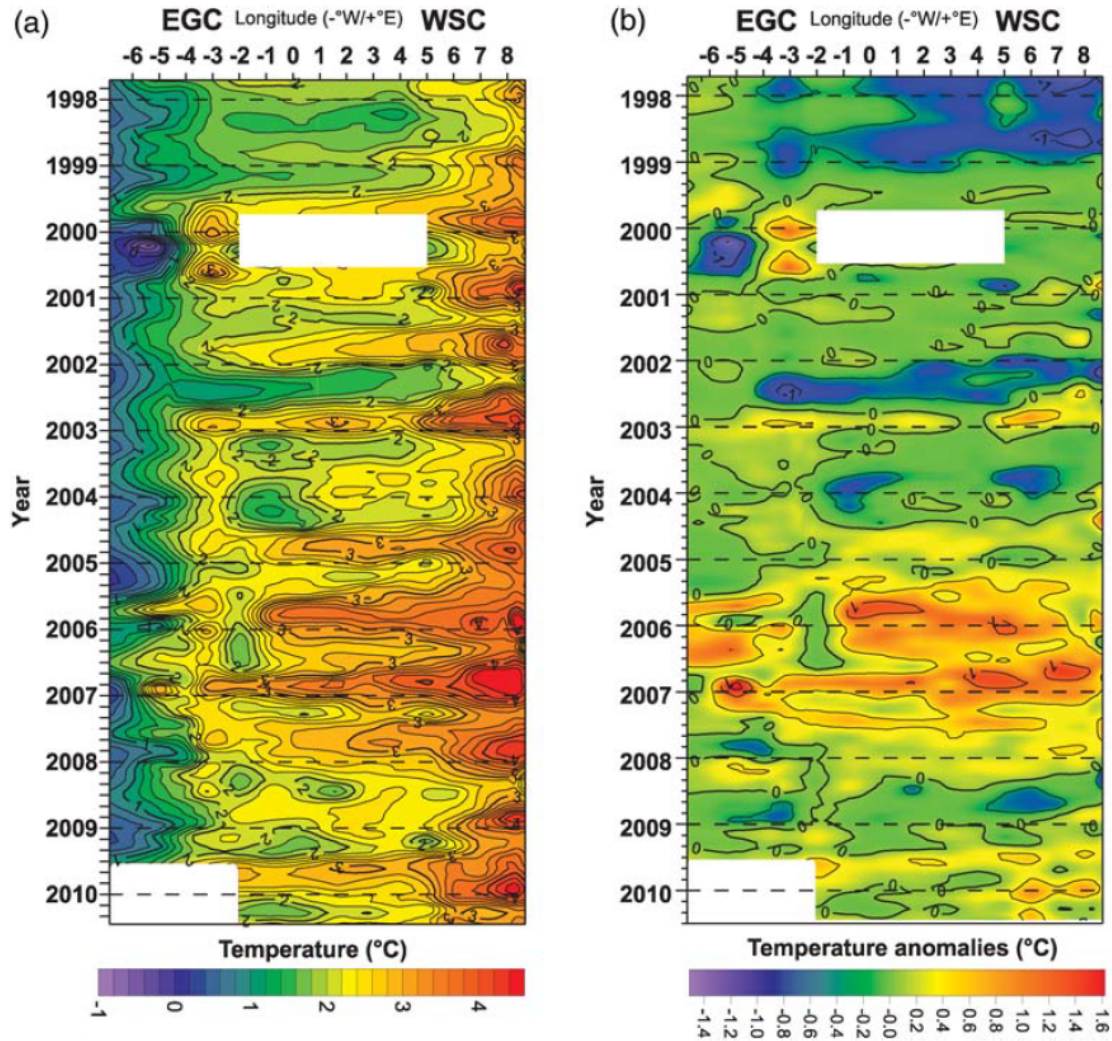
Figure 2.3: *Monthly mean (a) temperatures at 250 m and (b) temperature anomalies across Fram Strait between 1997-2012 from mooring data. The white rectangles indicate periods with no mooring data available (Beszczynska-Möller et al., 2012).*

(2010). Glaciers are constantly in exchange with the atmosphere, hydrosphere, and lithosphere. They gain and lose mass. Mass gain is accomplished by ice flow from upstream, snowfall and precipitation (if air temperatures are below zero), and basal freezing. Mass loss is due to surface and basal melting, and calving at the glacier front. Many marine-terminating glaciers in North and Northeast Greenland have floating extensions referred to as ice tongues. The mass budget of such a glacier is defined as follows, assuming steady state:

$$0 = BMB + SMB + GLF - CF, \quad\quad\quad (2.1)$$

where BMB is the basal mass balance, SMB the surface mass balance, GLF the grounding line flux, and CF the calving flux (Figure 2.5) (Depoorter et al., 2013). Steady state means that mass
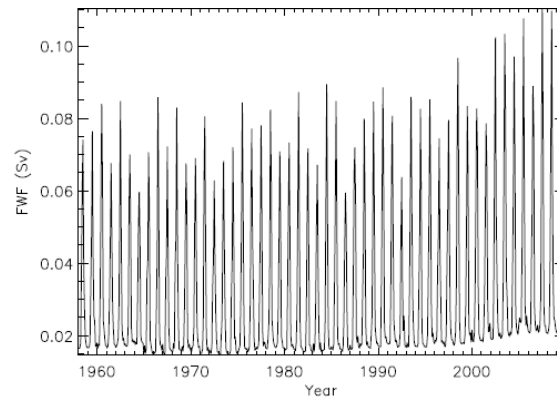
Figure 2.4: Total monthly freshwater flux (FWF) for the Greenland Ice Sheet in Sv between 1958 and 2010 (Bamber et al., 2012).

loss is exactly compensated for by mass gain.

Surface melting occurs mainly in summer due to solar radiation, and precipitation and snow fall if surface temperatures are above zero and is referred to as surface runoff (Figure 2.5). Basal melting occurs at the glacier bedrock due to friction between ice flow and bedrock and due to geothermal heating. Surface runoff and basal meltwater drains through the hydrologic network of the glacier and are released at the grounding line (Das et al., 2008; Chu et al., 2009). It is referred to as subglacial discharge.

The point where the ice goes afloat and is not grounded anymore is termed the grounding line (Figure 2.5). It is a very dynamic area and not a rigid line, and responds simultaneously to the dynamics of the ocean, e.g., tides. The grounded ice, the ice tongue, and the bedrock create a cavity that is filled with water. Ice tongues located in the high latitudes experience large snow accumulation due to low air temperatures and a generous moisture source supplied by the ocean. On the other hand, surface melting is enhanced because ice tongues are in general fairly flat. This results in large areas of melt ponds which have a low albedo and absorb shortwave radiation very effectively which in turn leads to even stronger melting. Basal melting and freezing along the ice base of an ice tongue is referred to as submarine melting and freezing (Figure 2.5). Thomsen et al. (1997) propose that submarine melting may contribute significantly to the overall mass balance of marine-terminating glaciers. An ice tongue is highly variable and susceptible to atmospheric and oceanic forces and changes. Freezing along the ice base is related to the pressure and salinity dependence of the freezing point of sea water. The freezing point decreases with both pressure and salinity. Due to the density contrast between cold and fresh subglacial discharge and warm and salty AW present in the cavity a buoyant plume evolves that rises along the ice base. As the plume advances to shallower depth the pressure reduces and, hence, the freezing point increases which lead to freezing and accumulation along the ice base. In contrast, even water that is at the freezing point at the surface can melt ice
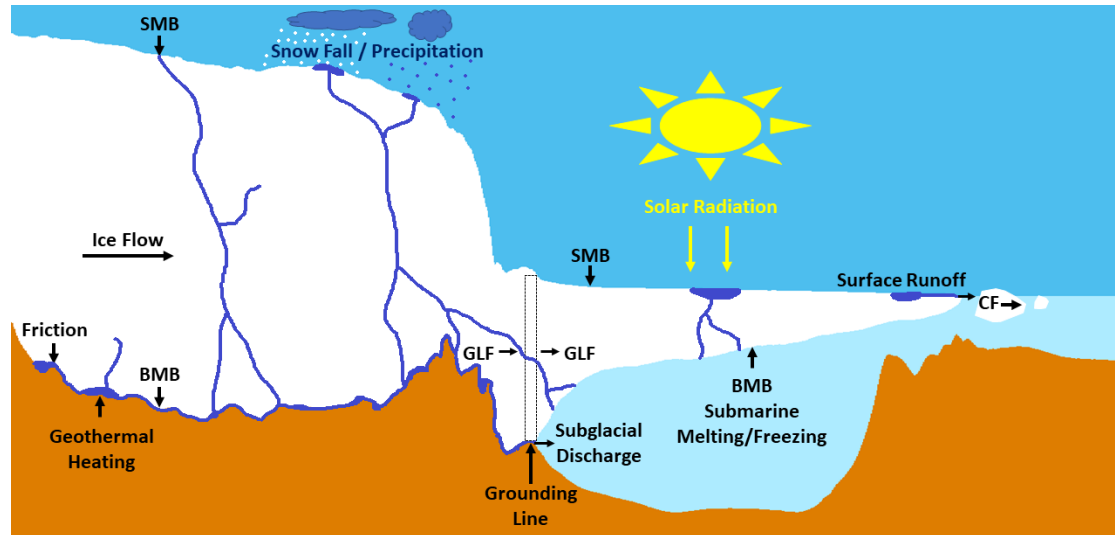
Figure 2.5: Part of the Northeast Greenland Ice Stream (NEGIS) draining into the Nioghalvfjerdsfjorden as the 79NG (Figure 2.1). The geometry is from RTopo2 (Schaffer et al., 2016). BMB, basal mass balance. SMB, surface mass balance, GLF, grounding line flux, CF, calving flux.

underneath an ice tongue as its freezing point is decreased due to pressure. Therefore, the water is warmer than the ice temperature and drives melting. In this process, cold, fresh, and buoyant Ice Shelf Water (ISW) is formed. It is noteworthy that freezing along an ice base in Greenland is not observed due to the present of very warm AW and relatively short ice tongues (Kimura S. (2017), personal communication). The lateral margins of the fjords act to resist ice flow from upstream. As a result, the ice flow is concentrated along the centre of an ice tongue. Ice tongues themselves counteract ice flow and, thus, provide an additional buttressing effect. Moreover, sea ice in front of ice tongues protect them from calving Reeh et al. (2001).

2.3   Fjord Circulation and Plume Dynamics

The following description of the circulation in Greenland fjords aims to give insights into the processes related to submarine melting. It is mainly adopted from Straneo and Cenedese (2015). The circulation is affected by tides, buoyancy forcing from the glacier and icebergs, surface fluxes, local winds (along-/across-fjord winds), and eddies.

Greenland fjords are generally filled with a three- or four-layered water column. Cold and fresh PW is present at the surface overlying warm and salty AW. In addition, one or two very cold and fresh layers exist that are well-mixed in temperature. These consist of surface runoff, subglacial discharge, and/or submarine meltwater (Figure 2.6). Surface runoff entering the fjord surface creates a very fresh and cold layer overlying PW (Figure 2.6). As the plume that evolves
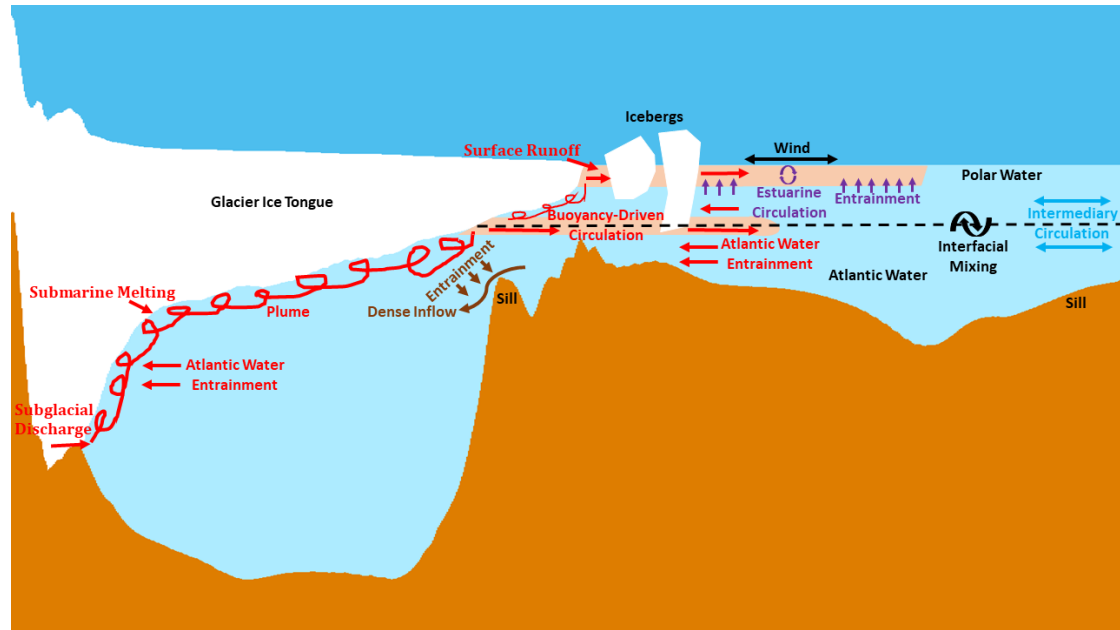
Figure 2.6: *Schematic representation of the circulation in a Greenland fjord with a marine-terminating glacial ice tongue. Red indicates the buoyancy-driven circulation resulting from surface runoff, subglacial discharge, and submarine melting, purple indicates the estuarine circulation resulting from surface runoff and winds, blue indicates the intermediary circulation, and pink indicates the circulation generated by the dense inflow over the sill. Figure modified from Straneo and Cenedese (2015).*

due to a density contrast rises along the ice base, AW is entrained which drives submarine melting. The resulting meltwater maintains this buoyancy-driven circulation. Depending on the amount of subglacial discharge and submarine melting and, hence, on the buoyancy, the plume reaches its level of neutral buoyancy at some depth or outcrops at the surface. In both cases, the plume detaches from the glacier, and flows into the fjord. Assuming that subglacial discharge is released at multiple channels would lead to several interacting plumes and to a strong 3D circulation. The presence of subglacial discharge and surface runoff is a summer phenomenon. In winter, only submarine melting exists (Straneo et al., 2011). Consequently, plume dynamics, entrainment (Cenedese and Linden, 2014), and, hence, submarine melting vary seasonally (Xu et al., 2013; Kimura et al., 2014). Farther downstream the system reduces to a two layer circulation with PW on top and AW below.

Most of Greenland fjords have deep laying sills (Figure 2.6). Above these sills intermediary flows evolve. They have their nature described by density fluctuations originating outside the fjord. The density fluctuations can result from along-shore winds (upwelling or downwelling) or density anomalies advected across the fjord mouth. Depending on the width of the fjord, a geostrophic flow influenced by rotational effects (wide) or a vertically sheared flow across the fjord (narrow) adjusts. It is crucial for the fjord dynamics and the water properties that intermediary circulations are able to flush the entire fjord waters and change the properties on

different time scales from daily to subseasonally (Aure et al., 1996).

Depending on whether the sill is located above or below the interface between AW and PW, the exchange of these water masses happens without any barrier and can be associated with intermediary circulations. On inter-annual time scales, changes may be driven by advection of shelf conditions (Jackson et al., 2014). This most likely also affects both submarine melting and freshwater outflow (Sciascia et al., 2014).

The renewal of deep water across the sill is strongly connected to a reverse inflow of dense water from the continental shelf. Coupled to this is entrainment of fresher water from above (Figure 2.6). The residence time of deep water depends on mixing, the intermediary circulation, and the volume of water for nonglacial fjords (Stigebrandt, 2012). In contrast, for fjords which are filled by marine-terminating glaciers the time depends also on subglacial discharge and submarine melting. This would result in shorter renewal time because of entrainment of deep water into the plumes.

An additional freshwater source is iceberg melting. Iceberg meltwater can stay subsurface when the icebergs are deep, e.g., below the PW-AW interface.

Surface runoff, turbulent mixing caused by winds, and tides drive an estuarine circulation (Figure 2.6). Mixing of freshwater downwards leads to entrainment of denser water from below. This results in a denser (mostly saltier) subsurface layer below the freshwater outflow.

Numerical model results dictate that the submarine melt rates are positive correlated to the AW temperature and subglacial discharge (Jenkins, 2011; Sciascia et al., 2013; Xu et al., 2013). In contrast, Jenkins (1991) and Holland et al. (2007) find a quadratic dependence of the melt rates to the AW temperature. Thus, melt rates and their variation in space and time are highly sensitive to the model parameterizations and to the external forcings.

Entrained AW warms the ice to its in-situ freezing point along the ice-ocean boundary (Figure 2.6. Heat conducted into the ice leads to melting. As a result, more freshwater is added to the plume, increases its buoyancy, and, hence, accelerates it.

If the plume is sufficiently buoyant to overcome the background stratification it reaches the surface where it outcrops. Otherwise it stops ascending when its level of neutral buoyancy is reached. Independent from the height the plume achieves, it then separates from the glacier and flows horizontally into the AW layer and away from the glacier as a buoyancy-driven current (Figure 2.6). Entrainment of AW into the plume leads to a slow stream of ambient waters directed toward the glacier.

The subglacial discharge is released either by a localized, point source (e.g., a channel, Figure 2.7a) or a distributed, line source (e.g., a crack extending along the glacier front/grounding line, Figure 2.7b). Xu et al. (2013) investigated the response of submarine melting to subglacial discharge released at the ice-ocean boundary of Store Glacier as a point source using the MITgcm (Massachussets Institute for Technology General Circulation Model). Increasing the
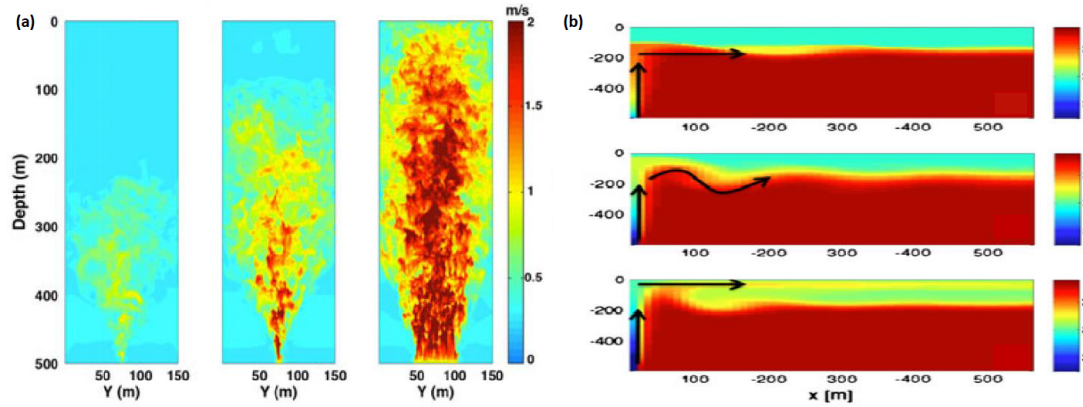
Figure 2.7: *(a) 3D simulations (MITgcm) of vertical plume velocity in m s^{-1} with varying subglacial discharge (small to large - left to right) and channel geometry at Store Glacier (Xu et al., 2013). (b) 2D simulations (MITgcm) of plume salinity in psu with varying subglacial discharge (small to large - top to bottom) at Helheim Glacier (Sciascia et al., 2013).*

subglacial discharge ($1\,\mathrm{m^3\,s^{-1}}$, $5\,\mathrm{m^3\,s^{-1}}$, $30\,\mathrm{m^3\,s^{-1}}$) leads to a faster and more vigorous plume (Figure 2.7a). Submarine melt rates increased with the subglacial discharge.

Sciascia et al. (2013) found that increasing the subglacial discharge causes the plume to penetrate progressively closer to the surface (Figure 2.7b). Also, the mean and maximum submarine melt rate increased with the subglacial discharge applying values of $0.74\,\mathrm{m^3\,s^{-1}}$, $5.8\,\mathrm{m^3\,s^{-1}}$, and $8.7\,\mathrm{m^3\,s^{-1}}$ at Helheim Glacier released as a line source. The salinity distribution and the plume height were calculated for a two-layer stratification. If the plume density between PW and AW is lower than the density of PW the plume reached the surface. If the plume density is greater than the density of PW, the plume reaches its level of neutral buoyancy at a certain depth in the water column.

2.4   NEGIS and 79NG

The NEGIS (Figure 2.8 left, black box) drains about half of the northern sector of the GrIS (Wilson and Straneo, 2015). Rignot and Kanagaratnam (2006) quantifies the drainage basin of NEGIS to be more than 15 % of the GrIS. From its summit of about 2 500 m NEGIS flows toward the coast traveling more than 300 km (Thomsen et al., 1997; Thomas et al., 2009). It connects with the ocean via three marine-terminating glaciers which are 79NG, Zachariæ Isstrøm, and Storstrømmen (Fahnestock et al., 1993) (Figure 2.8 inlet). The glaciers serve as conduits for the drainage of NEGIS (Roberts D. (2017), personal communication). Discharge of the NEGIS into the ocean is mainly controlled by 79NG and neighbored Zachariæ Isstrøm (Jenkins, 1991; Thomsen et al., 1997; Reeh et al., 1999, 2001; Schaffer et al., 2017). This is about 198 380 km^2 in
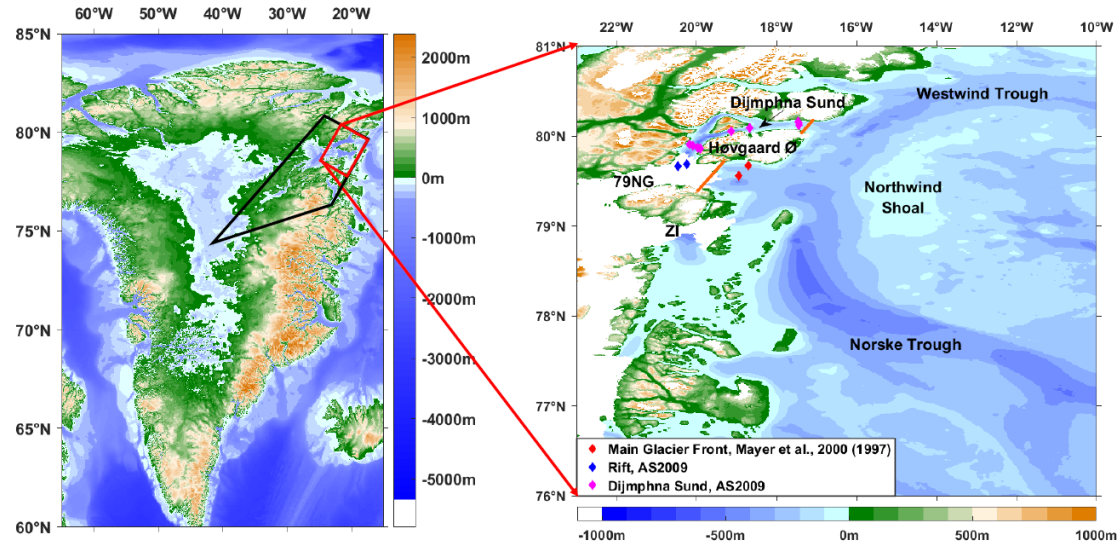
Figure 2.8: *Bedrock map showing the location of NEGIS (black box), 79NG, and Zachariæ Isstrøm (ZI) (red box and inlet). The bedrock is from the RTopo2 data set from Schaffer et al. (2016). CTD stations from previous cruises are indicated by colored diamonds. Red lines indicate transects showing bedrock, ice elevation, and ice base as illustrated in Figure 2.10*

area which is 12 % of the GrIS (Rignot and Mouginot, 2012). 79NG alone drains about 8.4 % of the GrIS (Jung-Rothenhäusler, 1998).

The 79NG is with its 80 km length (Schaffer et al., 2017) the largest floating ice tongue in Greenland (Wilson et al., 2017). Its grounding line is at about 600 m depth (Mayer et al., 2000; Wilson and Straneo, 2015; Schaffer et al., 2017). It drains into Nioghalvfjerdsfjorden which is 20 km wide for about two thirds of its upper extent. The lower one third is about 30 km wide. An island termed Høvgaard Ø separates the ice tongue into two glacier fronts (Figure 2.8 inlet). The main front which is about 30 km wide stretches toward east. A smaller front about 8 km wide (Reeh et al., 2001; Schaffer et al., 2017) terminates north in a neighboring, narrow fjord termed Dijmphna Sund. Most observations from the 79NG area are conducted in summer/autumn. During the field work performed by Thomsen et al. (1997) and Mayer et al. (2000) Dijmphna Sund was mostly free from sea ice. In contrast, a permanent fast-ice cover is present just off the main front (Reeh et al., 2001; Straneo et al., 2012; Wilson and Straneo, 2015). The bedrock along the NEGIS is below sea level for roughly 150 km upstream of the grounding line of 79NG (Figure 2.5 and 2.8) (Thomas et al., 2009). This makes the NEGIS particularly susceptible to a collapse if the ice tongue of 79NG might destabilize or even melt down completely. The floating ice tongue of Zachariæ Isstrøm completely melted between fall 2012 and spring 2015 (Mouginot et al., 2015). This implies that the area is subject to rapid changes (Wilson et al., 2017). Increased submarine melting was also observed at 79NG, however, it is currently pinned to islands at the main front (Figure 2.8 inlet) (Thomsen et al., 1997; Reeh

et al., 2001). Also, its mass balance seem to remain relatively stable (Mouginot et al., 2015; Schaffer et al., 2017). In addition, 79NG is hooked at the lateral margins counteracting the ice flow from upstream. Paleoclimatic studies suggest that 79NG reached further east in the past (Figure 2.8 inlet) (Roberts D. (2017), personal communication). It is furthermore concluded from these studies that the shallow Northwind Shoal might have been a pinning point. During the Holocene, 79NG started becoming ungrounded and retreating toward its current pinning point leading to a shoaling of the Northwind Shoal as result of isostatic rebound (Roberts D. (2017), personal communication). At present, the grounding line of 79NG is farthest west than ever before (Roberts D. (2017), personal communication). It is believed that the deglaciation of 79NG was caused by marine/submarine melting. 79NG will retreat rapidly given further melting at the grounding line and the retroshaped/downsloped bedrock (Figure 2.5) (Plach A. (2017), personal communication). However, further upstream the bedrock progressively increases which might stop further retreat and be the next pinning point of 79NG.

2.4.1 Hydrography

AW recirculates in Fram Strait and flows onto the continental shelf of Northeast Greenland (Figure 2.1). A C-shaped trough system exists in front of 79NG (Figure 2.1 and 2.8 inlet). It is divided into the northern Westwind Trough and the southern Norske Trough (Wilson and Straneo, 2015). AW cannot access the Westwind Trough directly from its recirculation pathway north of Molloy Hole as the continental shelf break is too shallow at this location (Schaffer et al., 2017) (Figure 2.1). From there, AW flows southward and enters the trough system via Norske Trough together with AW recirculating south of Molloy Hole. Many studies found that AW is present on the continental shelf at depth. It underlies a shallow layer of cold and fresh PW which originates in the Arctic Ocean and is carried onto the continental shelf by the EGC (Mayer et al., 2000; Wilson and Straneo, 2015; Schaffer et al., 2017).

Schaffer et al. (2017) and Wilson and Straneo (2015) conclude that the warmest AW that flows toward 79NG originates in the Norske Trough in the south. From there it flows toward the main front and into the cavity beneath the 79NG ice tongue. AW warmer than $1\,°C$ and similar characteristics as the recirculating AW are present in Norske Trough below $200\,m$ (Wilson and Straneo, 2015; Schaffer et al., 2017). It is transported toward the main front of 79NG within a boundary current along the northeastern slope of Norske Trough (Schaffer et al., 2017).

Wilson and Straneo (2015) and Schaffer et al. (2017) suggest that AW enters the cavity beneath the 79NG ice tongue through the main front in the east (Figure 2.9). In more detail, Schaffer et al. (2017) propose that AW enters the cavity via a $370\,m$ deep channel which was detected in seismic reflections (Mayer et al., 2000) and CTD profiles. The RTopo2 data along the main front (Schaffer et al., 2016) reveal shallower depth as deep as $340\,m$ (Figure 2.10a).
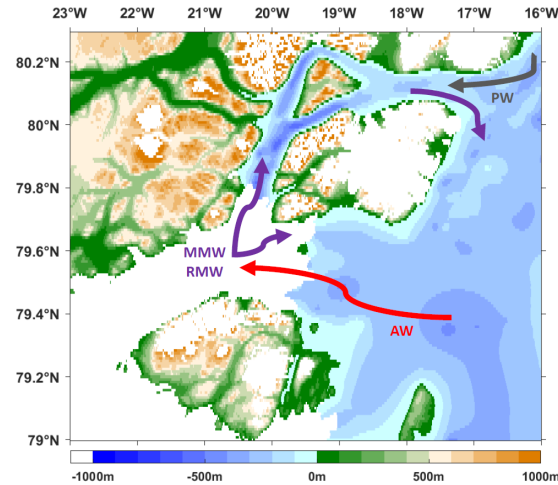
Figure 2.9: *Overview map of the circulation at 79NG and in the cavity beneath its ice tongue as suggested by (Wilson and Straneo, 2015). Red arrows: Atlantic Water (AW), purple: glacial meltwater-modified water (MMW) and glacial runoff-modified water (RMW), gray: Polar Water (PW). The bedrock is the RTopo2 data set from Schaffer et al. (2017).*
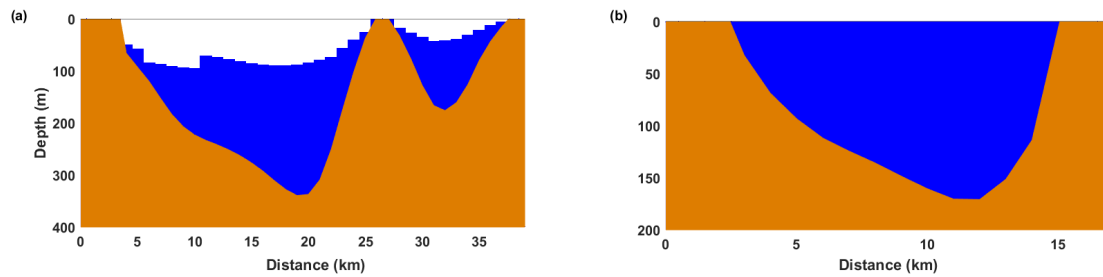
Figure 2.10: *Transverse profiles of bathymetry at selected locations at 79NG area. (a) Main front and (b) Dijmphna Sund Mouth. The profiles are indicated by red lines in Figure 2.8 (inlet). The bathymetry is the RTopo2 (Schaffer et al., 2016).*

AW with mean maximum temperatures of $1\,°C$ at $320\,m$ depth are detected at the main front (Schaffer et al., 2017). Selected CTD profiles (Mayer et al., 2000) show a layered water column (Figure 2.11). Cold and fresh water is present in the uppermost $50\,m$. Below, a cold mixed layer is found with temperatures close to freezing. In contrast, the salinity increases with depth which might either indicate a cold halocline or a mixture of PW and submarine meltwater (Mayer et al., 2000). Between $100\,m$ and $150\,m$, the temperature and salinity increase with depth. The selected profiles do not show the presence of AW because they were taken at too shallow depth. However, Mayer et al. (2000) also present profiles reaching deeper in the water column revealing AW (not shown).

Schaffer et al. (2017) further propose that AW is blocked by a sill just east of Høvgaard Ø (Figure 2.8). This prevents an exchange between the water in Norske Trough and Westwind Trough. Wilson and Straneo (2015) support this finding who found AW in the Norske Trough
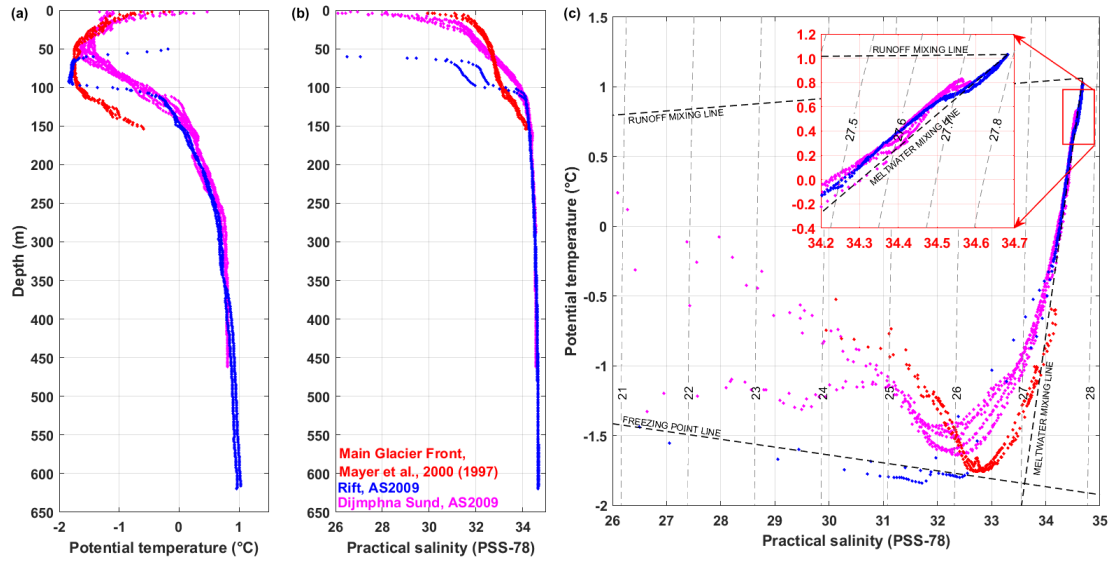
Figure 2.11: *Potential temperature (a) and salinity (b) as a function of depth for profiles close to the main front (red, Mayer et al. (2000)), in a rift 15 km upglacier from the northern terminus (blue, Wilson and Straneo (2015)), and in Dijmphna Sund (yellow, Wilson and Straneo (2015)). (c) Potential temperature versus salinity diagram for the same stations. Density ($\sigma_0 = \rho_0$ - 1000 kg m^{-3}) lines are drawn every 1 kg m^{-3}. The freezing point temperature referred to the surface pressure is indicated by the dashed black line. The meltwater mixing line connects the densest and warmest AW found in the rift profiles (T = 1.0 °C, S = 34.68 psu) and the effective ice properties (T* = -92.8 °C, S$_i$ = 0 psu, Eq. 3.26). The mixture of ambient water and glacial runoff fall along the runoff mixing line with the runoff temperature and salinity being T = 0 °C and S = 0 psu (Straneo et al., 2012). The inlet shows an expanded view presenting the deepest water masses. The locations of the profiles are shown in Figure 2.8 (right).*

to be warmer and saltier than in Westwind Trough.

CTD profiles were taken in a rift on the ice tongue close to the northern terminus and in Dijmphna Sund during a survey in September 2009 with M/V Arctic Sunrise (AS2009 hereafter) (Wilson and Straneo, 2015). The data reveal the presence of AW as warm as 1 °C in the cavity (Figure 2.11). The water properties are very similar to these detected in Norske Trough (Wilson and Straneo, 2015) which support the suggested flow of AW into the cavity (Figure 2.9). As in most Greenland fjords the water column exhibits a multiple layer system with cold and fresh PW at the surface, very cold water subsurface exhibiting a strong stratification, and AW at depth.

Once in the cavity, AW is believed to drive submarine melting along the ice base due to presence of glacial meltwater-modified water which fall along the meltwater mixing line (Figure 2.11). This line connects the warmest AW (S = 34.68, T = 1.0 °C) with the effective ice properties (S$_i$ = 0, T$_i^*$ = -92.8 °C).

The runoff mixing line connects AW with surface runoff and/or subglacial discharge (T = 0 °C, S = 0 psu) (Figure 2.11). The water in the cavity is veered against the runoff mixing line

(Figure 2.11 inlet) suggesting the presence of a mixture between AW and surface runoff and/or subglacial discharge which is referred to as glacial runoff-modified water (Wilson and Straneo, 2015).

Observations indicate increasing AW temperatures (Beszczynska-Möller et al., 2012; Onarheim et al., 2014). This may lead to enhanced submarine melting and a complete collapse of the 79NG ice tongue and, thus, destabilizing NEGIS.

Wilson and Straneo (2015) propose that glacial meltwater-modified water and glacial runoff-modified water rise along the ice base due to their high buoyancy and leave the cavity through the main front in the east and via the northern front entering Dijmphna Sund (Figure 2.9). Glacial meltwater-modified water and glacial runoff-modified water are present at depth in Dijmphna Sund which support the suggested circulation. Moreover, Wilson and Straneo (2015) find that AW temperatures deep in the cavity are warmer than in Djimphna Sund (Figure 2.11 inlet). Thus, they hypothesize that the AW present in the cavity originates from the warmer water in Norske Trough rather than from water in the Westwind Trough which is colder (not shown). This supports once again that AW enters the cavity via the main front. Also, the bathymetry at the northern front is sufficient deep to allow a such a pathway (Figure 2.10c). In addition, Wilson and Straneo (2015) tracked a sill along Dijmphna Sund with a maximum depth of about 170 m which has the potential to block the inflow of AW from the Westwind Trough. The bathymetry across the mouth of Dijmphna Sund from the RTopo2 data confirm the presence of the sill (Figure 2.10d). PW that originates in the Arctic Ocean and is carried by the EGC onto the continental shelf and finally into Dijmphna Sund is present at the surface (Figure 2.11).

2.4.2 Melting

Dynamic changes of 79NG and Zachariæ Isstrøm might spread toward the interior of the GrIS via NEGIS and affect the mass balance (Thomsen et al., 1997).

Many independent studies confirm that the 79NG ice tongue is thinning. The major contribution is submarine melting along the ice base. Thomas et al. (2009) derived surface elevation changes from laser altimeter data collected during aircraft flights along 79NG and Zachariæ Isstrøm for the periods 1994-1999 and 1999-2007. Partly rapid thinning caused by changes in glacier dynamics are found along Zachariæ Isstrøm. The surface of 79NG lowered at rates of about $0.1\,\mathrm{m\,yr^{-1}}$ for the period 1994-1999. Further inland the net change is almost nil. The data for 1999-2007 show an increased thinning of about $0.3\,\mathrm{m\,yr^{-1}}$ up to 150 km along the flight line, partly being as high as 0.5 - $1\,\mathrm{m\,yr^{-1}}$. This is consistent with surface ablation rates found by Thomsen et al. (1997) measuring ice fluxes across 79NG. Assuming steady state, hydrostatic equilibrium, and using a simple ice-flux model, the net balance yield submarine melting of

Mean submarine melt rate m yr^{-1}	Maximum submarine melt rate m yr^{-1}	Mean surface melt rate m yr^{-1}	Inflowing ice flux km^3 yr^{-1}	Submarine melt flux km^3 yr^{-1}	Reference
4 - 5	-	1	-	-	Thomsen et al. (1997)
8	40	1.2	15	11.2	Mayer et al. (2000)
-	-	0.5 - 1	-	-	Thomas et al. (2009)
-	50 - 60	1.5	10.2 $\pm$ 0.59	11.9 $\pm$ 0.96	Wilson et al. (2017)

Table 2.1: *Melt rates and ice fluxes at the 79NG ice tongue.*

about 4 - 5 m yr^{-1}. Thomsen et al. (1997) and Straneo and Cenedese (2015) propose that submarine melting is the largest contribution in the mass balance of 79NG.

Mayer et al. (2000) quantified the mean submarine melt rate of 79NG to roughly 8 m yr^{-1} using the continuity equation, mean ice thicknesses from seismic reflections, and velocities obtained from GPS stake measurements. Strongest melting is found close to the grounding line with up to 40 m yr^{-1}.

Wilson et al. (2017) present submarine melt rates retrieved from ice flux divergence calculations using ice thickness change from digital elevation models and ice velocities from optical feature tracking in the continuity equation for the period 2011-2015. Largest melt rates occur close to the grounding line being about 50 - 60 m yr^{-1}. They decay rapidly within 15 km down-glacier from the grounding to about 15 m yr^{-1}. Further downstream, the melt rates decrease to near zero. Wilson et al. (2017) further computed the ice volume flux across the grounding line which is lower than the observed total melt flux (surface and submarine) indicating net melting (Table 2.1).

3. Data and Methods

3.1 Conductivity Temperature Depth (CTD)

CTD data were obtained during a research cruise to Fram Strait and 79NG in August/September 2016 (FS2016 hereafter). The cruise was organized by the Norwegian Polar Institute on R/V Lance. A Sea-Bird 9plus CTD was used together with a Sea-Bird 11plus V2 Deck Unit. The system is referred to as SBE 911plus (Sea-Bird Electronics, 2015). It was calibrated for the last time December 19, 2015. The CTD was incorporated into an array of 11 Niskin bottles. The rosette was lowered on a hydrographic wire at a descend rate of ideally $1\,\mathrm{m\,s^{-1}}$. The sampling were done with $24\,\mathrm{Hz}$. Temperature (SBE 3plus premium Temperature sensor) and conductivity (SBE 4C Conductivity sensor) are measured upstream of a channel through which water flows (Sea-Bird Electronics, 2015). The flow rate is controlled by an integrated SBE 5T pump. The advantage is that spiking of salinity is reduced due to a slower flow rate and a more constant time response from the sensor. This improves the resolution, particularly in wavy conditions. Moreover, the natural flow is not disturbed. As a consequence, the dynamic accuracy is improved and small scale structures can be resolved (Sea-Bird Electronics, 2015). The pressure was measured with a digiquartz pressure sensor. Additionally, one conductivity and one temperature sensor were connected to the CTD rosette. A mounted TS duct assures that temperature and salinity are measured for the same water parcel. To avoid the instrument colliding with the sea floor or any obstacles, a bottom contact switch was installed. The Sea-Bird 11plus V2 Deck Unit allows for real-time data acquisition and control. On a screen the collected data can be visualized and monitored during the descent. This ensures that the Niskin bottles can be manually closed at predefined depths and instrument failure can easily be detected.
The data were processed using SBE Data Processing software (Software Version Seasave V 7.21b). Only the data measured during the downcast were used. Output variables used in this study include pressure, temperature, and conductivity. Pressure was low-pass-filtered (Butterworth) with a time constant of $0.15\,\mathrm{s}$. Salinity was low-pass-filtered using a time constant of $0.03\,\mathrm{s}$. The filter smoothes high frequency (rapidly changing) data to prevent time shifting (Sea-Bird Electronics, 2015). For temperature no filtering was performed. Aligning the CTD

Water Masses	Abbreviation	Potential temperature (°C)	Salinity (psu)
Polar Surface Waters	PSW	< 0	< 34.3
Polar Surface Waters warm	PSWw	> 0	< 34.3
Modified Atlantic Waters	MAW	< 0	> 34.3, < 34.8
Atlantic Waters	AW	> 0	> 34.3
North Atlantic Deep Water	NADW	< 0	> 34.8

Table 3.1: Water mass definition used in this study.

parameters in time makes sure that calculations, e.g. of salinity, are made using measurements from the same water parcel. Conductivity values were primary and secondary corrected for the cell thermal mass using the same parameters for the thermal anomaly amplitude of $\alpha = 00.3$ and for the time constant of $1/\beta = 7$. As a result, salinity accuracy can be better than 0.01 psu. Subsequently, by executing loop editing, scans are marked where the CTD rosette is moving less than minimum velocity (0.25 cm s^{-1}) or is traveling backwards due to ship roll (Sea-Bird Electronics, 2015). Bad scans are excluded from further processing. The window size was set to 300 s. Using conductivity, temperature, and pressure practical salinity and density were computed. The data were then averaged into pressure bins with a bin size of 1 m. The surface bin was included. Water sampling was done (if applicable) with a SBE 17plus V2 Searam bottle firing system (917plus). Summarizing the bottle .ros files and storing the data in .btl files is the last step in the processing procedure. Doing so, Seasave averages the desired input variables as well as variables that has to be derived from other parameters.

The measurement range for conductivity is 0 to 7 S m^{-1} and for temperature -5 to 35 °C. The accuracy of the conductivity sensor is ± 0.0003 S m^{-1} and for the temperature sensor ± 0.001 °C (Sea-Bird Electronics, 2015). The time response of both the temperature and conductivity sensor is 0.065 s.

The CTD stations are grouped into sections defined by geographic features (Figure 3.1): Fram Strait (magenta), Continental Shelf (blue), Norske Trough (orange), Dijmphna Sund (red), Westwind Trough (green).

Validation of the CTD profiles were done by comparing salinity values obtained from the CTD with values from the Niskin bottles measured by a Portasal 8410A salinometer manufactured by OSIL. The CTD measured 1 s before and after bottles were closed to allow for nearly direct comparison. The comparison shows good agreement (Figure 3.2) and no significant pressure trend.

Water masses and their properties are presented in Table 3.1. In TS-space the observed water masses are illustrated in Figure 3.3. In this study, the main focus is on the AW properties.
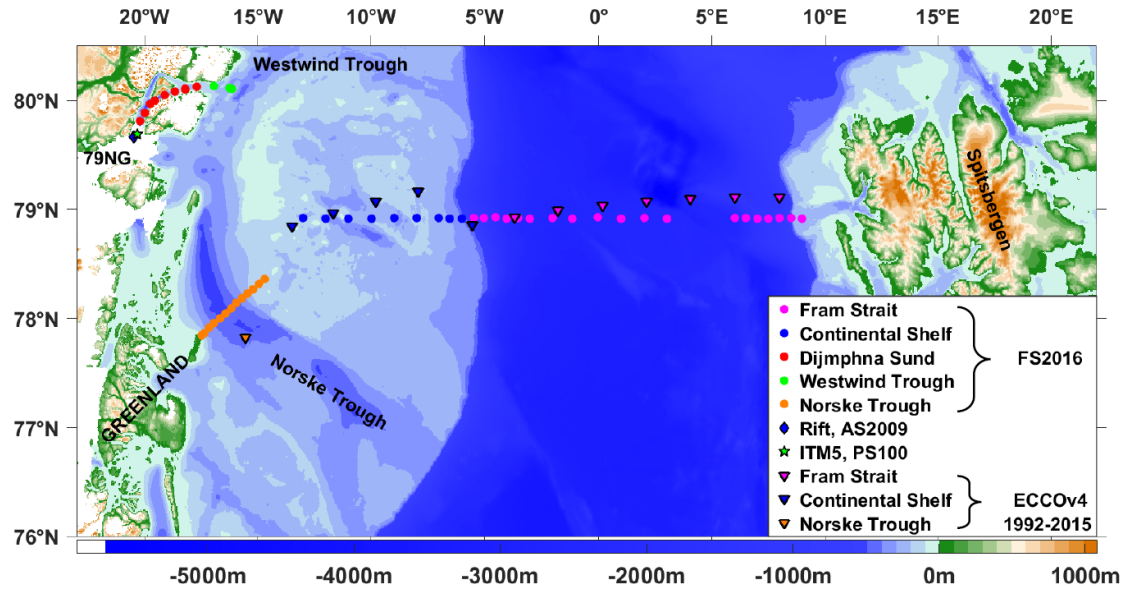
Figure 3.1: *Overview map of the location of all hydrographic data collected during FS2016 and previous surveys.*
FS2016: Fram Strait (magenta), Continental Shelf (blue), Norske Trough (orange), Dijmphna Sund (red), Westwind
Trough (green). Wilson and Straneo, 2009: Rift (blue). Straneo et al., 2016: Ice-Tethered Mooring (ITM5, blue).
Estimating the Circulation and Climate of the Ocean version 4 state estimate and ocean model (ECCOv4) September
1992-2015: Fram Strait (magenta), Continental Shelf (blue), Norske Trough (orange). Bedrock and surface mask are
the RTopo2 (Schaffer et al., 2016).

Therefore, it is worth mentioning its definition in more detail. Originally, it was tried to define
AW by density as suggested by Rudels et al. (2002) and Schaffer et al. (2017). In this case, AW
would lie between the $27.70 \, \text{kg} \, \text{m}^{-3}$ and $27.97 \, \text{kg} \, \text{m}^{-3}$ isopycnals (referenced to the surface).
However, using the practical salinity as a criterion together with the potential temperature
yields a more clear distinction in the study area. Hence, AW is defined as being warmer than
$0 \, °\text{C}$ and saltier than $34.30 \, \text{psu}$.

3.2   Ice-Tethered Mooring (ITM) and Tidal Analysis

An Ice-Tethered Mooring (ITM) was deployed in a rift 15 km upglacier from the northern
terminus of the 79NG ice tongue on August 23, 2016 during the PS100 cruise on R/V Polarstern
(Figure 3.1). Four aquadopp single-point current profiler from Nortek AS are attached to the
mooring line at initial depths of about 165 m, 250 m, 370 m, and 500 m. The aquadopps are
equipped with transducers that transmit acoustic pulses in different, but known directions. The
pulses are reflected at suspended particles and sent back to the device with a shift in sound
frequency (Doppler shift). The velocity of the particle can be derived by solving
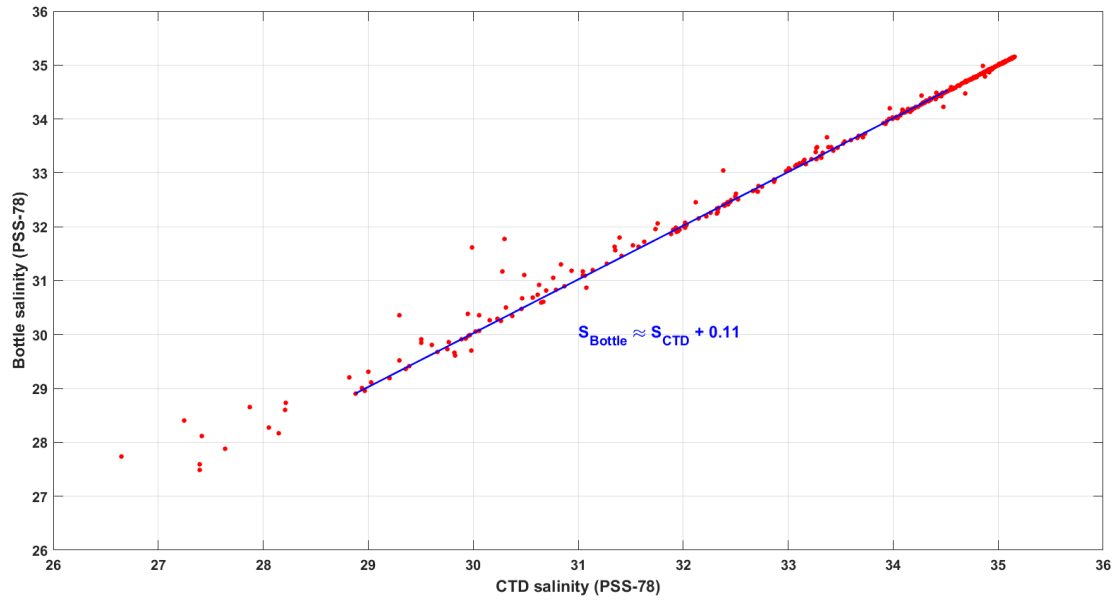
Figure 3.2: Salinity measurements from the CTD plotted against the salinometer results from the Niskin bottles.
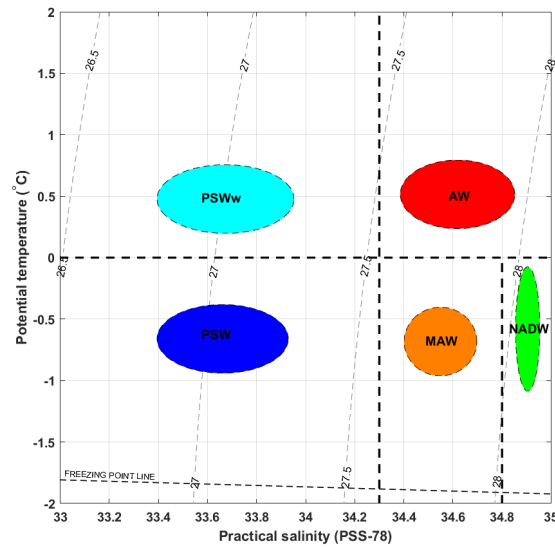
Figure 3.3: Potential temperature versus salinity diagram illustrating the waters masses used in this study. Density ($\sigma_0 = \rho_0 - 1000\,kg\,m^{-3}$) lines are drawn every $0.5\,kg\,m^{-3}$. Water mass properties are presented in Table 3.1. The freezing point temperature referred to the surface pressure is indicated by the dashed black line. Polar Surface Water (PSW) is marked blue, Polar Surface Water warm (PSWw) is marked light blue, Modified Atlantic Water (MAW) is marked orange, Atlantic Water (AW) is marked red, and North Atlantic Deep Water (NADW) is marked green.

Tide	Description	Frequency (cph)
O1	Principal lunar declinational	0.0387307
K1	Sun-Moon angle, diurnal	0.0417807
N2	Principal lunar elliptic, semidiurnal	0.0789992
M2	Principal lunar, semidiurnal	0.0805114
S2	Principal solar, semidiurnal	0.0833333

Table 3.2: The 5 most important tidal constituents at 79NG area resolved by the harmonic tidal analysis following Pawlowicz et al. (2002).

$$f = \frac{c + v_r}{c + v_s} \cdot f_0, \tag{3.1}$$

for the particle velocity v_s which is equal to the current velocity. f_0 is the frequency of the sound wave emitted by the transducers, f the frequency of the reflected sound wave, c the velocity of the sound waves in water, and v_r the velocity of the instrument relative to the suspended particles.

The range in velocity is $\pm 500 \, \text{cm s}^{-1}$ and accuracy $\pm 0.5 \, \text{cm s}^{-1}$ (Nortek AS, 2013). Measurements are averaged over 15 min. The data were collected and made available by the Ice-Tethered Profiler Program (Toole et al., 2006; Krishfield et al., 2008) based at the Woods Hole Oceanographic Institution (http://www.whoi.edu/itp). Raw data show very good agreement with the data visualized by the WHOI group. Moreover, tides are fairly barotropic which indicates good quality of the data (Section 4.2.2).

Tidal velocities are relevant to describe the processes in the cavity below the 79NG ice tongue. These are calculated from the ITM5 using the harmonic analysis package T_{tide} (Pawlowicz et al., 2002). The period October 21, 2016 to January 18, 2017 was extracted which gives a record length of 89.3 days, sufficient to detect all tidal constituents. Recorded data used in this study are zonal (U) and meridional (V) velocities. 35 tidal constituents are considered listed in order of predefined importance based on the equilibrium response method. The 5 most relevant components and their frequencies are presented in Table 3.2. The frequencies are known from astronomical parameters and based on sums and differences of integer multiplies of 6 basic frequencies (Pugh and Woodworth, 2014). In the T_{tide}, tides are modelled using sums of complex amplitudes at these distinct frequencies expressed as

$$x(t) = b_0 + b_1 t + \sum_{k=1,\ldots,N} a_k e^{i\sigma_k t} + a_{-k} e^{-i\sigma_k t}. \tag{3.2}$$

The requisite is a time series of current observations y(t) which is treated by the program as vectors of the form u + iv. N is the number of constituents used each with a frequency σ_k. a_k is a complex amplitude and the complex conjugate of a_{-k}. t is time, and the terms b_0 and $b_1 t$ represent possible offset and linear drift. The modelled tidal forcing is fit (least-square) along

sinusoidal functions using

$$E = \sum_m |x(t_m) - y(t_m)|^2 = ||Ta - y||^2,$$ (3.3)

where y = [y(t$_1$),y(t$_2$),...,y(t$_M$)]′, a = [b$_0$,b$_1$,a$_1$,a$_{-1}$,a$_2$,a$_{-2}$,...,a$_{-N}$]′, and T is an M x 2N + 2 matrix of linear and sinusoidal functions.

The tidal flow was calculated as the root mean square (rms) of the u$_T$ and v$_T$ tidal components using

$$\sqrt{\langle U_T^2 \rangle} = \sqrt{u_T^2 + v_T^2}.$$ (3.4)

U$_T$ is the tidal flow magnitude and the angle brackets indicate a temporal mean.

3.3 Refined Topography 2 (RTopo2)

Bedrock, ice elevation, and ice base are adopted from the recently published Refined Topography 2 (RTopo2) data set (Schaffer et al., 2016). The origin of the data set is the RTopo1 (Timmermann et al., 2010). The horizontal resolution was increased from 1 min to 30 s. In contrast to RTopo1, RTopo2 includes representation of the GrIS and its marine-terminating glaciers. RTopo2 is interpolated, smoothed, and, if applicable, replaced with appropriate artificial values (Schaffer et al., 2016). To create this data set a variety of resolutions, projections, and coverages as well as sampling periods were merged.

The General Bathymetric Chart of the Oceans (GEBCO 2014) and the International Bathymetric Chart of the Arctic Ocean version 3 (IBCAOv3) were merged. GEBCO 2014 is derived from ship depth soundings and satellite-derived gravity data (Weatherall et al., 2015). The digital bathymetric product IBCAOv3 is a combination of multibeam, dense single beam, and surface height data with a horizontal resolution of 500 m x 500 m. On the continental shelf, data are sparse due to less ship traffic and partly due to ice cover. Therefore, other data sets with different resolutions, projections, and coverages were included (Schaffer et al., 2016). For example, surface elevations from the Greenland Ice Mapping Project and ice thicknesses from airborne altimeter surveys (Bamber et al., 2013), and satellite-derived ice motion data (Morlighem et al., 2014). The combination of these products result in improvements of the resolution of fjord structure. Schaffer et al. (2016) combined the best parts of each data set to obtain the most realistic representation. The especially bad representation of the continental shelf of Northeast Greenland is to some extent overcome by feeding a high-resolution digital bathymetry model with reprocessed and combined multi- and single-beam echosoundings from more than two decades and maximum depths from CTD profiles (Arndt et al., 2015).

In particular, the ice base of the 79NG ice tongue is derived from seismic, airborne, and radar surveys (Mayer et al., 2000; Schaffer et al., 2016). The ice elevation is calculated from the ice
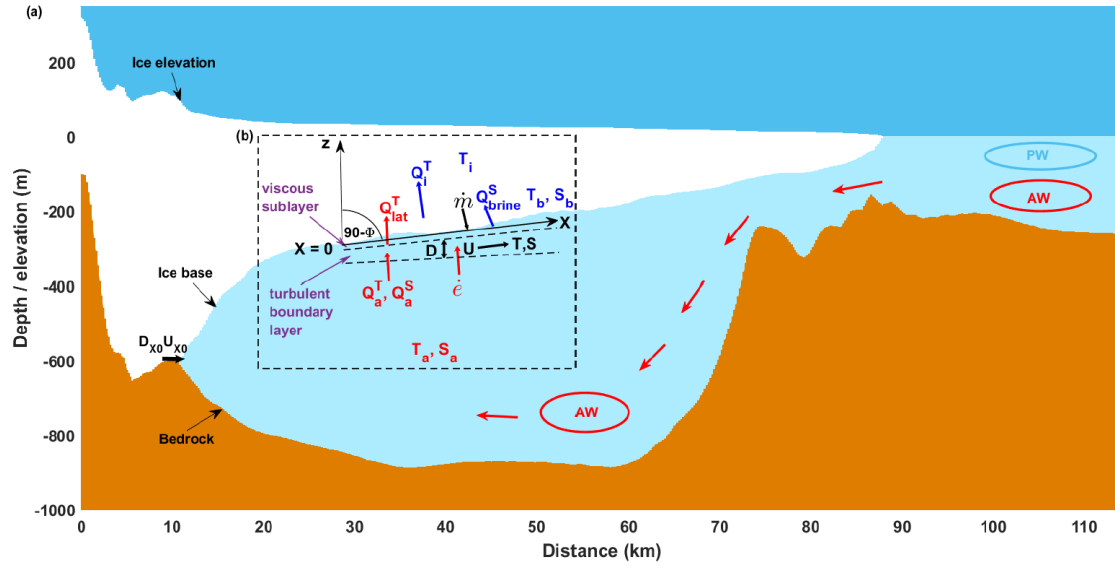
Figure 3.4: *(a) Schematic representation of bedrock, ice elevation, and ice base along the centreline of the 79NG ice tongue from RTopo2 (Schaffer et al., 2016). The line is marked cyan in Figure 3.5. The data were smoothed using a moving average fit with a horizontal footprint of about 1.1 km. (b) Illustration of an evolving plume circulation along the ice base modified from a general description by Jenkins (2011). Subglacial discharge $D_{X0}U_{X0}$ is released at the grounding line depth. The representation of heat and salt fluxes at the ice-ocean boundary is adopted from Holland and Jenkins (1999). The plume variables are defined in Section 3.5.*

thickness exploiting hydrostatic equilibrium (Schaffer et al., 2016).

Bedrock, ice elevation, and ice base along the centreline of the 79NG ice tongue with extension inwards from the grounding line and seawards from the main front is illustrated in Figure 3.4a. The ice base of 79NG is shown in Figure 3.5

High resolution bedrock data are crucial to investigate AW flow onto the continental shelf of Northeast Greenland, towards the 79NG ice tongue along the trough system and into the cavity below. The realistic representation of the ice base is necessary to allow for an enhanced resolution of the ice-ocean boundary and, thus, for a proper simulation of the submarine melt rates and plume dynamics.

The global sphere is divided into 360 deg, 1 deg is 60 min, 1 min is 60 s. 30 s are about 930 m of latitude and longitude at the equator. However, polewards 1 s of longitude decreases with the cosine of latitude. In case of the 79NG ice tongue which centreline follows roughly the 79.5°N latitude 30 s of longitude are approximately 170 m. The spherical grid of RTopo2 in the area considered is thus 170 m x 930 m (Figure 3.6) which gives a mean horizontal footprint of about 550 m.

The horizontal distance between data points along the flow line was equally spaced. It is defined according to the length of the ice tongue and the number of data points for the ice base achieved following the 80 km long flow lines (Figure 3.5). For example, along the centreline
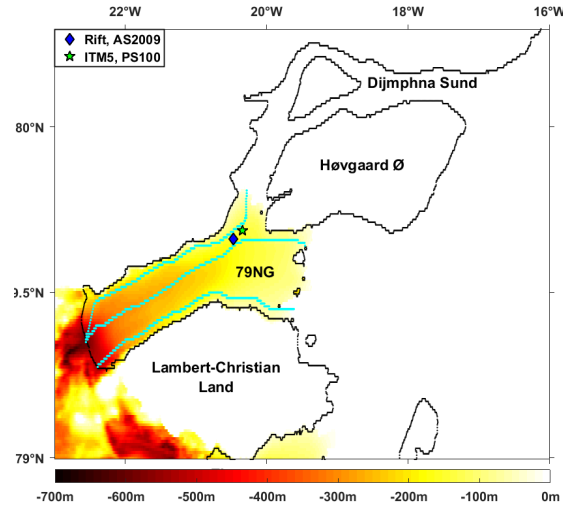
Figure 3.5: *Ice base in m from RTopo2 Schaffer et al. (2016). Cyan flow lines mark the pathways for which plumes were simulated using the 1D ISW plume model (Section 3.5).*

371 data points were manually extracted and sorted monotonically decreasing. This yield a horizontal spacing of about $80\,000\,\text{m}/371 = 216\,\text{m}$. Subsequently, the ice base was smoothed applying the moving average method to every 5th data point introducing a horizontal footprint of about 1.1 km. However, the 1DISW plume model uses a higher resolution for solving the equations.
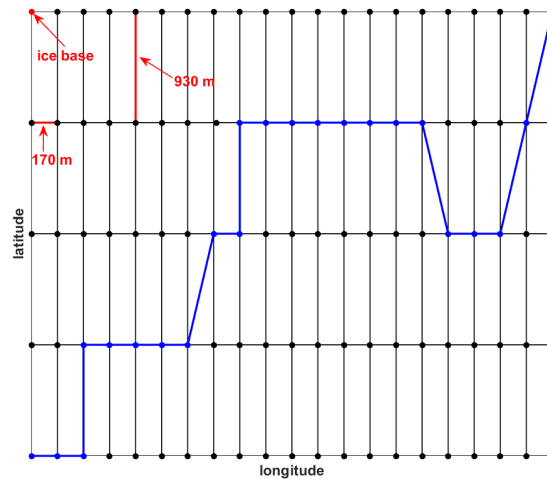
Figure 3.6: *Schematic representation of the RTopo2 grid resolution. Horizontal distances result as described in the text. The cyan line indicates a flow line along the 79NG ice tongue, e.g. as shown in Figure 3.5. Note that the horizontal distances are not for scale.*

3.4   Ocean Reanalysis - ECCOv4

The reanalysis product ECCOv4 (Estimating the Circulation and Climate of the Ocean version 4) consists of two portions (Forget et al., 2015): First, the initial state of the ocean which is based on hydrographic observations between 1992-2015 (Figure 3.7). Second, a non-linear inverse ocean model that simulates the initial state of the future (here until 2015). The evolution of the ocean is modeled by the primitive equations (horizontal and vertical momentum eq., continuity eq, and heat and salt conservation eq.). These hydrostatic, Boussinesq equations are solved by the MITgcm which is incorporated in ECCOv4. The equations are integrated over 24 years. The observations provide constraints for the model simulations. The dynamics can be revised in Forget et al. (2015).

Monthly mean 3D fields of potential temperature and salinity are extracted. ECCOv4 has a horizontal resolution of about $2\,^\circ$. CTD stations across Fram Strait are about $40\,\mathrm{km}$ apart (Figure 3.1). The vertical resolution is $10\,\mathrm{m}$ for 5 to $115\,\mathrm{m}$, and there are 50 levels in total at irregular intervals.

As ECCOv4 assimilates observations and, thus, is expected to simulate hydrography better than a "normal" model. However, data coverage is sparse, especially on the continental shelf of Northeast Greenland and that 79NG (Figure 3.7). The data constraints are Argo floats (IFREMER), CTD profiles (NODC, WOA09), and moorings. However, only CTD profiles extend below $2000\,\mathrm{m}$ (Forget et al., 2015).
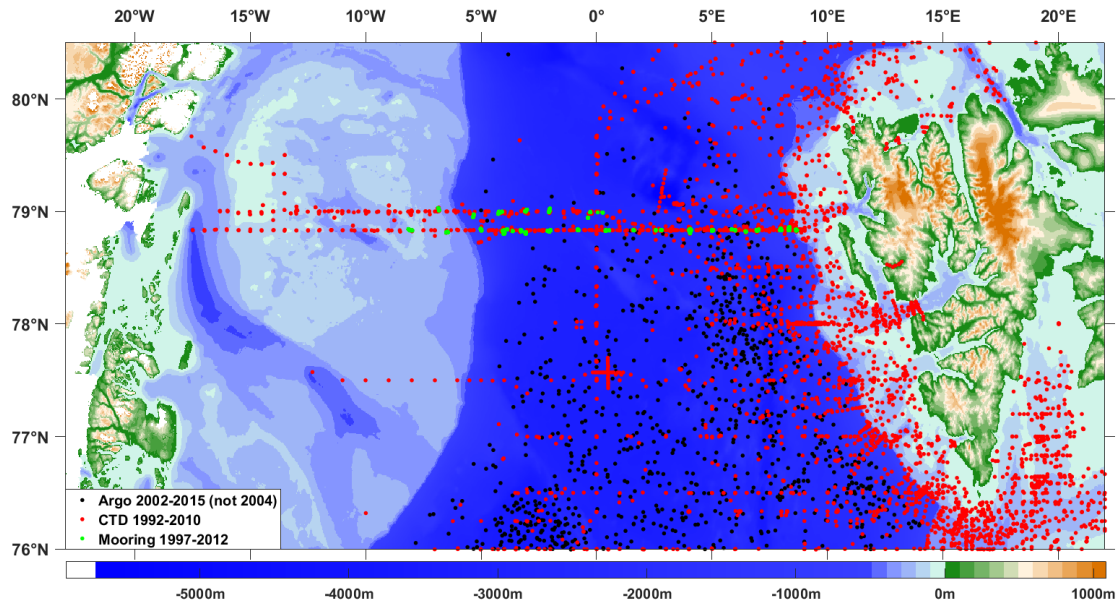
Figure 3.7: *Location of hydrographic observations which constrain ECCOv4. Argo floats are indicated in black, CTDs are indicated in red, and moorings are indicated in green. Bedrock is from RTopo2 (Schaffer et al., 2016).*

3.5   1D Ice Shelf Water plume model

A 1D Ice Shelf Water (ISW) plume model is used to simulate submarine melt rates and plume dynamics along the ice base of 79NG ice tongue. The model was developed in the MATLAB environment by Jenkins (1991). Frazil ice growth and precipitation as well as some tidal effects are included (Smedsrud and Jenkins, 2004). Extended sensitivity experiments testing modified sets of equations were performed by Jenkins (2011). The description of the model below follows Jenkins (1991) and Jenkins (2011) unless otherwise stated.

Close to the grounding line the evolution of the plume is dominated by subglacial discharge rather than by submarine melting. The model must be initialized with sufficient high subglacial discharge which is released as a point source (volume flux per unit width) at the grounding line depth. Within that region the melt rate is linear in AW temperature T_a, has a cube root dependence on the subglacial discharge $D_{X0}U_{X0}$, a complex dependence on the ice base, and varies with the stratification. However, further downstream of the ice tongue the additional freshwater supply is controlled by submarine melting which acts as a line source along the ice base.

The variables that describe the buoyant plume (Figure 3.4b) are plume thickness D, velocity U, temperature T, and salinity S. The concept of solving the problem is to introduce four ordinary differential equations (ODEs) - one for each variable - that conserve fluxes of mass (Eq. 3.5), momentum (Eq. 3.6), heat (Eq. 3.7), and salt (Eq. 3.8) at the ice-ocean boundary:

$$\frac{d}{dX}(DU) = \dot{e} + \dot{m}, \tag{3.5}$$

$$\frac{d}{dX}(DU^2) = Dg'\sin\phi - C_D U^2, \tag{3.6}$$

$$\frac{d}{dX}(DUT) = \dot{e}T_a + \dot{m}T_b - C_D^{1/2}U\Gamma_T(T - T_b), \tag{3.7}$$

$$\frac{d}{dX}(DUS) = \dot{e}S_a + \dot{m}S_b - C_D^{1/2}U\Gamma_S(S - S_b). \tag{3.8}$$

Those four equations present the core of the model. X is the distance along the ice base with its starting point at the grounding line (Figure 3.4b). The melt rate $\dot{m}$ is regulated by the entrainment $\dot{e}$ of ambient water, here AW. It has the physical unit thickness of water per unit time and is parameterized as

$$\dot{e} = E_0 U \sin\phi. \tag{3.9}$$

E_0 is the dimensionless entrainment coefficient and depends on the amount of turbulent mixing, and $\sin\phi$ is the slope of the ice base.

The terms on the right-hand side of the momentum balance (Eq. 3.6) are the buoyancy force induced by the gravity component g acting parallel to the ice base and the frictional drag

Symbol	Value	Units	Description	Symbol	Units	Description
E_0	1.8×10^{-2}	–	Entrainment coefficient	X	m	Distance along plume path
C_D	9.7×10^{-3}	–	Drag coefficient	D	m	Plume thickness
$D_{X0}U_{X0}$	1.0×10^{-3}	$m^2\,s^{-1}$	Subglacial discharge	U	$m\,s^{-1}$	Plume velocity
$C_D^{1/2}\Gamma_{T,S}$	5.9×10^{-4}	–	Stanton number	T	°C	Plume temperature
$C_D^{1/2}\Gamma_T$	1.1×10^{-3}	–	Thermal Stanton number	S	psu	Plume salinity
$C_D^{1/2}\Gamma_S$	3.1×10^{-5}	–	Haline Stanton number	T_a	°C	AW temperature
λ_1	-5.73×10^{-2}	$°C\,psu^{-1}$	Seawater freezing point slope	S_a	psu	AW salinity
λ_2	8.32×10^{-2}	°C	Seawater freezing point offset	T_b	°C	Temperature at ice-ocean boundary
λ_3	7.61×10^{-4}	$°C\,m^{-1}$	Depth dependence of freezing point	S_b	psu	Salinity at ice-ocean boundary
L	3.35×10^5	$J\,kg^{-1}$	Latent heat of fusion	T_f	°C	In-situ freezing point of plume
c_i	2.009×10^3	$J\,kg^{-1}\,K^{-1}$	Specific heat capacity for ice	$\frac{\rho_a - \rho}{\rho_0}$	–	Density contrast between plume and AW
c	3.974×10^3	$J\,kg^{-1}\,K^{-1}$	Specific heat capacity for seawater	$\dot{m}$	$m\,yr^{-1}$	Melt rate
α	3.87×10^{-5}	K^{-1}	Thermal expansion coefficient	$\dot{e}$	$m\,s^{-1}$	Entrainment rate
β	7.86×10^{-4}	–	Haline contraction coefficient	γ_T	$m\,s^{-1}$	Heat transfer coefficient
g	9.81	$m\,s^{-2}$	Acceleration due to gravity	γ_S	$m\,s^{-1}$	Salt transfer coefficient
ρ_i	917	$kg\,m^{-3}$	Average density of ice	D_e	m	Depth of ice base
ρ_w	1024	$kg\,m^{-3}$	Average density of water	$\sin\phi$	–	Slope of ice base
Pr	13.8		Prandtl number			
Sc	2432		Schmidt number			
ν	1.95×10^{-6}	$m^2\,s^{-1}$	Kinematic viscosity of sea water			

Table 3.3: (left) Physical constants and (right) output variables of the 1D ISW plume model.

parameterized by a dimensionless drag coefficient C_D. g' is the reduced gravity depending on the stratification. It is defined as

$$g' = g\left(\frac{\rho_p - \rho_a}{\rho_0}\right),$$
(3.10)

with ρ_p being the plume density, ρ_a the density of AW, and ρ_0 a reference density. $\left(\frac{\rho_a - \rho}{\rho_0}\right)$ is then the density contrast between the plume and AW. The density of the plume ρ is described by a linear equation of state:

$$\rho = \rho_0\left[1 + \beta(S - S_0) - \alpha(T - T_0)\right].$$
(3.11)

Values for the thermal expansion α and haline contraction coefficient β are given in Table 3.3. T_0 and S_0 are the initial temperature and salinity of the plume. These must lie between the AW properties and the freezing point. T_0 is set to the freezing point.

The initial plume velocity U_{X0} and plume thickness D_{X0} are calculated by assuming a balance between buoyancy and friction:

$$U_{X0} = \left(\frac{(\rho_a - \rho)g\sin\phi D_{X0}U_{X0}}{E_0\sin\phi + C_D}\right)^{0.333}$$
(3.12)

and

$$D_{X0} = \frac{D_{X0}U_{X0}}{U_{X0}}.$$
(3.13)

The density contrast between the plume and AW is then

$$\rho_a - \rho = \beta(S_a - S_0) - \alpha(T_a - T_0).$$
(3.14)

Melt rates at 79NG are expected to be highest at the grounding line depth. This is due to the pressure and salinity dependence of the freezing point:

$$T_b = \lambda_1 S_b + \lambda_2 + \lambda_3 D_e, \tag{3.15}$$

with $\lambda_3 D_e$ giving the ice base depth dependence. The ice-ocean boundary is symbolized by the subscript b. λ_1, λ_2, and λ_3 are constants presented together with other parameters used in Table 3.3. The heat needed to warm and subsequently melt the ice is provided by the AW. The conservation of heat and salt at the ice-ocean boundary are expressed as

$$Q_a^T = Q_i^T - Q_{lat}^T, \tag{3.16}$$

and

$$Q_a^S = Q_i^S - Q_{brine}^S, \tag{3.17}$$

following Figure 3.4b. Q_a^T and Q_a^S are the heat and salt fluxes associated with the AW. Q_i^T and Q_i^S are the heat and salt fluxes conducted into the ice. Q_{lat}^T is the latent heat flux caused by melting or freezing, and Q_{brine}^S is the salt flux into the ice caused by melting.

When the AW and ice properties are known, the former from a CTD profile, Eq. 3.16 and 3.17 can be rewritten as

$$c\gamma_T(T_a - T_b) = \dot{m}c_i(T_b - T_i) + \dot{m}L, \tag{3.18}$$

$$\gamma_S(S_a - S_b) = \dot{m}(S_b - S_i), \tag{3.19}$$

where c and c_i are the specific heat capacities for seawater and ice, L the latent heat of fusion which results from the transformation of solid ice to liquid, and γ_T and γ_S are the turbulent transfer coefficients for heat and salt. $\dot{m}$ c_i (T_b - T_i) is the heat directed into the ice. The ice temperature T_i determines the amount of heat conducted and is set to -15 °C. The salinity of ice, S_i, is always zero for melting.

It is of great importance to differentiate between the turbulent boundary layer and the viscous sublayer (Figure 3.4b). In the eddy dominated turbulent layer, heat and salt are diffused at same rates. In contrast, close to the ice-ocean boundary in the viscous sublayer, eddy activity is highly suppressed, and heat and salt diffuse on a molecular scale. Thus, heat is exchanged much more rapidly than salt and $\gamma_T > \gamma_S$ (Holland and Jenkins, 1999; Straneo and Cenedese, 2015). This process is accounted for in the use of the Prandtl (Pr) and Schmidt (Sc) numbers in the denominators of Eq. 3.22 and 3.23. They describe the ratio of the kinematic viscosity of seawater ν to thermal and salinity diffusivities (Holland and Jenkins, 1999). Sc is 2 432 and Pr is 13.8 (Table 3.3). Because Sc » Pr, γ_S is smaller than γ_T by a factor 31.4 within the the viscous sublayer. Thus, melting is controlled by salt transfer (Jenkins and Bombosch, 1995). According to Straneo and Cenedese (2015), all processes are parameterized by γ_T and γ_S, and so is the shear stress

$$u_*^2 = C_D U^2, \tag{3.20}$$

A potential significant contribution to the shear stress is the tidal flow (Jenkins et al., 2010) with the right hand side being replaced by C_D ($U^2 + \langle U_T^2 \rangle$). γ_T and γ_S can then be described as

$$\gamma_{T,S} = C_D^{1/2} \Gamma_{T,S} U = u_* \Gamma_{T,S}, \tag{3.21}$$

where $C_D^{1/2} \Gamma_{T,S}$ are the thermal and haline Stanton numbers St_*. They are obtained empirically from laboratory studies of boundary layers on flat, smooth plates (Kader and Yaglom, 1972, 1977). γ_T and γ_S are velocity dependent and expressed as

$$\gamma_T = \frac{C_D^{1/2}\sqrt{U^2 + U_T^2}}{2.12\ln(C_D^{1/2}Re) + 12.5Pr^{2/3} - 9} \tag{3.22}$$

and

$$\gamma_S = \frac{C_D^{1/2}\sqrt{U^2 + U_T^2}}{2.12\ln(C_D^{1/2}Re) + 12.5Sc^{2/3} - 9} \tag{3.23}$$

adopted from Kader and Yaglom (1972, 1977). Re is the Reynolds number defined as

$$Re = \frac{DU}{\nu}. \tag{3.24}$$

The first terms in the denominators can be neglected compared to the second terms. It follows that the transfer of heat and salt does not depend on the flow which is described by the Reynolds number.

Further, from the heat and salt balance at the ice-ocean boundary (Eq. 3.16 and 3.17), one can derive the slope of the meltwater mixing line (Figure 2.11c):

$$\frac{\Delta T}{\Delta S} = -\left(\frac{T_a - T_b}{S_a - S_b}\right) = -\left(\frac{c(T_f - T_i)}{c_i S_b} + \frac{L}{c_i S_b}\right), \tag{3.25}$$

In the literature it is known as the Gade line (Gade, 1979). It is further utilized that $\frac{\gamma_S}{\gamma_T} \approx 1$ away from the viscous layer (Figure 3.4b).

The effective ice temperature is

$$T_i^* = T_f - \frac{L}{c} - \frac{c_i}{c}(T_f - T_i), \tag{3.26}$$

where T_f is the freezing temperature of seawater and T_i the ice temperature. T_f is calculated using the same salinity as water at the grounding line depth (Straneo et al., 2012).

The width of the fjord gives an indication for if rotational effects, and, hence, across-fjord variations should be considered. The first baroclinic radius of deformation is based on the stratification in the fjord:

$$R = \left(\frac{g' H_1 H_2}{H}\right)^{0.5} \cdot f^{-1}, \tag{3.27}$$

H_1, H_2, and H are the upper, lower, and total water column thickness. f is the Coriolis parameter. The stratification is assumed to be a two-layer system consisting of PW overlying AW. From the

CTD profile in the rift on the 79NG ice tongue (Figure 2.11) the following values are estimated: $H_1 \approx 90\,\text{m}$, $\rho_1 \approx 1\,026.3\,\text{kg}\,\text{m}^{-3}$, $H \approx 560\,\text{m}$, $H_2 \approx 470\,\text{m}$, and $\rho_2 \approx 1\,027.7\,\text{kg}\,\text{m}^{-3}$. Eq. 3.27 yields $R \approx 9\,\text{km}$. The fjord width of 20 - 30 km thus exceeds the first baroclinic radius of deformation. As a consequence, rotation has effects on the dynamics in the fjord. Because the ISW plume model solves the problem along a predefined flow line, across-fjord variations are visualized in the different selected flow lines (Figure 3.5).

The model is steady in time, uniform in the across-flow direction, and depth-integrated. The ODEs are solved by 4th and 5th order Runge-Kutta formulas (modified version of ODE45 by C. B. Moler, last update used September 1992). Inputs are calculations along plume gradients of the prognostic variables D, U, T, and S. The integration stops when the plume has reached its level of neutral buoyancy, thus, when the momentum flux is zero. The output data are vectors of derivatives D, U, T, and S along the ice base. Subsequently, the melt rate and associated variables are calculated according to Eq. 3.18 and 3.19. Input variables are D, U, T, S, the depth of the ice base D_e, and the tidal velocity U_T. Melting occurs when the plume temperature is above its freezing temperature with S instead of S_b in Eq. 3.15. The output variables are presented in Table 3.3 (right).

4. Results

4.1 Hydrography

The properties of the water masses found in the measurements collected across Fram Strait, on the continental shelf of Northeast Greenland, and at 79NG during FS2016 are shown in the T-S diagram in Figure 4.1.

The data document presence of very cold and dense North Atlantic Deep Water (NADW) at depths across Fram Strait. AW is overlying and found in all profiles. AW partly travels around the entire Arctic Ocean and experiences heat loss and transformation into Modified Atlantic Water (MAW). A major part of MAW leaves the Arctic Ocean via Fram Strait and propagates south along the continental shelf. MAW is found above the AW across Fram Strait, on the Continental Shelf, and in the Norske Trough. PW is present in the uppermost layers of the water column in all profiles. It is distinguished between PSW and PSWw (Rudels et al., 2000). In Dijmnphna Sund, the surface layer partly consists of PSWw.

4.1.1 Fram Strait and Continental Shelf

Regionally, AW is observed between the surface and about 960 m depth across Fram Strait (Figure 4.2). Highest temperatures of 7.5 °C are found in the surface layer offshore Spitsbergen (Figure 4.3a). The maximum salinity is 35.16 psu (Figure 4.3b). Across Fram Strait the AW cools and freshens continuously toward the Continental Shelf of Northeast Greenland. The mean core temperature and salinity across Fram Strait at roughly 250 m are about 2.5 °C and 35.02 psu. Highest core temperature is found close to Spitsbergen with about 4.4 °C. However, an eddy like feature is located offshore the Northeast Greenland continental shelf roughly between 5.5 °W and 0 ° which maintains high temperatures (1.8 °C to 4.6 °C) and salinity (34.96 psu to 35.11 psu) (Figure 4.3). It is found between about 75 m and 500 m depth, coinciding fairly well with the AW core. Further, AW is present on the Continental Shelf with a mean temperature and salinity of 0.6 °C and 34.52 psu. The maximum temperature and salinity found are 1.3 °C and 34.87 psu. Cold and fresh PSW overlies the AW on the Continental Shelf. The water mass
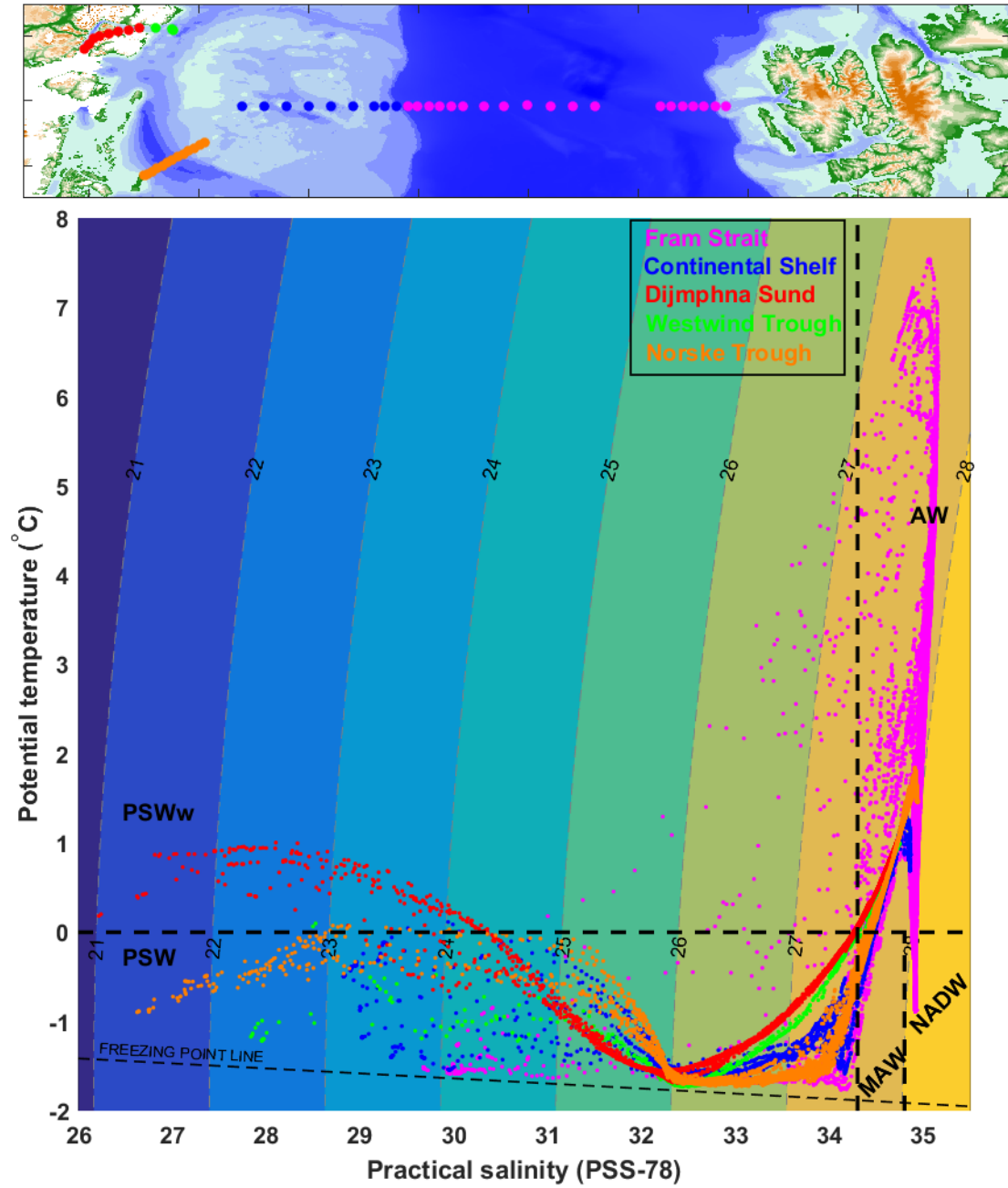
Figure 4.1: *Potential temperature versus salinity of all hydrographic data collected during FS2016. Density ($\sigma_0 = \rho_0 - 1000\,kg\,m^{-3}$) lines are drawn every $1\,kg\,m^{-3}$. The freezing point temperature referred to the surface pressure is indicated by the dashed black line. Water mass definitions are presented in Table 3.1 and Figure 3.3. CTD profiles across the Fram Strait are marked magenta, profiles from the Continental Shelf are marked blue, profiles from Dijmphna Sund are marked red, profiles from the Westwind Trough are marked green, and across Norske Trough are marked orange. The location of the profiles is shown in the small map on top and in Figure 3.1.*

intrudes offshore into the AW and clearly separates a local subsurface temperature ($7.5\,°C$) and salinity ($35.16\,psu$) maximum from the eddy (Figure 4.2 and 4.3). Between $50\,m$ to $100\,m$ depth
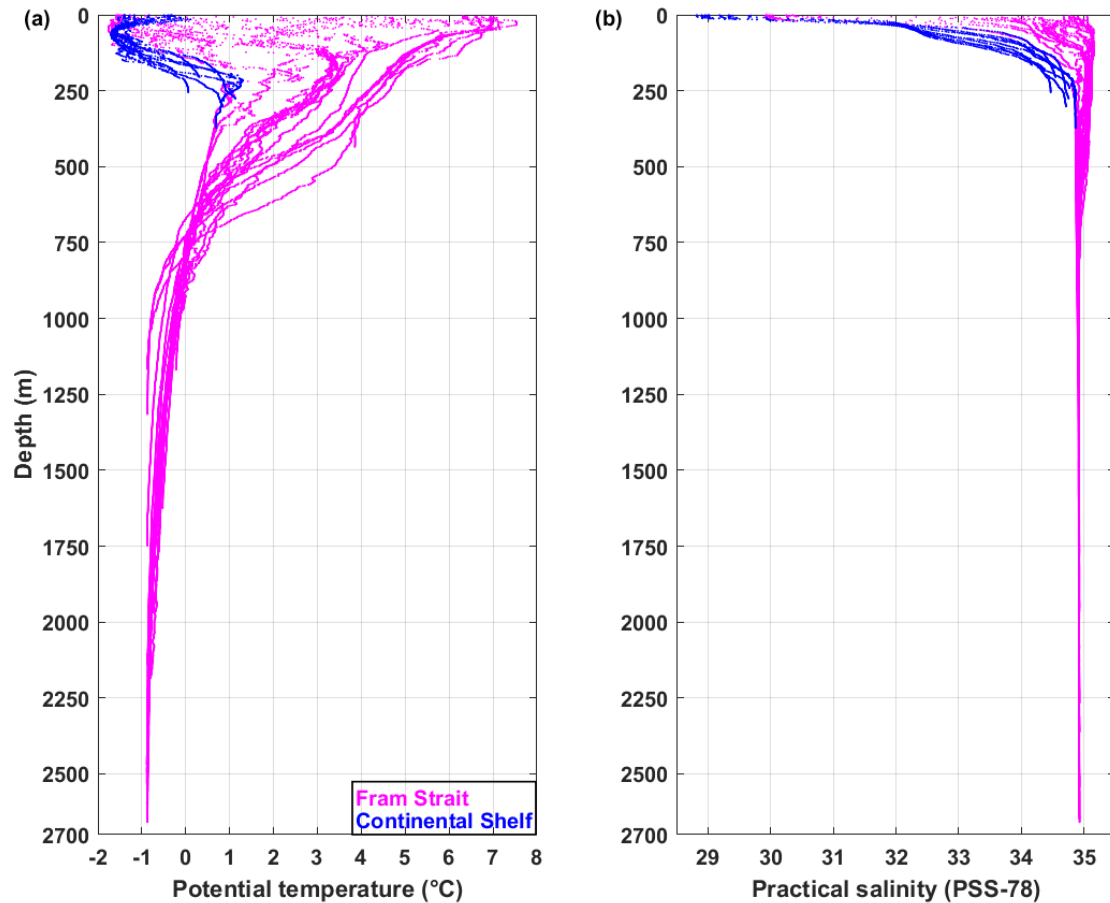
Figure 4.2: (a) Potential temperature and (b) practical salinity as a function of depth for profiles across Fram Strait (magenta) and on the Continental Shelf (blue). The locations of the CTD stations are shown in Figure 3.1.

on the Continental Shelf, a very cold and fresh mixed layer exists with temperatures locally near freezing (Figure 4.3). In contrast, the salinity increases from the surface to the AW core, with only a very small decrease below 500 m (Figure 4.2).

4.1.2   Norske Trough

Across the Norske Trough, PSW overlies a several hundred meters thick layer of AW which is present below 200 m (Figure 4.4a, b and 4.5). The deep waters in Norske Trough clearly stems from recirculating AW across Fram Strait (Figure 4.1) and are modified due to mixing and cooling. Further, AW properties on the continental shelf at about 250 m depth are identical to AW in the Norske Trough at this depth (Figure 4.2 and 4.4a, b). At the surface, temperature ranges between -0.9 °C and 0.0 °C and salinity between 26.62 psu and 30.66 psu. Below, at depths between 40 m and 100 m, a very cold and thick layer that is well mixed in temperature and close to the freezing point is present (Figure 4.4a and 4.5). In contrast, salinity increases
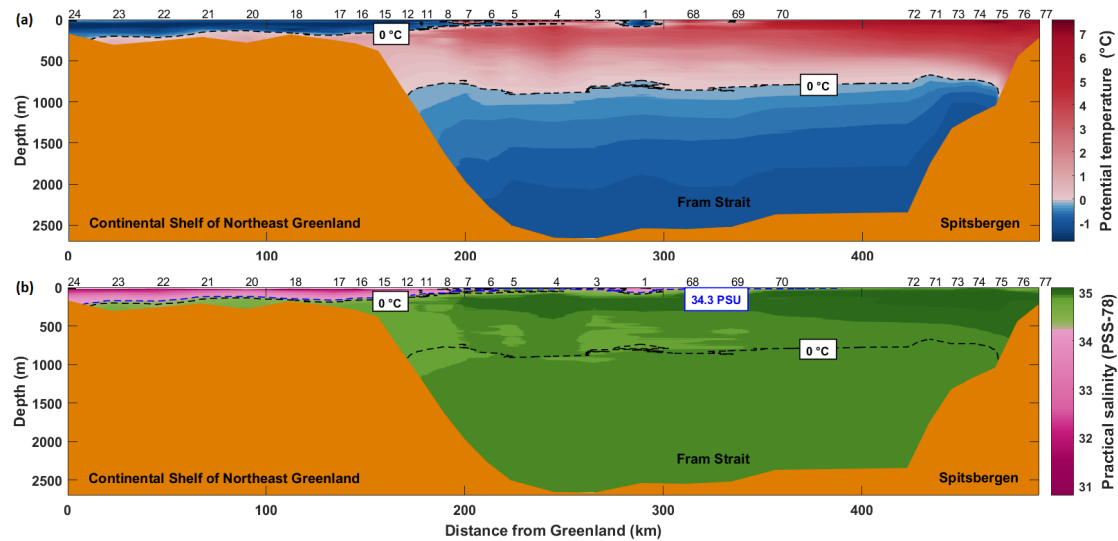
Figure 4.3: *(a) Potential temperature and (b) practical salinity across Fram Strait and on the Continental Shelf of Northeast Greenland. The locations of the CTD stations are shown in Figure 3.1. The 0 °C isotherms (black dashed) and the 34.3 psu isohaline (blue dashed) define the AW. The bathymetry is based on the depth measured during the CTD cast minus 10 m.*
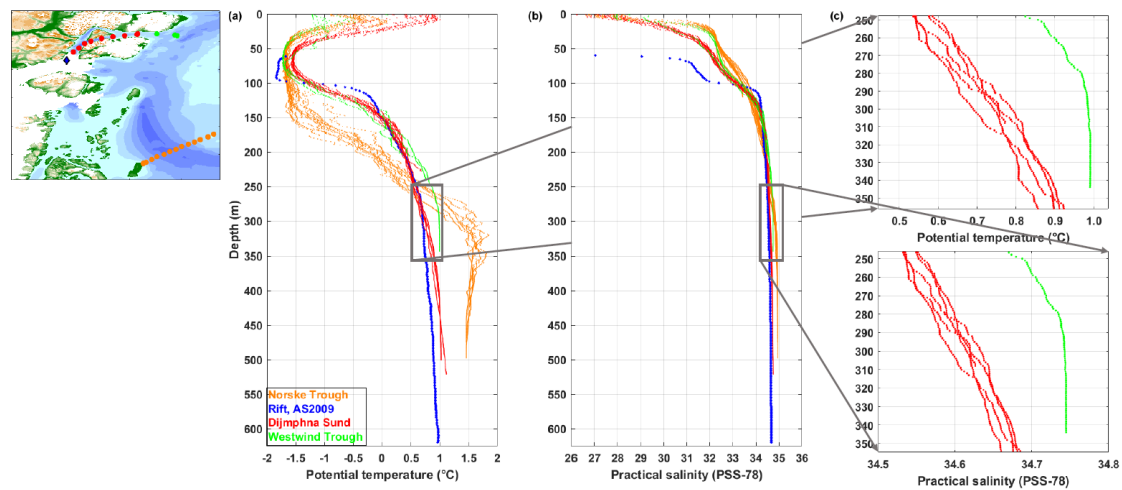
Figure 4.4: *(a) Potential temperature and (b) salinity across the Norske Trough (orange), in the Rift (blue), in Dijmphna Sund (red), and across the Westwind Trough (green). (c) Expanded view illustrating differences between profiles in Dijmphna Sund (red) and across Westwind Trough (green). The locations of the CTD stations are shown in Figure 3.1.*

gradually downwards (Figure 4.4b. This feature is a cold halocline. Temperature varies between -1.7 °C and -1.4 °C and salinity between 32.23 psu and 33.64 psu. The salinity increase drives a strong stratification which increases rapidly separating the surface and subsurface layers from the AW layer at depth.

Maximum AW temperature of about 1.8 °C is found at roughly 321 m. Subsequently, the
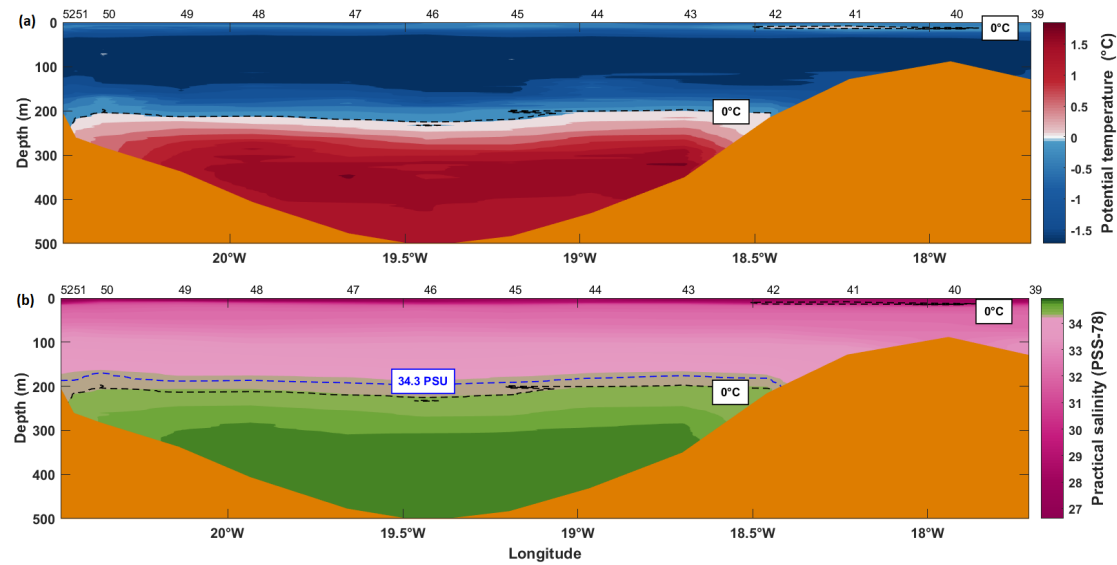
Figure 4.5: *(a) Potential temperature and (b) salinity across Norske Trough. The locations of the CTD stations are shown in Figure 3.1. The 0 °C isotherms (black dashed) and the 34.3 psu isohaline (blue dashed) define the AW. The bathymetry is based on the depth measured during the CTD cast minus 10 m.*

temperature decreases to about 1.5 °C at the bedrock (498 m). The salinity increases steadily to 34.94 psu at the bedrock. Thus, the AW is colder and fresher than the AW transported by the eddy offshore (Figure 4.3).

AW is present in the cavity below 150 m (Figure 4.4a, b, Section 2.4.1). In contrast, across Norske Trough it is found below 200 m - 230 m. Moreover, AW at depths across the Norske Trough is much warmer and saltier than in the cavity.

4.1.3   Dijmphna Sund and Westwind Trough

In the uppermost 20 - 30 m of the water column in Dijmphna Sund relatively warm and fresh PSWw is present (Figure 4.4a, b and 4.6). It overlays colder PSW. AW is found deeper in the water column. Additionally, the measurements document a 30 m thick layer which is well mixed in temperature close to freezing. In contrast, the salinity increases gradually downwards. The structure of the water column outside Dijmphna Sund in the Westwind Trough is similar. However, properties differ, especially in the upper 100 m and at depths. The surface layer is much colder and consists of PSW instead of PSWw as in Dijmphna Sund (Figure 4.6). Temperatures in the cold mixed layer are lower in the Westwind Trough. At depths, the AW is much warmer and saltier reflecting the closer distance to Fram Strait (Figure 4.6c). For instance, at 300 m depth the contrast in temperature is 0.3 °C and in salinity about 0.15 psu.

Close to the mouth of Dijmphna Sund (station 34) a sill is present as shallow as about 190 m
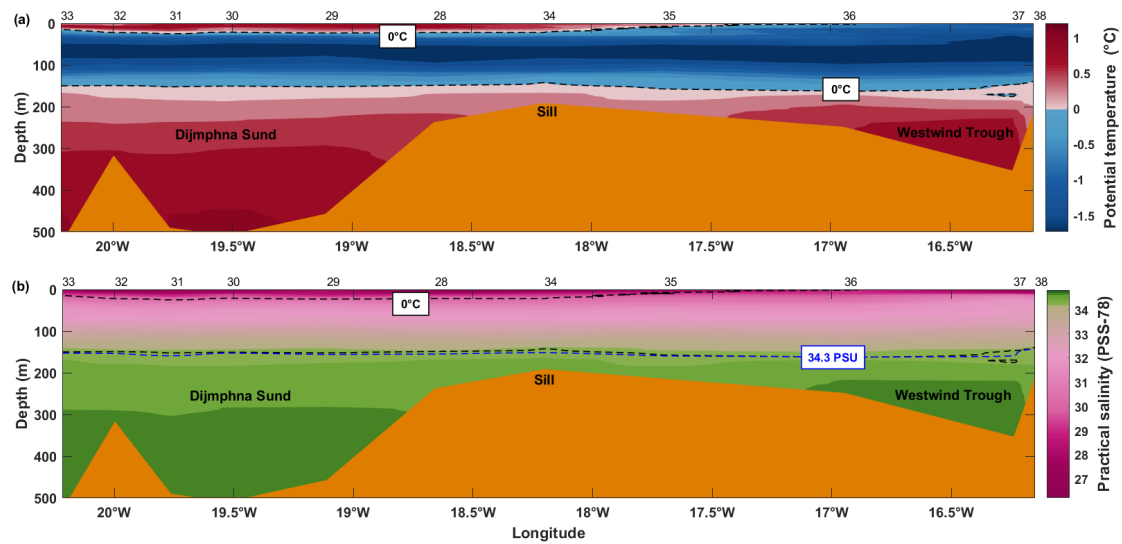
Figure 4.6: *(a) Potential temperature and (b) salinity along Dijmphna Sund and in the Westwind Trough. The locations of the CTD stations are shown in Figure 3.1. The 0 °C isotherms (black dashed) and the 34.3 psu isohaline (blue dashed) define the AW. The bathymetry is based on the depth measured during the CTD cast minus 10 m.*

(Figure 4.6). In general, Dijmphna Sund is about 150 m deeper than the part of the Westwind Trough shown here and the deepest water is warmer and saltier than in the Westwind Trough. Figure 4.1 shows the water masses in TS-space in Dijmphna Sund observed during FS2016 and AS2009 as well as in the cavity. During FS2016, the surface layer in Dijmphna Sund consists of PSWw whereas during AS2009 mainly PSW is present. Depths between 50 m and 100 m are occupied by very cold water during both surveys. Temperatures close to the ice in the rift profiles fall along the freezing point line. At depths, AW is present in all profiles.

AW most likely enters the cavity via the main front at depths below 300 m. The mixture of AW, meltwater modified water and runoff modified water leaves the cavity via Dijmphna Sund and the main front at shallower depths (Figure 2.9). The deep waters in all profiles fall along the meltwater mixing line in TS-space (Figure 4.7). TS-properties in Dijmphna Sund from FS2016 follow the line very accurately (inlet). In contrast, the profiles in Dijmphna Sund and in the cavity during AS2009 veer from the meltwater mixing line towards the runoff mixing line.

4.2 Ice-Tethered Mooring and Tidal Analysis

Current measurements obtained from the ITM5 are used to examine the mean flow in the cavity below the 79NG ice tongue. Moreover, inflow and outflow pathways of AW and ISW are investigated, and the velocity field is used to calculate the tidal flow.
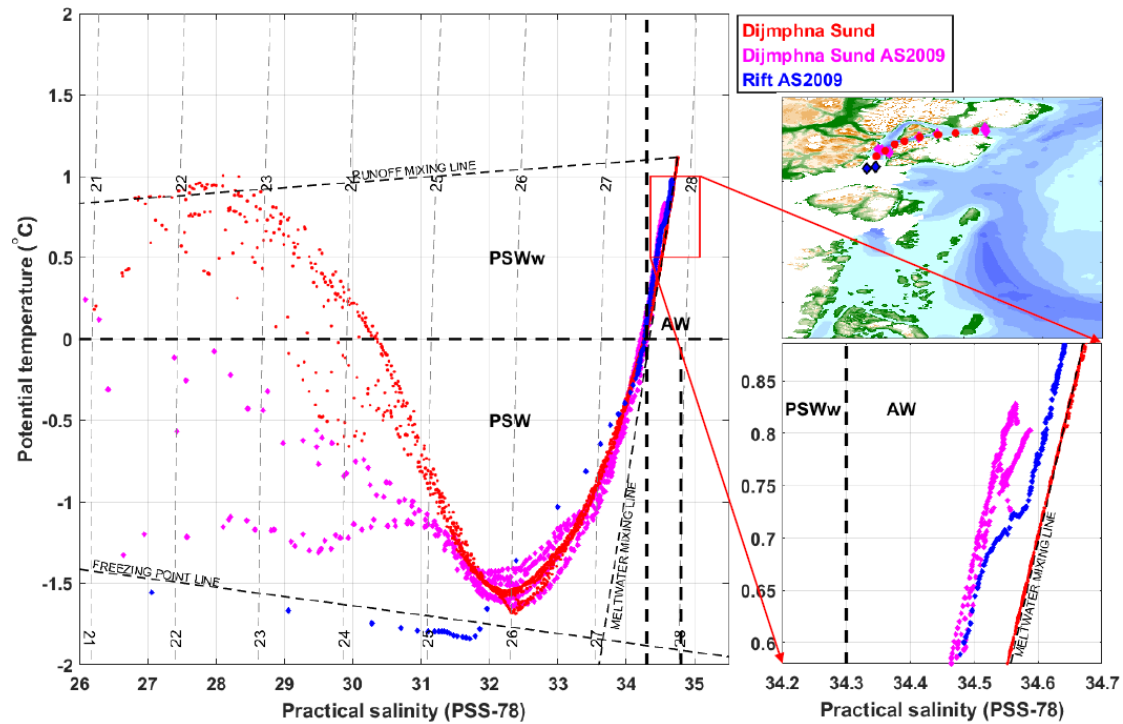
Figure 4.7: *Potential temperature versus salinity of hydrographic data collected in Dijmphna Sund and in the cavity*
below the 79NG ice tongue. Density ($\sigma_0 = \rho_0 - 1000\,kg\,m^{-3}$) lines are drawn every $1\,kg\,m^{-3}$. The freezing point
temperature referred to the surface pressure is indicated by the dashed black line. Water mass definitions are presented
in Table 3.1 and Figure 3.3. CTD profiles from Dijmphna Sund obtained during FS2016 are marked red, obtained
during AS2009 are marked magenta, and profiles from the cavity obtained during AS2009 are marked blue. The
meltwater mixing line connects the densest and warmest AW found in Dijmphna Sund during FS2016 (T = 1.1 °C,
S = 34.75 psu) and the effective ice properties ($T_i^* = -92.8\,°C$, $S_i = 0\,psu$, Eq. 3.26). The mixture of AW water and
glacial runoff fall along the runoff mixing line with the runoff temperature and salinity being T = 0 °C and S = 0 psu
(Straneo et al., 2012). The right inlet shows an expanded view presenting the deepest water masses. The location of
the profiles is shown in the small map at the right and in Figure 3.1.

4.2.1   Mean Flow

Figure 4.8 shows the time series of the mean flow (green) decomposed into (a) the east/west
and (b) the north/south components for the four aquadopps deployed at (top to bottom) 165 m,
250 m, 370 m, and 500 m depth in the water column. The mean flow is not significantly different
from the detided flow (blue) which is more visible in the graph. Velocities are on the order of 5
to $10\,cm\,s^{-1}$. Currents in the east/west direction are generally stronger than in the north/south
direction.

 Figure 4.9 shows the progressive vector displacements (PVD) of a water parcel based on the
current measurements at fixed locations (Skogseth et al., 2013). Displacements are on the order
of 50 km to 90 km maximum.
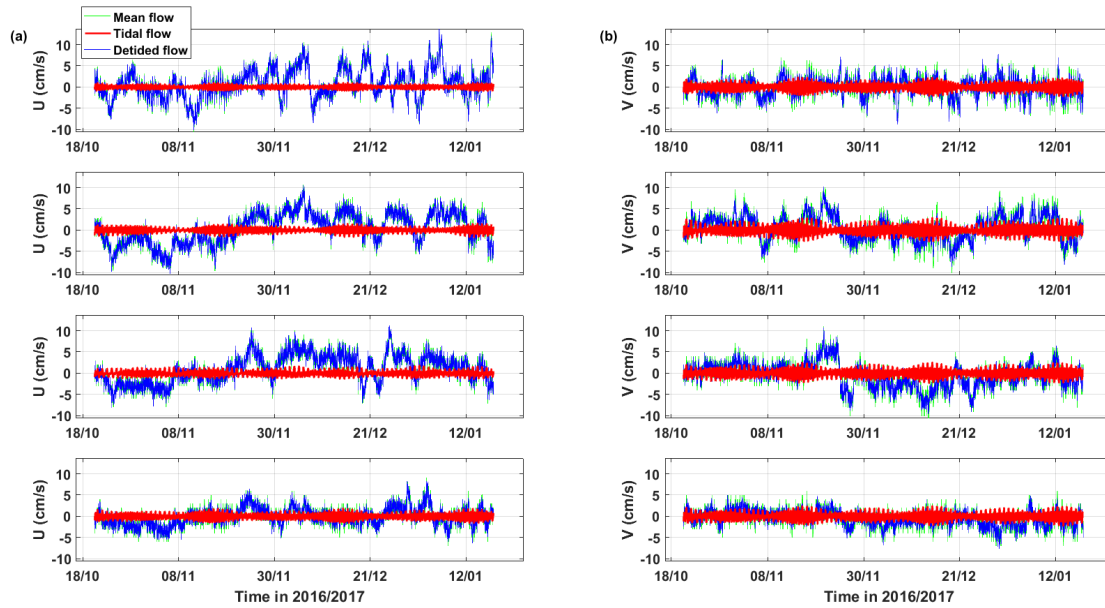
Figure 4.8: *ITM measurements in the cavity below the 79NG ice tongue. The ITM was deployed in a rift close to the northern terminus (Figure 3.5a, blue pentagram). (a) East/west and (b) north/south velocity components for (from top to bottom) 165 m, 250 m, 370 m, and 500 m depth. Measurements are shown for the period 21 October 2016 to 18 January 2017. The mean flow is marked green, the calculated tidal flow red, and the detided flow blue.*

During the first third of the sampling period (about 30 days), the data document a mean flow westward at all depths (Figure 4.8a and 4.9). This pattern is less pronounced closest to the ice at 165 m. At this depths, periodical events exist where the flow is directed eastward on the order of $5 \, \text{cm s}^{-1}$ (Figure 4.8a, top panel). A water parcel would reach the grounding line within about 20 days at 250 m (Figure 4.9, orange). For the subsequent 60 days, the favored direction is east, toward the main front. At 500 m, the currents are weaker. At 250 m, 370 m, and 500 m, currents are directed northward for the first 30 days (Figure 4.8b and 4.9). The mean flow at 165 m is very weak and rather directed south. For the remaining 60 days water at 370 m and 500 m flows southward (Figure 4.8b lower two panels, and 4.9). At 250 m, the currents are dominated by an alternating north-south-north flow with a periodicity of about 30 days. Currents at 165 m do not reveal a favored northern or southern flow direction (Figure 4.8b top panel). Similarities exist in the current structure at 165 m, 250 m, and 500 m depth. The currents at 165 m do not reveal a meridional mean flow. Waters at 250 m flow northward and waters at 370 m southward.

4.2.2 Tidal Flow

The tidal flow (red) is overlaid on the velocity field in Figure 4.8. It is quite small and ranges between $0.93 \, \text{cm s}^{-1}$ and $1.18 \, \text{cm s}^{-1}$ (Table 4.1). Both the east and north component clearly reveal variations in time. The tidal flow and the contribution to the variation in the mean flow
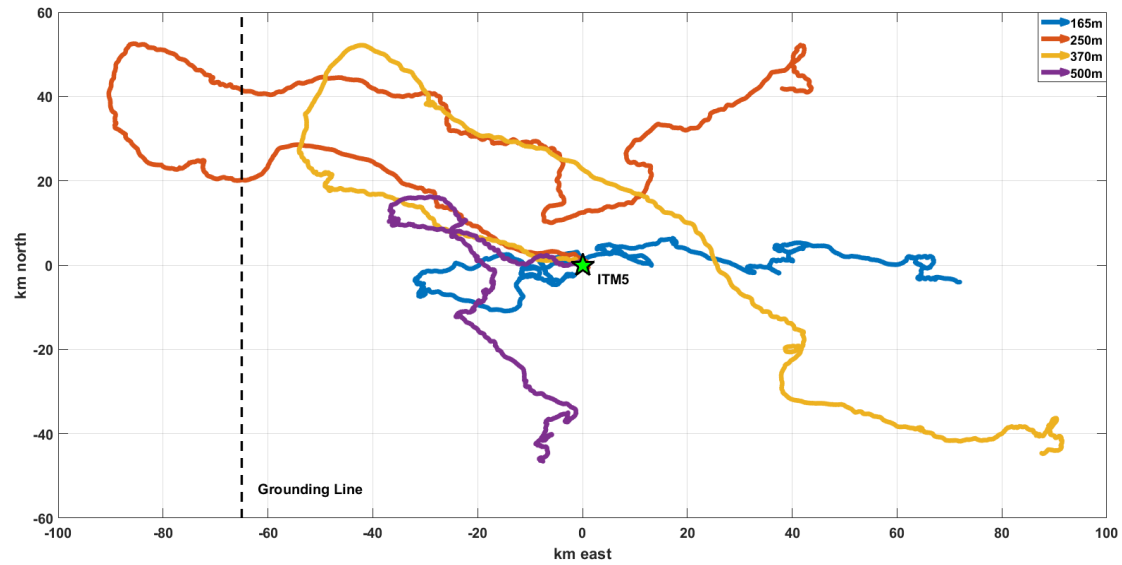
Figure 4.9: *Progressive vector displacement (PVD) of currents at 165 m (blue), 250 m (red), 370 m (yellow), and 500 m (purple) depth relative to the starting point 21 October 2016. The location of the ITM is about 15 km upglacier from the northern front and indicated by the blue pentagram (Figure 3.5a).*

Aquadopp	Tidal velocity $\sqrt{\langle U_T^2 \rangle}$ (cm s^{-1})	Total explained variance (%)	Variance in u_T (%)	Variance in v_T (%)
165 m	0.93	6.8	1.8	18.2
250 m	1.18	8.2	3.3	15.4
370 m	1.08	7.8	4.3	11.9
500 m	1.08	18.6	12.4	26.1

Table 4.1: *Tidal contribution to the variability in the velocity field at the four different depth levels 165 m, 250 m, 370 m, and 500 m. The contribution is stated in %. The mean tidal velocity $\sqrt{\langle U_T^2 \rangle}$ is calculated as $\sqrt{u_T^2 + v_T^2}$ (Eq. 3.4).*

are strongest in the north component at all depths (Figure 4.8 and Table 4.1). However, the tidal flow is much smaller than the mean flow at all depths (Figure 4.8). Tides can only explain about 6.8 % (165 m), 8.2 % (250 m), 7.8 % (370 m), and 18 % (500 m) of the total variance in the mean flow (Table 4.1). For instance, at 165 m tidal effects explain only 1.8 % of fluctuations in the east component, whereas tides explain 18.2 % of fluctuations in the north component.

The five most pronounced tidal constituents are O1, K1, N2, M2, and S2 of which M2 is by far the strongest. O1, M2, and S2 are fairly barotropic (Figure 4.10), whereas K1 and N2 slightly rotate with depth. However, this might not be significant.

The rotation of the M2 tidal ellipses are anticyclonic at 165 m, 370 m, and 500 m. At 240 m tides rotate cyclonically.
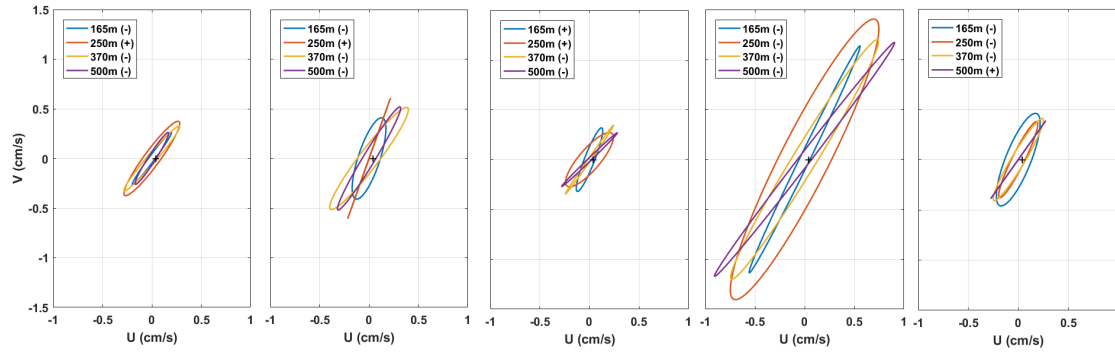
Figure 4.10: *Barotropic tidal ellipses of the five most dominating constituents in the velocity time series shown in Figure 4.8 (left to right: O1, K1, N2, M2, and S2). Numbers displayed in the legend indicate the instrument depth. (+) means cyclonic and (−) anticyclonic rotation. The harmonic analysis were performed using T_{TIDE} (Pawlowicz et al., 2002).*

4.3 Ocean Reanalysis - ECCOv4

ECCOv4 provides monthly potential temperature and practical salinity fields for the period 1992-2015. The main aims of this chapter are first, to evaluate the ECCOv4 with the observations from FS2016 and second, to investigate annual and seasonal variations in AW temperature, salinity, and layer thickness. The AW properties play a key role in submarine melting of the 79NG ice tongue. Therefore, a time series of a profile in the Norske Trough is examined. The location is chosen because the data collected during FS2016 reveal the presence of AW in this trough (Section 5.3.2). Further, AW found in the Norske Trough flows toward the main front of 79NG and into the cavity below its ice tongue where it drives melting (Schaffer et al., 2017; Wilson and Straneo, 2015). Hence, it is of great importance to find a range in AW properties in order to realistically quantify submarine melt rates.

4.3.1 Fram Strait and Continental Shelf

The AW is in the mean present below 1 000-1 200 m across Fram Strait in August and September (Figure 4.11). Mean core temperature and salinity are 1.0 °C and 34.98 psu. Temperatures are highest with up to 3.1 °C close to the surface offshore Spitsbergen. Highest salinity of 35.08 psu is found subsurface. In August/September during FS2016, a mean core temperature and salinity of 2.5 °C and 35.02 psu were observed. The observed maximum temperature and salinity close to Spitsbergen are 7.5 °C and 35.16 psu (Section 4.1.1). Thus, ECCOv4 simulates significantly lower temperatures than observed. Salinity is comparable.

AW cools across Fram Strait with lowest temperatures at depths and on the Continental Shelf of Northeast Greenland (Figure 4.11). The high salinity is mostly maintained, only offshore and
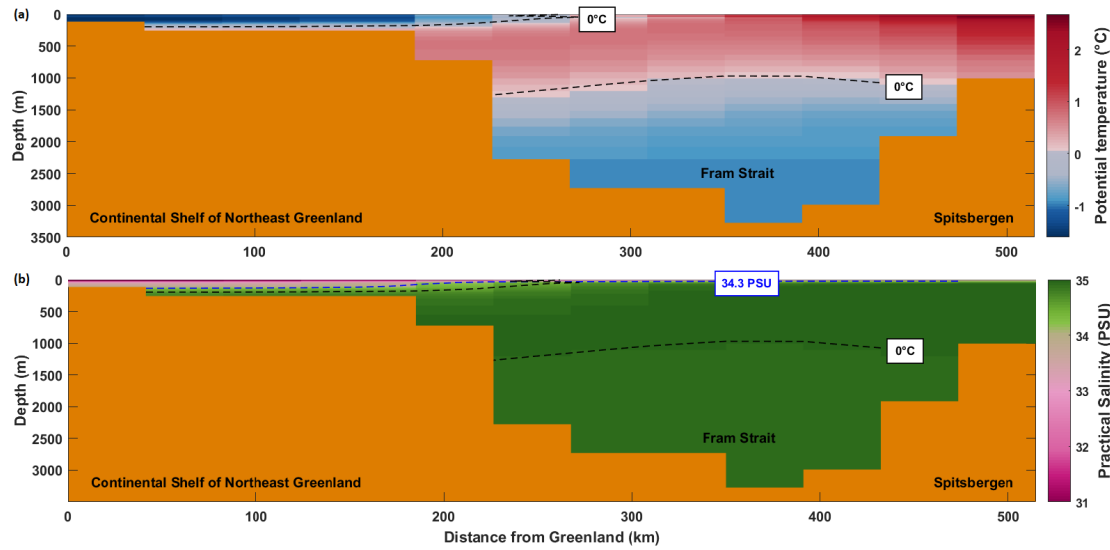
Figure 4.11: (a) Potential temperature and (b) salinity across Fram Strait and on the Continental Shelf of Northeast Greenland. The locations of the ECCOv4 stations are shown in Figure 3.1. The 0 °C isotherms (black dashed) and the 34.3 psu isohaline (blue dashed) define the AW.

onto the Continental Shelf fresher AW exists. At the bottom of the Continental Shelf the AW layer is very shallow and is detached from the surface by cold and fresh PSW. The EGC further intrudes into the AW offshore. The mean AW temperature and salinity on the Continental Shelf are 0.4 °C and 34.83 psu. Maximum temperature and salinity are 0.7 °C and 34.98 psu. AW present during FS2016 is warmer and much fresher (Section 4.1.1).

4.3.2   Norske Trough

Water properties in the Norske Trough for the period 1992-2015 are extracted from ECCOv4. The location of the chosen profile is displayed in Figure 3.1. The results are implemented in the 1D ISW plume model (Section 4.4.3) in order to simulate annual variability in submarine melt rates and plume dynamics depending on AW temperature, salinity, and depth (Section 5.4.3). Figure 4.12 shows monthly mean temperature and salinity profiles in (a) August and (b) September for each year between 1992 and 2015 (gray crosses). The black triangles indicate the mean. Water properties change only slightly from August to September. However, variations on annual timescales clearly exist

Cold and fresh PSW occupy the uppermost 50 m. Between 50 m and 100 m the water column is very cold and well mixed in temperature. In contrast, the salinity increases steadily with depth from its subsurface values. Temperature and salinity increase gradually from 100 m to their maximum values at 300 m depth. Variations in temperature between 1992 and 2015 are most pronounced in the upper 35 m and at depths. Subsurface, this is due to an exceptionally warm
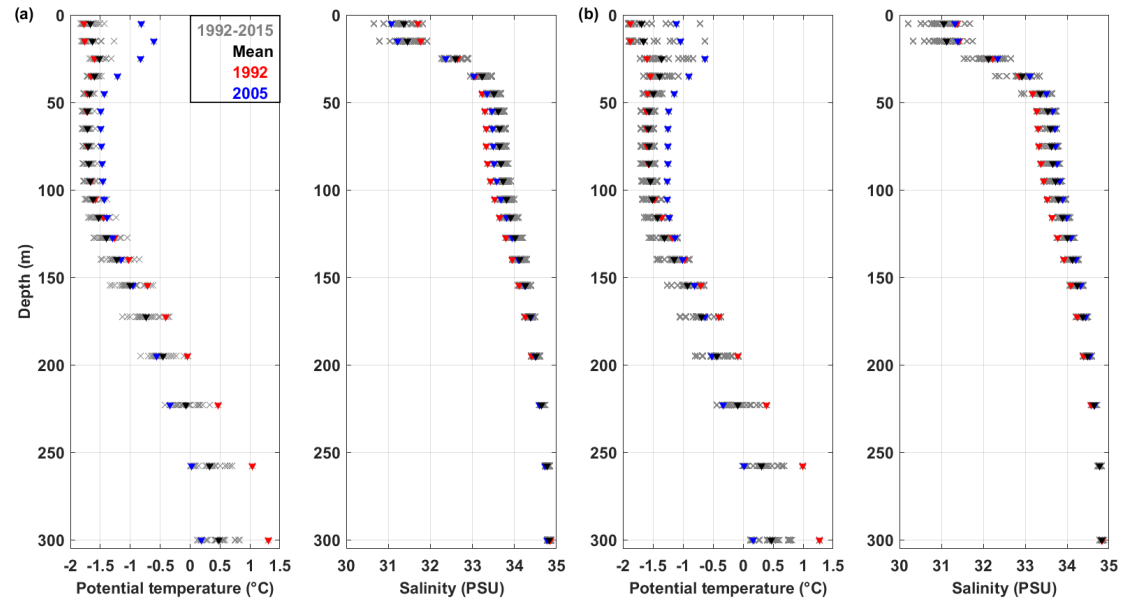
Figure 4.12: *Temperature and salinity profiles with respect to depth for (a) August and (b) September between 1992 and 2015 from ECCOv4.*

layer during 2005 (blue) in August and during 2001 and 2005 (blue) in September.

Simulated AW is in the mean present below 225 m (Figure 4.12). In 1992 (red), AW is shallower and present at and below 200 m. In contrast, in 2005 (blue) AW is deeper and not found before 255 m. As a result, the depth where AW is present varies on the order of 55 m. AW temperature and salinity clearly varies. Highest AW temperatures with 1.3 °C are found in 1992 (red) at 300 m depth. Very cold AW with 0.1 °C is present in 2005 (blue) at the same depth. Thus, AW temperatures vary on the order of 1.2 °C. The salinity varies between 34.78 psu and 34.87 psu. Variations are on the same order at shallower depths. The mean AW temperature and salinity are about 0.5 °C and 34.82 psu. The results are recapped in Table 4.2. Properties of AW from a profile in the middle of the Norske Trough obtained during FS2016 (Figure 4.4a, b) are also listed for comparison. The comparison shows that ECCOv4 appears to be able to capture the observations in the Norske Trough in a good way.

	AW presence	Temperature at 300 m	Salinity at 300 m
	(m)	(°C)	(psu)
ECCOv4	200 - 255	0.1 - 1.3	34.78 - 34.87
FS2016	220	1.2	34.79

Table 4.2: *AW properties in the Norske Trough simulated by ECCOv4 and observed during FS2016.*

4.4   1D ISW plume model

The 1D numerical ISW plume model has been applied to three flow lines along the ice base of the 79NG ice tongue (Figure 3.5b). The focus lies on the evolution of submarine melt rates and the plume dynamics with respect to the distance from the grounding line. The parameters that control the melting process and the plume dynamics are tuned. First, the model results obtained using parameters that are believed to be the best choice for the 79NG ice tongue are described. These simulations are referred to as the STANDARD case (Section 4.4.1). In the following, sensitivity experiments of the submarine melt rate and on the plume dynamics to values of the most important parameters are presented (Section 4.4.2). Thereafter, the variability of AW temperature and its presence in the water column and its control on the melt rate and plume dynamics is discussed (Section 4.4.3). Lastly, a simplified method is used to yield estimates of the stability of the ice tongue and the fresh water export associated with melting (Section 5.4.4). Values for the time scales on the disappearance of the 79NG ice tongue based on the melt rates obtained during the previous model simulations are provided.

4.4.1   The Centreline of the 79NG Ice Tongue - The STANDARD case

In the STANDARD case the model was applied to the centreline of the 79NG ice tongue (Figure 3.4a, 3.5, and 4.14a). Further, the choices for the model parameters used are presented as well as a short review of their influences on the submarine melt rates and the plume dynamics.

The entrainment coefficient E_0 plays a key role in the parameterization of the entrainment rate $\dot{e}$ (Eq. 3.9). In turn, $\dot{e}$ dictates the amount of AW that is transferred into the plume and toward the ice-ocean boundary. The value for E_0 applied in the performed survey is 1.8×10^{-2}. Furthermore, the slope of the ice base $\sin \phi$ is also proportional to the entrainment rate and very likely has significant effects on the processes. The slope along the centreline is marked black in Figure 4.13. The drag coefficient C_D is suggested to be very important for the flow along the ice base, especially for the plume velocity. The value 9.7×10^{-3} is adopted from Jenkins et al. (2010). The subglacial discharge $D_{X0}U_{X0}$ is the source for the plume and makes it rise initially. Moreover, it is the most unknown parameter. The model results are expected to be highly sensitive to this quantity. The value applied is $1 \times 10^{-3}\,\mathrm{m^2\,s^{-1}}$. Tides are expected to increase the energy available for mixing, the rate of which heat and salt are transferred toward the ice-ocean boundary (Eq. 3.22 and 3.23), and the shear between the plume and the ice-ocean boundary (Eq. 3.20). The value $1.18\,\mathrm{cm\,s^{-1}}$ for the tidal flow used is the root mean square, $\sqrt{\langle U_T^2 \rangle}$, at approximately 250 m depth calculated from the ITM5 measurements in the rift of the ice tongue. The turbulent transfer coefficients for heat and salt, $\gamma_{T,S}$, determine how fast heat and salt is transported and exchanged at the ice-ocean boundary. Hence, they play a major
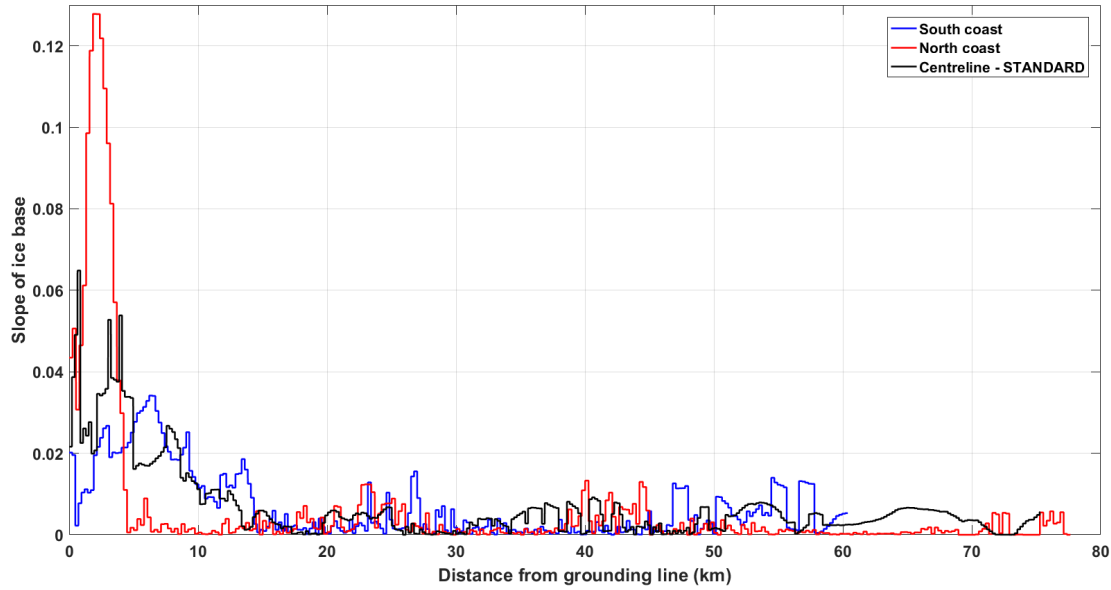
Figure 4.13: *The slope of the ice base* sin φ *with respect to the distance from the grounding line in km along three flow lines. Centreline (black), South Coast (blue), and North Coast (red). The flow lines are marked cyan in Figure 3.5. The ice base along the flow line was smoothed using a moving average fit with a horizontal footprint of about 1.1 km.*

role in the heat and salt balance. The velocity dependent formulation from Jenkins (1991) is devoted (Eq. 3.22 and 3.23). The ice base changes laterally and therefore determines a spatially varying distribution of the melt rate and plume dynamics. The ice bases are smoothed using a moving average fit with a horizontal footprint of about 1.1 km (Section 3.3). The hydrographic properties of the water column in the cavity below the ice tongue are provided by the CTD profile taken in the rift close to the northern front (Figure 4.4a, b). AW is present below 150 m. As most of the ice tongue is below 150 m depth (Figure 4.14a)), the ice is in direct contact with AW. The chosen set of parameters used for the STANDARD case are summarized in Table 4.3.

Figure 4.15 shows (a) the melt rates in $m\,yr^{-1}$, (b) the density contrast between the plume and AW in $kg\,m^{-3}$, (c) the thermal driving in °C, (d) the plume temperature in °C, (e) the plume salinity in psu, (f) the plume velocity in $cm\,s^{-1}$, and (g) the plume thickness in m. The profiles are plotted as a function of the distance X in km referenced to the grounding line (GL). The GL is located at X = 0 km and the zone between X = 0 km and X = 10 km is termed the grounding line zone (GLZ). Further, the transition zone (TS) between 10 km and 20 km downstream from the GLZ and the downstream zone (DSZ) are defined. The latter is the part of the ice tongue downstream from 20 km until the main front. These segments were chosen corresponding to distinct pattern in the melting. The plume is initiated at the GL and evolves along the ice base. It reaches its level of neutral buoyancy and detaches at about 75 km (Figure 4.15 and Table 4.4). Neutral buoyancy is reached when the density contrast between the plume and the AW is zero.
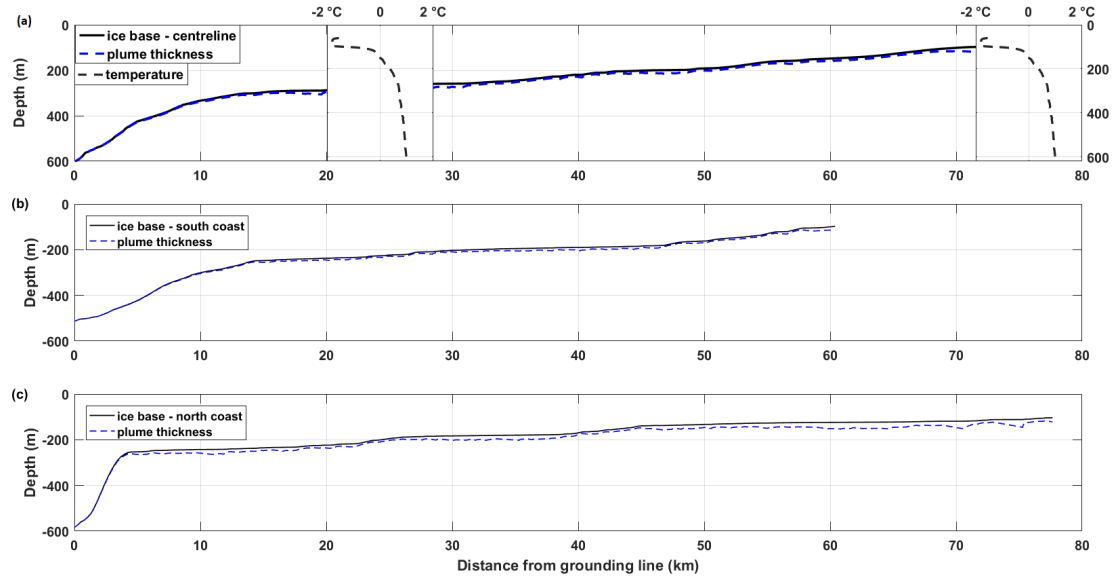
Figure 4.14: Ice base (solid) and plume thickness (dashed) in m with respect to the distance from the grounding line in km along three flow lines. (a) Centreline with the temperature profile from the rift obtained during AS2009 overlaid, (b) South Coast, and (c) North Coast. The flow lines are marked cyan in Figure 3.5b. The ice base was smoothed using a moving average fit with a horizontal footprint of about 1.1 km.

The largest melt rates of about 50 - 75 m yr^{-1} are simulated within the GLZ (Figure 4.15a and Table 4.4). They decay rapidly down-glacier from the GLZ. The maximum melt rates drop to about 6 m yr^{-1} within the TZ. Further downstream, the melt rates increase again for about 5 km to approximately 15 m yr^{-1} before a relatively steady mean melting of approximately 6 m yr^{-1} is reached. In general, the melt rates increase rapidly from 0 m yr^{-1} at the GL and follow more or less a linear relationship for 1 km.

The plume is driven by the density contrast ρ_a - ρ between AW and the plume itself. The density contrast is strongest close to the GL (Figure 4.15b). This is because of the subglacial

Parameter	Symbol	Value	Unit	Equation / Figure	Reference
Length	L	80	km	−	Schaffer et al. (2017)
Ice base	−	−	m	Figure 3.4	Schaffer et al. (2016)
Ice base slope	$\sin \phi$	−	−	Figure 4.13	Schaffer et al. (2016)
CTD profile	−	−	−	Figure 4.4a, b	Wilson and Straneo (2015)
Entrainment coefficient	E_0	1.8×10^{-2}	−	Eq. 3.9	Jenkins (1991)
Drag coefficient	C_D	9.7×10^{-3}	−	−	Jenkins et al. (2010)
Subglacial discharge	$D_{X0}U_{X0}$	1×10^{-3}	$m^2 s^{-1}$	−	Jenkins (1991)
Tidal flow	$\sqrt{\langle U_T^2 \rangle}$	1.18	$cm s^{-1}$	Eq. 3.4	Section 4.2.2
Transfer coefficients	$\gamma_{T,S}$	−	$m s^{-1}$	Eq. 3.22 and 3.23	Jenkins (1991)

Table 4.3: Model parameters used in the STANDARD case.
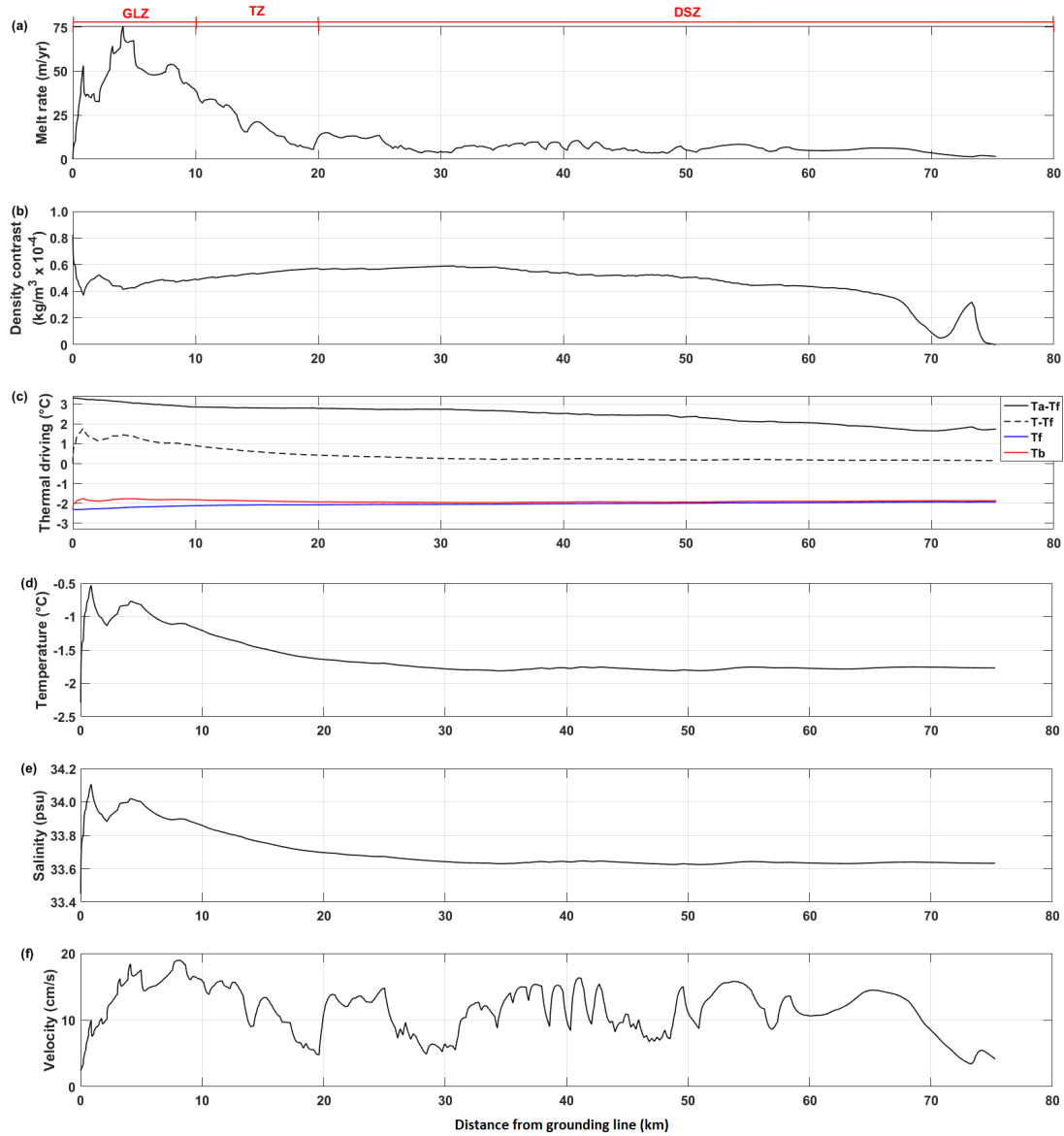
Figure 4.15: *Model results along the the centreline of 79NG ice tongue to parameters referred to as the STANDARD case. The parameters used are presented in Table 4.3. (a) Submarine melt rate, (b) density contrast between the plume and the AW, (c) thermal drivings, (d) plume temperature. (e) plume salinity, (f) plume velocity, and (g) plume thickness. GLZ means grounding line zone, TZ transition zone, and DSZ downstream zone.*

discharge which is released at this position and provides the initial buoyancy for the plume. The density contrast decreases rapidly because as the plume accelerates and its velocity increases (Figure 4.15f) more AW is entrained (Eq. 3.9). Moreover, the slope is steepest within the GLZ (Figure 4.13) and, thus, entrainment of AW is high. However, as freshwater is released into the plume due to melting, the density contrast increases again until about 30 km downstream. The increase in the amount of freshwater is evident in the salinity decrease along the ice base (Figure 4.15e). Down-glacier of 30 km, the density contrast continuously decreases as a result

Model run	Mean melt rate $(\mathrm{m\,yr^{-1}})$	Maximum melt rate $(\mathrm{m\,yr^{-1}})$	Point of detachment (km)	Final plume flux $(\mathrm{m^3\,s^{-1}})$	Travel time (days)
Standard	14.8	75.3	75.3	38 100	8.7
50 % ($E_0 = 0.9 \times 10^{-2}$)	6.3	41.9	75.5	15 000	12.8
200 % ($E_0 = 3.6 \times 10^{-2}$), 90 % ($C_D = 8.6 \times 10^{-3}$)	31.5	113.4	75.5	94 200	6.3
400 % ($E_0 = 7.2 \times 10^{-2}$)	55.7	144.0	76.3	199 800	5.6
25 % ($C_D = 2.5 \times 10^{-3}$)	21.6	75.1	69.7	60 000	4.2
50 % ($C_D = 4.9 \times 10^{-3}$)	17.7	77.9	74.5	48 900	6.2
90 % ($C_D = 8.6 \times 10^{-3}$)	15.5	76.1	75.1	39 900	8.1
200 % ($C_D = 1.9 \times 10^{-2}$)	11.3	68.4	78.3	29 100	13.8
$D_{X0}U_{X0} = 1.0 \times 10^{-9}\,\mathrm{m^2\,s^{-1}}$	5.6	74.5	75.3	1.25	9.0
$D_{X0}U_{X0} = 8.7 \times 10^{-2}\,\mathrm{m^2\,s^{-1}}$	17.4	86.8	75.3	48 268	7.6
$D_{X0}U_{X0} = 8.7\,\mathrm{m^2\,s^{-1}}$	24.7	65.7	78.7	389 710	3.2
0 % ($\sqrt{\langle U_T^2 \rangle}$)	14.8	75.3	75.3	38 100	8.6
1000 % ($\sqrt{\langle U_T^2 \rangle}$)	12.4	73.6	78.5	33 861	13.0
2000 % ($\sqrt{\langle U_T^2 \rangle}$)	9.3	71.3	78.3	26 243	19.5
50 % ($\gamma_{T,S}$)	11.4	43.7	75.3	33 000	9.8
200 % ($\gamma_{T,S}$)	17.4	113.4	75.3	41 700	8.1
$\gamma_{T,S} = 0.6 \times 10^{-2}$	21.3	232.2	75.3	46 500	7.5
$\gamma_T = 1.1 \times 10^{-2}, \gamma_S = 3.1 \times 10^{-4}$	21.2	234.0	75.3	46 500	7.5
South coast	11.6	50.7	60.4	27 600	7.9
North coast	18.6	143.9	77.7	11 877	10.4
+ 0.5 °C	18.9	94.5	75.3	41 100	7.8
+ 1.0 °C	23.1	115.1	75.3	45 000	7.2
+ 1.5 °C	27.9	137.2	75.3	48 000	6.7
+ 2.0 °C	32.6	160.6	75.3	51 000	6.3
+ 2.5 °C	37.4	185.2	75.3	54 000	5.9
+ 3.0 °C	43.4	211.0	75.3	56 700	5.6
warm AW	19.3	97.7	75.3	42 121	7.7
cold AW	10.2	54.5	75.3	33 474	10.2
shallow AW	15.1	75.8	80.0	41 735	8.3
deep AW	14.7	72.5	63.4	33 113	8.6

Table 4.4: *Sensitivity of the model results along the centreline of the 79NG ice tongue due to different parameters: Entrainment coefficient, drag coefficient, subglacial discharge, tidal flow, turbulent transfer coefficients for heat and salt, ice bases, AW temperature, and presence of AW in the water column.*

of less melting (Figure 4.15a) At about 75 km the plume reaches its level of neutral buoyancy meaning (Figure 4.15b and Table 4.4).

Figure 4.15c displays the evolution of the temperature difference between properties in the plume, termed thermal driving. The thermal driving between the AW temperature and the in-situ freezing point at the ice-ocean boundary, T_a-T_f (black solid), is highest at the GL with about 3.3 °C. It decreases nearly continuously along the ice base and reaches approximately 1.7 °C close to the main front. A core assumption in the model is that the ice-ocean boundary is at the in-situ freezing point (Eq. 3.15). Hence, a positive T_a-T_f means melting. Although T_a-T_f decreases, it maintains a very high positive value explaining the melting (Figure 4.15a). In contrast, the thermal driving of the plume and the in-situ freezing point, T-T_f (Figure 4.15c, black dashed), is lower. It peaks close to the GL to about 1.7 °C and falls along the ice base to

near 0°C. This is consistent with the plume temperature T adjusting toward the in-situ freezing point (Figure 4.15d). $T-T_f$ is positive for 30 km where also high melt rates are simulated. Further downstream it drops to near zero. This lead to lower melt rates (Figure 4.15a). T_f (Figure 4.15c, blue) increases steadily because the plume reaches shallower depths and freshens due to melting (Figure 4.15e). The same accounts to the ice-ocean boundary temperature T_b (Figure 4.15c, red), yet it is higher within the GLZ because S_b is used instead of the plume salinity S to calculate it. Further downstream, T_b and T_f are almost identical due to the decrease in S (Figure 4.15e).

The plume temperature T rises rapidly within a short distance from the GL to a maximum of about -0.5 °C (Figure 4.15d). Within the TZ and the DSZ it decreases continuously to approximately -1.8 °C because of the freshwater supply caused by melting.

The plume is fresh within the GLZ with a maximum salinity of 34.11 psu (Figure 4.15e). Downstream of 5 km, the plume freshens steadily along the ice base due to melting (Figure 4.15a) reaching a minimum salinity of 33.45 psu.

The plume accelerates linearly within 5 km due to the density contrast initiated by the release of subglacial discharge and then due to melting. It reaches a maximum velocity of about 19 cm s^{-1} (Figure 4.15e). Besides three local minima where the plume velocity rapidly decreases the plume maintains a fairly high mean velocity of about 10 cm s^{-1}. However, at approximately 70 km, the velocity decreases again to below 5 cm s^{-1}.

The plume thickness D increases nearly linearly from 0 m at the GL to about 17 m within 20 km (Figure 4.15f). Downstream from that location D experiences a sudden drop to 6 m - 7 m within 1 km. This pattern is observed two more times along the ice base where D rises to about 18 m and 14 m. These drops are consistent with an increase in the plume velocity (Figure Figure 4.15e). However, the mean thickness remains rather constant of about 10 m until close to 70 km. The plume increases then rapidly to nearly 40 m within 5 km before it drops by about 15 m. It then starts increasing again before the plume gets neutrally buoyant and detaches.

The final plume flux, a product of the final plume velocity and thickness and the width of the main front (30 km) along which it would be released in a 2D or 3D concept, is about 38 100 m^3 s^{-1} (Table 4.4). The plume travels from the grounding line toward the main front within 8.7 days.

4.4.2 Sensitivity Experiments

In this section, the sensitivity of model results to the most important parameters is studied. By changing the parameters, the modeled melt rates and plume dynamics can be amplified or reduced, but the basic patterns remain unaltered. The main aim is to investigate the response of the submarine melt rate along the ice base due to the tuning. In addition, the evolution

of the plume velocity and thickness is monitored. First, it is examined how the entrainment coefficient E_0 and the slope of ice base $\sin \phi$ affect the melt rates and the plume dynamics. Then, the influence of the drag coefficient C_D is explored before the role of the subglacial discharge is demonstrated. Subsequently, the effects of the tidal flow are analyzed. Thereafter, the turbulent transfer coefficients of heat and salt and the effects of modifying these are considered. Lastly, it is presented how the melt rates vary laterally, across the ice tongue. Therefore, the model is applied to three flow lines which have different ice bases.

Entrainment Coefficient

The entrainment rate $\dot{e}$ regulates the amount of AW put into the plume and, thus, the heat available for melting. The heat supplied to the ice-ocean boundary is proportional to both the AW temperature and the entrainment rate (Eq. 3.7) (Jenkins, 1991). Increasing the entrainment coefficient E_0 leads to an increase in $\dot{e}$ (Eq. 3.9) and, hence, in the heat reservoir. The entrainment coefficient was increased to 200 % ($E_0 = 3.6 \times 10^{-2}$, red) and to 400 % ($E_0 = 7.2 \times 10^{-2}$, green) the STANDARD value (100 %, $E_0 = 1.8 \times 10^{-2}$, black). This results in elevated melt rates everywhere along the ice base (Figure 4.16a). For the 200 % simulation a drag coefficient of roughly 90 % ($C_D = 8.6 \times 10^{-3}$, green) instead of 100 % ($C_D = 9.7 \times 10^{-3}$, black) as for the STANDARD case was used. This was done because for this combination a plume circulation did not evolve. However, the influence of a 90 % drag coefficient was tested and found that the melting does not significantly change compared to the STANDARD case (Figure 4.16b and Table 4.4). Decreasing the STANDARD value to 50 % (0.9×10^{-2}, blue) yields lower melt rates (Figure 4.16a). In general, the spatial distribution of melting does not change.

A 200 % entrainment coefficient causes an increase in the mean melt rates from about $15 \, \text{m} \, \text{yr}^{-1}$ for the STANDARD case to about $32 \, \text{m} \, \text{yr}^{-1}$ (Figure 4.16a, red, and Table 4.4). In particular, melt rates are elevated within the GLZ and the TZ. The maximum melt rate increases to approximately $113 \, \text{m} \, \text{yr}^{-1}$ compared to $75 \, \text{m} \, \text{yr}^{-1}$ for the STANDARD. The gradient within the TZ is steeper. Downstream melt rates are still very high ranging between $7 \, \text{m} \, \text{yr}^{-1}$ and $40 \, \text{m} \, \text{yr}^{-1}$. Using a 400 % entrainment coefficient leads to even higher melting (Figure 4.16a, green, and Table 4.4). In addition, the plume reaches its level of neutral buoyancy about $1 \, \text{km}$ further downstream compared to the STANDARD. This is due to the high amount of freshwater caused by significantly elevated melt rates.

Coupled to the additional freshwater the plume velocity increases (Figure 4.17a, red and blue). The higher buoyancy (not shown) supplied by the freshwater due to melting speeds the plume up. In turn, this leads to higher entrainment rates and, thus, higher melt rates. Associated with the speed up is a shorter travel time of about 6.3 days and 5.6 days for a 200 % and 400 % entrainment coefficient compared to the STANDARD (Table 4.4). However, close to the GL the
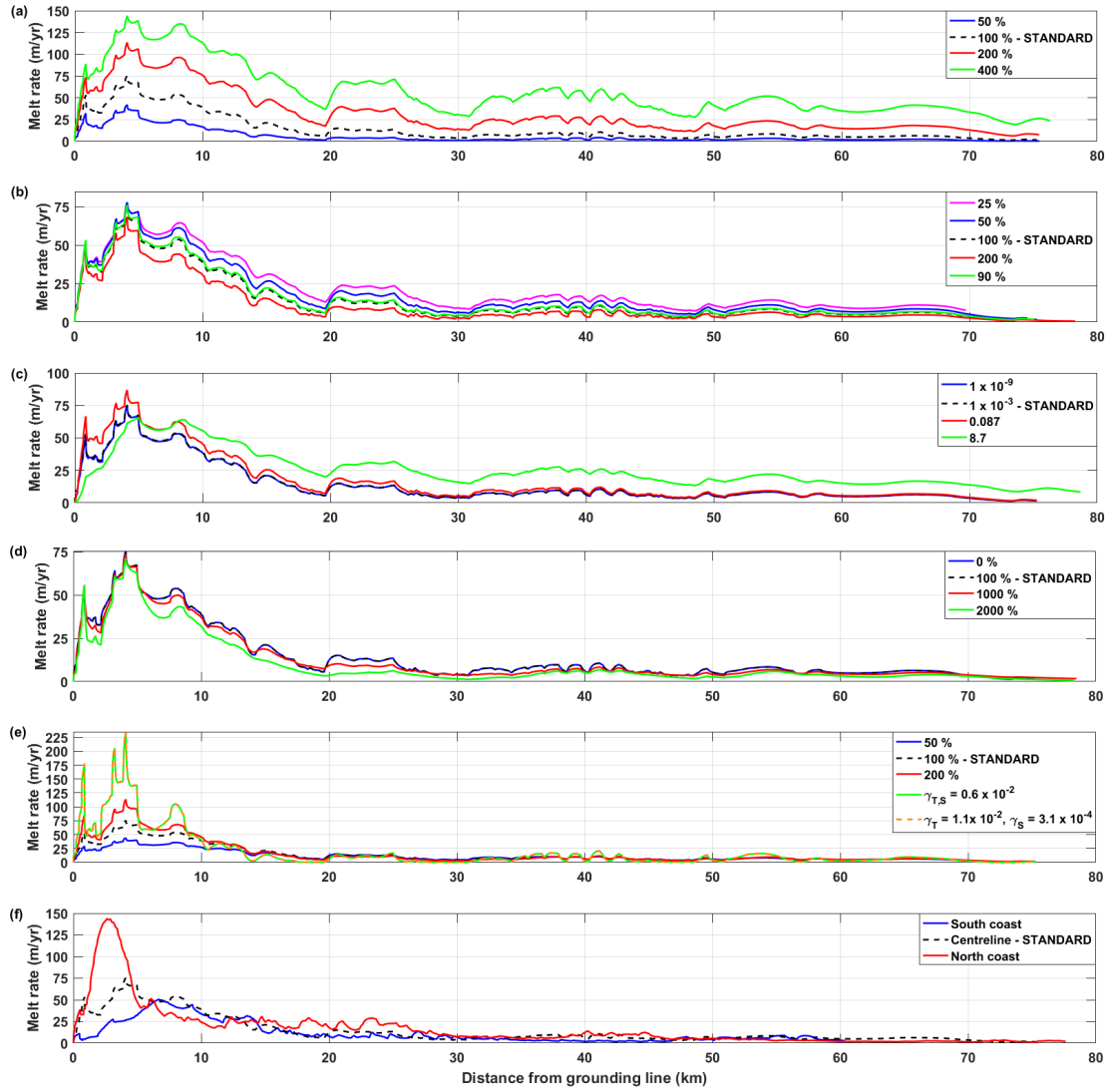
Figure 4.16: *Sensitivity of the submarine melt rate along the centreline of the 79NG ice tongue due to different parameters. (a) Entrainment coefficient, (b) drag coefficient, (c) subglacial discharge, (d) tidal flow, (e) turbulent transfer coefficients for heat and salt, and (f) ice base.*

velocity only changes slightly. In addition, the change is not very pronounced where the plume accelerates at about 20 km, 30 km, and 50 km. As significantly more freshwater is added to the plume its thickness increases (Figure 4.18a, red and green). In addition, more AW is entrained which also leads to a thicker plume. Corresponding to the increase in melting, velocity, and thickness the plume flux also increases (Table 4.4).

 Applying a lower entrainment rate, 50 %, causes a decrease in melting (Figure 4.16a, blue, and Table 4.4). Mean melt rates reduce to about 6 m yr^{-1}. The maximum malt rates within the GLZ drop to about 42 m yr^{-1}. The gradient within the TZ is less pronounced. Along the DSZ melting is near zero. Due to reduced melting less freshwater is released into the plume. As a result,
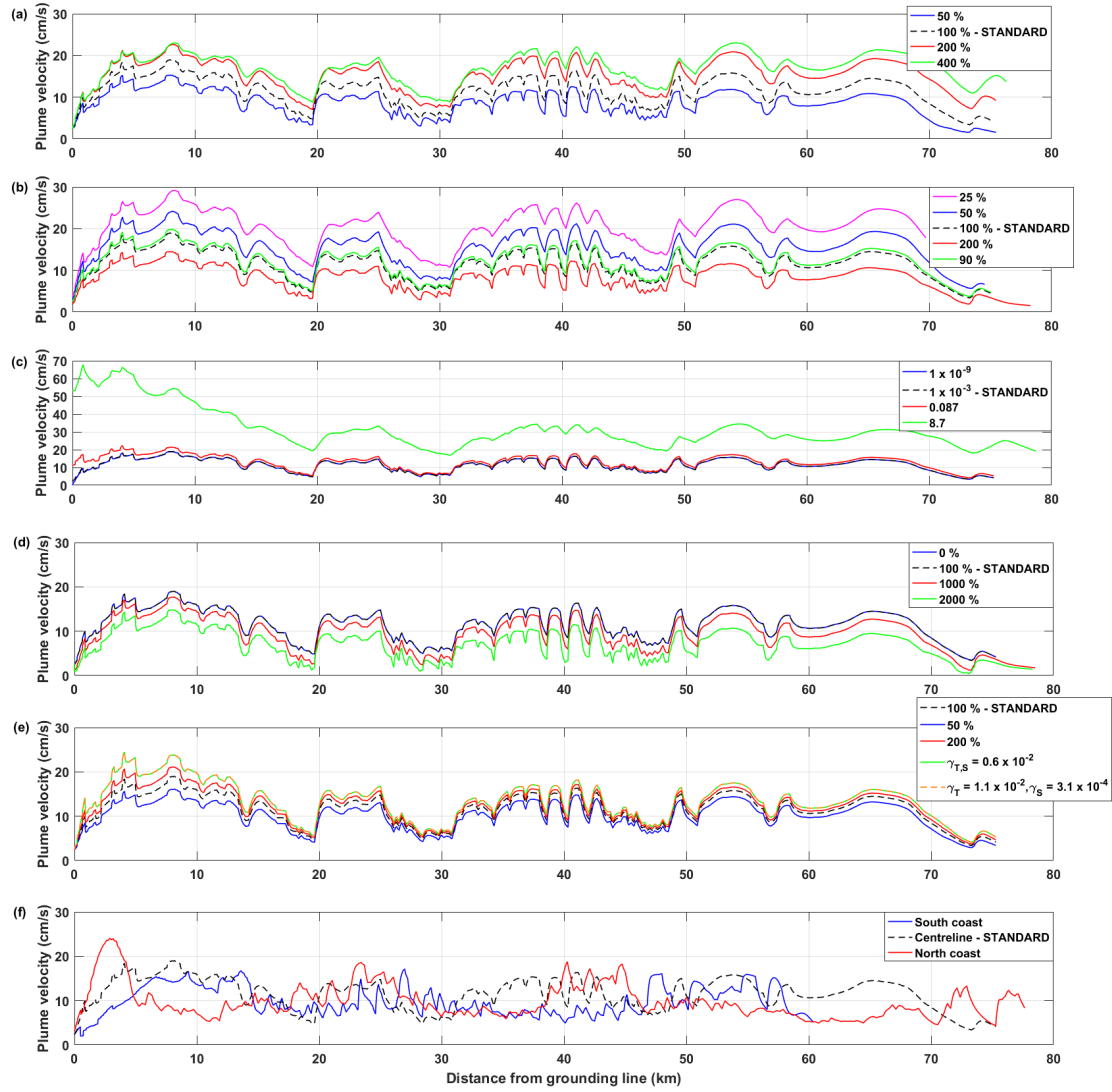
Figure 4.17: *Sensitivity of the plume velocity along the centreline of the 79NG ice tongue due to different parameters. (a) Entrainment coefficient, (b) drag coefficient, (c) subglacial discharge, (d) tidal flow, (e) turbulent transfer coefficients for heat and salt, and (f) ice base.*

the plume is less buoyant and rises slower along the ice base (Figure 4.17a, blue). Due to a slower plume, less AW is entrained and, hence, less heat is available for melting. Moreover, the plume needs longer to reach to travel from the GL toward the main front, about 12.8 days (Table 4.4). The plume thickness decreases because less AW is entrained and, thus, less freshwater is released due to reduced melting (Figure 4.18a, blue). As the melt rates, velocity, and thickness decrease the plume flux also decreases (Table 4.4).
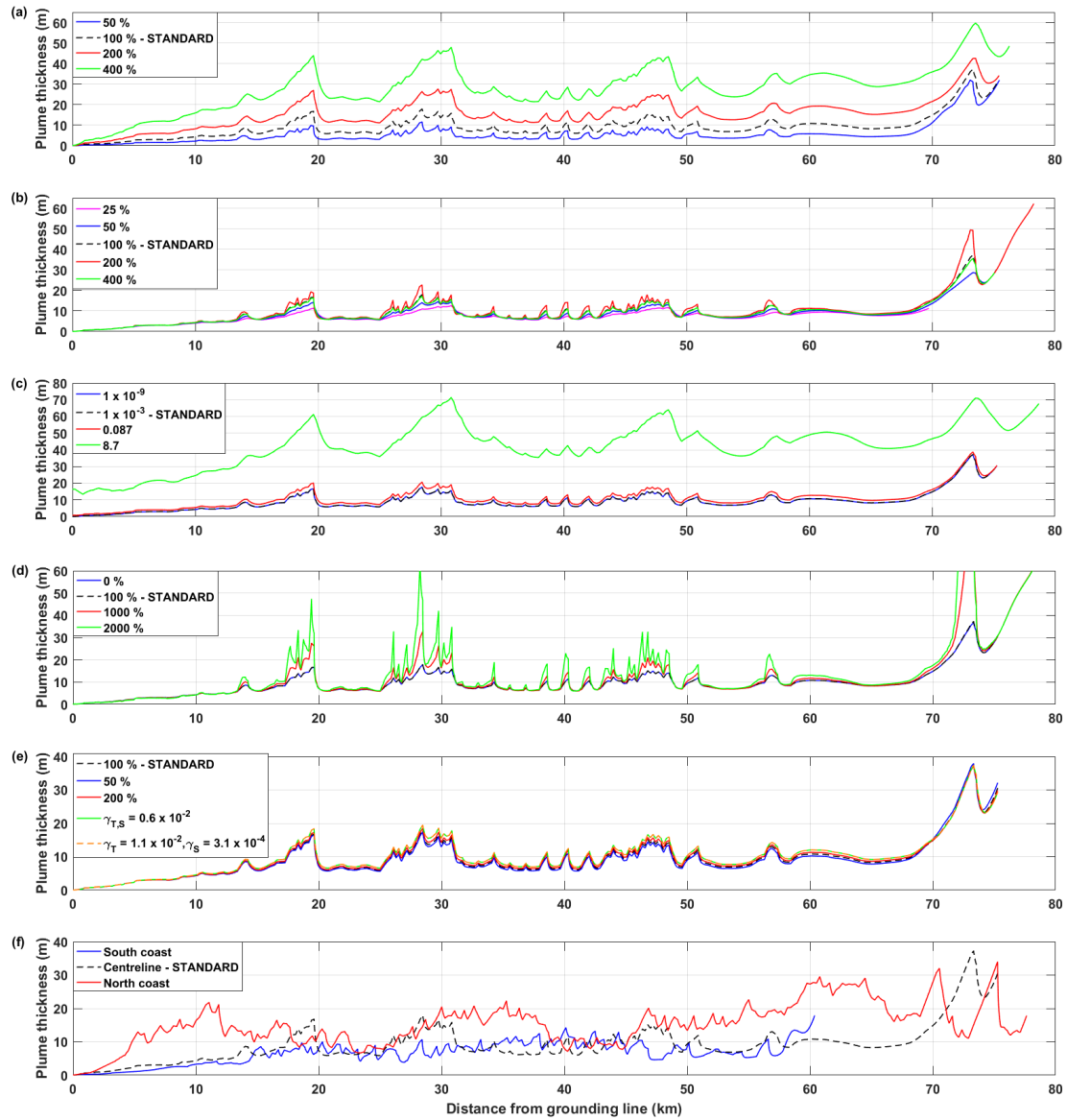
Figure 4.18: *Sensitivity of the plume thickness along the centreline of the 79NG ice tongue due to different parameters. (a) Entrainment coefficient, (b) drag coefficient, (c) subglacial discharge, (d) tidal flow, (e) turbulent transfer coefficients for heat and salt, and (f) ice base.*

Drag Coefficient

The standard value for the drag coefficient C_D used in this work is 9.7×10^{-3} (100 %). To understand how the drag coefficient influences the submarine melt rates and the plume dynamics along the ice base of the 79NG ice tongue, this parameter is changed over and compared to the range 25 % to 200 %. Using lower drag coefficients, 25 % (2.5×10^{-3}, magenta) and 50 % (4.9×10^{-3}, blue), results in a faster plume (Figure 4.17b). In contrast, a higher drag coefficient, 200 % (1.9×10^{-2}, red) leads to a slower plume. Generally, the melt rates are less sensitive to

the tested values for the drag coefficient than for the entrainment coefficient described above (Figure 4.16a, b and Table 4.4).

A higher plume velocity leads to more entrainment of AW and, thus, more melting (Figure 4.16b, magenta and blue, and Table 4.4). Mean melt rates increase to about $18\,\mathrm{m\,yr^{-1}}$ and $22\,\mathrm{m\,yr^{-1}}$ by reducing the drag to 50 % and 25 %. Maximum melt rates increase only notable for a 50 % lower drag to about $78\,\mathrm{m\,yr^{-1}}$. In addition, the turbulent transfer coefficients for heat and salt, $\gamma_{T,S}$, depend linearly on the plume velocity (Eq. 3.22 and 3.23). As the plume accelerates, heat supplied by the AW is transferred faster toward the ice base. The drag coefficient only determines $\gamma_{T,S}$ as the square root and, hence, has a weaker influence. The plume thickness decreases insignificantly (Figure 4.18b, magenta and blue). Due to the higher velocity the plume flows close to the main front in 6.2 days (50 % drag) and 4.2 days (25 % drag) (Table 4.4). However, the plume also travels a shorter distance, $70\,\mathrm{km}$ (25 % drag), as it reaches its level of neutral buoyancy earlier because of higher entrainment rates. Moreover, the melt rates are not largely increased and, thus, the additional freshwater seem not to be enough to increase the buoyancy sufficiently.

A slower plume, due to an increasing of the drag coefficient to 200 %, causes lower mean melt rates of about $11\,\mathrm{m\,yr^{-1}}$ (Figure 4.16b, red, and Table 4.4). Maximum melting decreases to about $68\,\mathrm{m\,yr^{-1}}$. In addition, the turbulent transfer of heat is reduced as a higher drag implies a decrease in velocity. The plume thickens to 50 - 60 m shortly before it detaches close to the main front (Figure 4.18b, red). This is associated with a drop below $5\,\mathrm{cm\,s^{-1}}$ of the plume velocity (Figure 4.17b, red). The plume travels a greater distance of about $78\,\mathrm{km}$ (Table 4.4). This is because it stays buoyant for a longer time as less AW is entrained even though less freshwater and, thus, buoyancy is added. The greater distance and the reduction in the velocity cause a much longer travel time of 13.8 days.

Subglacial Discharge

As the subglacial discharge $D_{X0}U_{X0}$ is highly unknown for 79NG, a very wide range of 1.0×10^{-9} - $8.7\,\mathrm{m^2\,s^{-1}}$ is applied to examine this sensitivity.

The standard value of $1.0 \times 10^{-3}\,\mathrm{m^2\,s^{-1}}$ is used to initiate the plume. The subglacial discharge was further lowered to $1 \times 10^{-9}\,\mathrm{m^2\,s^{-1}}$. Applying this value yields a decrease in the mean melt rate of about $9\,\mathrm{m\,yr^{-1}}$ whereas the maximum melt rate remains nearly constant (Figure 4.16c, blue, and Table 4.4). It is found that the plume evolution is independent of a lower limit of the subglacial discharge as it always started to evolve. However, using no subglacial discharge leads to an error in the plume formulation because of the expression for the initial plume thickness (Eq. 3.13).

The subglacial discharge can be estimated from the surface runoff. Andersen et al. (2010) de-

rived a surface runoff of $174 \, \text{m}^3 \, \text{s}^{-1}$ based on a surface-energy-balance model and observations from an automatic weather station during summers in 2007 and 2008. The area of the drainage basin of 79NG is with $103\,314 \, \text{km}^2$ as much as twice that of Helheim Glacier which is $48\,140 \, \text{km}^2$ (Rignot and Kanagaratnam, 2006). Thus, it is expected that the surface runoff at 79NG is also much higher. Moreover, high geothermal heat fluxes were measured at NEGIS (Fahnestock et al., 2001). In addition, a large marginal lake located in the north exists (Thomsen et al., 1997). The latter two imply also higher subglacial discharge. Therefore, a tenfold subglacial discharge of $1\,740 \, \text{m}^3 \, \text{s}^{-1}$ at 79NG is assumed which is rudimentary at all but is helpful to constrain its upper limit. Further, two scenarios are assumed. First, the subglacial discharge is distributed along the grounding line with $20 \, \text{km}$ width. This yield $0.087 \, \text{m}^2 \, \text{s}^{-1}$ per unit width. Second, the subglacial discharge is released at one specific point $200 \, \text{m}$ wide which gives $8.7 \, \text{m}^2 \, \text{s}^{-1}$ per unit width. Sciascia et al. (2013) did this for Helheim Glacier. In nature, many cracks, channels, and openings might exist where subglacial discharge is released. However, this is highly unknown. Moreover, the ISW plume model solves the problems along one dimension.

Increasing the subglacial discharge to $0.087 \, \text{m}^2 \, \text{s}^{-1}$ leads to higher mean melt rates of about $18 \, \text{m} \, \text{yr}^{-1}$ compared to $15 \, \text{m} \, \text{yr}^{-1}$ in the STANDARD (Figure 4.16c, red, and Table 4.4). The increase is strongest within the GLZ. Downstream of $30 \, \text{km}$ melting is nearly unaltered. The velocity increases slightly within the GLZ due to the added buoyancy provided by the subglacial discharge (Figrue 4.17c, red).

Further increase in subglacial discharge ($8.7 \, \text{m}^2 \, \text{s}^{-1}$) causes higher melt rates of about $25 \, \text{m} \, \text{yr}^{-1}$ (Figure 4.16c, green, and Table 4.4). The plume velocity and thickness are highly elevated, especially within the GLZ due to the high subglacial discharge which determines the initial velocity and thickness (Eq. 3.12 and 3.13).

Tidal Flow

The tidal flow used in the STANDARD is $1.18 \, \text{cm} \, \text{s}^{-1}$. It is an order of magnitude lower than the mean plume velocity (Figure 4.17d). Moreover, tides are fairly barotropic and, thus, do not influence the entrainment of AW.

Applying no tidal flow ($0\,\%$), has neither effects on the melting nor on the plume dynamics compared to the STANDARD tidal flow (Figures 4.16d, 4.17d, 4.18d, blue, and Table 4.4). However, increasing the tidal flow to tenfold (red) and twentyfold (green) the STANDARD value reduces the melt rates (Figure 4.16d). The mean melt rates decrease more than the maximum melt rate (Table 4.4). The response is supported by Smedsrud and Jenkins (2004). A stronger tidal flow increases the shear between the plume and the ice-ocean boundary and, thus, the drag. This causes the plume to flow down (4.17d) and, as a result, less AW is entrained which lead to less melting.

The turbulent transfer coefficients for heat and salt, $\gamma_{T,S}$, rise as a response to an elevated tidal flow (Eq. 3.22 and 3.23). However, if less heat is available in the plume due to reduced entrainment of AW, $\gamma_{T,S}$ only accelerate the exchange of the heat and salt that is available. What is more, the mean plume velocity reduces by more than $1.18\,\mathrm{cm\,s^{-1}}$ when increasing the tides (Figrue 4.17d). This counteracts the increase of $\gamma_{T,S}$ due to tides. Moreover, due to its reduced velocity and, hence, less entrainment of AW the plume stays longer buoyant even though less freshwater is added. This leads to a greater distance and travel time (Table 4.4). The plume thickens periodically consistent with a decrease in the plume velocity (Figure 4.17d and 4.18d, red and green) as tides increase mixing. Maximum thicknesses of about $90\,\mathrm{m}$ and $215\,\mathrm{m}$ are reached downstream of $70\,\mathrm{km}$.

Turbulent Transfer Coefficients for Heat and Salt

The turbulent transfer coefficients for heat and salt γ_T and γ_S (Eq. 3.22 and 3.23), dictate the molecular exchange of heat and salt through the oceanic boundary layer (Figure 3.4b). Choosing an adequate parameterization of these coefficients are key in simulating realistic melt rates and plume dynamics (Holland and Jenkins, 1999). Thus, changing $\gamma_{T,S}$ is expected to have great effects.

Decreasing $\gamma_{T,S}$ by $50\,\%$ results in lower melt rates within the GLZ and the TZ (Figure 4.16e, blue and Table 4.4). The mean melt rate decreases to about $11\,\mathrm{m\,yr^{-1}}$ and the maximum melt rates to roughly $44\,\mathrm{m\,yr^{-1}}$ (Table 4.4). Further downstream, melting is not significantly reduced. Melting decreases because the heat transfer toward the ice base is attenuated. Due to less melting, less freshwater is released which decreases the buoyancy and, thus, the plume velocity (Figure 4.17e, blue). In turn, less AW is entrained. A change in the plume thickness is almost not visible (Figure 4.18e, blue).

Increasing $\gamma_{T,S}$ to $200\,\%$ leads to elevated mean melting of about $17\,\mathrm{m\,yr^{-1}}$ (Figure 4.16e, red and Table 4.4). Within the GLZ, the effects are larger. The maximum melt rate increases to roughly $113\,\mathrm{m\,yr^{-1}}$. Melting attenuates down-glacier of about $15\,\mathrm{km}$ and is not significantly different from the STANDARD further downstream (Figure 4.16e, red). The plume speeds up everywhere along the ice base (Figure 4.17e, red). Within the GLT this is consistent with higher melt rates. Further downstream where melting is not changed the higher plume velocity is due to the released freshwater. The plume thickness does not change much (Figure 4.18e, red).

The influence of constant turbulent transfer coefficients is also evaluated. Therefore, the value 0.6×10^{-2} for both γ_T and γ_S is applied. Further, because on the molecular level heat and salt are diffused on different rates, the model is run using $\gamma_T = 1.1 \times 10^{-2}$ and $\gamma_S = 3.1 \times 10^{-4}$. Using the constant value 0.6×10^{-2} increases the melting within the GLZ periodically very much ((Figure 4.16e, green) . Within the TZ, the melt rates decrease. Further downstream, melting shows an alternating pattern between higher and lower melting compared to the STANDARD

(black). The mean melt rate increases to about $21\,\text{m}\,\text{yr}^{-1}$ and the maximum melting to about $232\,\text{m}\,\text{yr}^{-1}$ (Table 4.4). The plume velocity further increases (Figure 4.17e, green) whereas the plume thickness remains fairly constant (Figure 4.18e, green). Applying different constants for γ_T (1.1×10^{-2}) and γ_S (3.1×10^{-4}) with the turbulent transfer coefficient for heat being two orders of magnitude larger than that for salt, does not result in significant changes compared to the latter case, neither in the melting (Figure 4.16e, orange, and Table 4.4) nor in the plume velocity (Figure 4.17e, orange) and thickness (Figure 4.18e, orange).

Ice Base

The ice base of the 79NG varies not only along its ice tongue but also change across it (Figures 3.5 and 4.14). The thickest ice base is concentrated along the centreline consistent with the fastest ice flow (Mouginot et al., 2015). Towards the margins the ice base thins. This is due to a higher lateral drag along the margins that counteracts the ice flow (Benn and Evans, 2010). The spatial distribution of the ice base has influences on the submarine melt rates and the plume dynamics.

Along the north coast (Figures 3.5 and 4.14) melt rates are much higher within the GLZ compared to the STANDARD (Figure 4.16f, red). The mean melt rate is with about $19\,\text{m}\,\text{yr}^{-1}$ larger compared to $15\,\text{m}\,\text{yr}^{-1}$ along the centreline (STANDARD) (Table 4.4). Maximum melting is much larger with about $144\,\text{m}\,\text{yr}^{-1}$ compared to $75\,\text{m}\,\text{yr}^{-1}$. It drops very quickly to about $25\,\text{m}\,\text{yr}^{-1}$ at 10 km. A TZ does not exist and the melt rates stay relatively constant within about 25 km. Further down-glacier, the melting decreases continuously to about 1 - $2\,\text{m}\,\text{yr}^{-1}$ before the plume detaches. The plume velocity increases rapidly within 3 km of the GLZ to its maximum of about $24\,\text{cm}\,\text{s}^{-1}$ (Figure 4.17f, red). In that region, the plume is about 5 - $6\,\text{cm}\,\text{s}^{-1}$ faster than along the centreline (STANDARD). In the mean, the velocity does not increase but regions of fast flow and low flow compared to the STANDARD exist. The high velocity within the GLZ is caused by the steep slope of the ice base (Figure 4.13, red and 4.14c). Coupled to that is an elevated entrainment of AW. As a result, larger melting occurs. Due to the higher entrainment and freshwater amount, the plume thickens in the mean (Figure 4.18f, red). The plume travels farther (78 km) and for a longer time (10.4 days) because of the higher buoyancy (Table 4.4)

The melt rates along the south coast are slightly lower than along the centreline (Figure 4.16f, blue). Mean melting is about $11\,\text{m}\,\text{yr}^{-1}$ (Table 4.4). The peak in the melt rates occurs further downstream from the GL and is attenuated to about $50\,\text{m}\,\text{yr}^{-1}$ compared to $75\,\text{m}\,\text{yr}^{-1}$ in the STANDARD. Further, melt rates decay within 15 km, stay relatively constant for about 10 km, and then drop to near zero. The plume velocity rises slower within the GLZ (Figure 4.17f, blue) due to a more gentle slope (Figure 4.13, blue). However, the mean is comparable to the STANDARD. This is the same for the plume thickness (Figure 4.18f, blue). The plume gets

neurally buoyant at about 60 km and travels this distance within 7.9 days (Table 4.4).

4.4.3   AW Temperature in the Cavity below the 79NG Ice Tongue

Rift Profile

The main question investigated in this study is the response of submarine melt rates and plume dynamics due to a warming ocean. Since the 1950s, the upper ocean heat content of the Atlantic Meridional Overturning Circulation has increased (Straneo and Heimbach, 2013). Additional to that, an anomalous inflow of subtropical waters driven by atmospheric changes and multidecadal natural ocean variability led to a warming of the Subpolar North Atlantic (Straneo and Heimbach, 2013). It is suggested that this signal propagates also toward the Arctic Ocean (Figure 2.1). Undeniably, during the last decades the ocean temperature north of Spitsbergen (Onarheim et al., 2014), across Fram Strait (Beszczynska-Möller et al., 2012), in the Norske Trough (Schaffer et al., 2017), and in the Eurasian Basin (Schauer et al., 2004) has increased. As a result of the warming, the submarine melting increased at many marine-terminating glaciers of Greenland (Straneo and Heimbach, 2013). It is very important to constrain the submarine melt rates along the 79NG ice tongue corresponding to an ocean warming.

In this regard, the AW temperature in the cavity was increased by increments of $0.5\,°C$. As a result, the AW temperature ranges between $0\,°C$ and $4\,°C$. Melt rates are expected to increase with rising temperatures.

Indeed, the 1D ISW plume model simulates that the melt rates (mean and maximum) along the centreline of the 79NG ice tongue increase close to linearly with AW temperature (Figure 4.19). However, also a quadratically dependence exist yet this is weaker.

Warming the AW by $0.5\,°C$ would increase the mean melt rate to about $19\,\mathrm{m\,yr^{-1}}$ compared to $15\,\mathrm{m\,yr^{-1}}$ for the STANDARD (Figure 4.20a, blue and black, and Table 4.4). Maximum melting rises from $75\,\mathrm{m\,yr^{-1}}$ to $95\,\mathrm{m\,yr^{-1}}$. The spatial distribution of the melting does not alter when further increasing the temperature by up to $3°C$ (Figure 4.20a). The highest mean melt rate simulated is about $43\,\mathrm{m\,yr^{-1}}$ (Figure 4.20a, orange and Table 4.4). The corresponding maximum melting is $211\,\mathrm{m\,yr^{-1}}$.

In the warmest scenario, the AW temperature is about $6.3°C$ higher than the in-situ freezing point close to the GL (Figure 4.20b, orange). This is about $3°C$ higher than for the STANDARD (black) explaining the highly elevated melt rates.

Highest plume temperatures with up to about $1°C$ are found within about 1 km of the GL (Figure 4.20c, orange). Within 1 km downstream the plume temperature drops to a local minimum before it rises to another peak at about 4 km. This pattern is consistent with the melting (Figure 4.20a, orange). Between 10 km and 20 km downstream of the GL the temperature decreases. The

The plot contains the equations:

$$m_{max} = 2.703\, T_a^2 + 31.780\, T_a + 41.094$$
$$(r^2 = 0.999)$$

$$m_{mean} = 0.625\, T_a^2 + 6.887\, T_a + 10.483$$
$$(r^2 = 0.998)$$
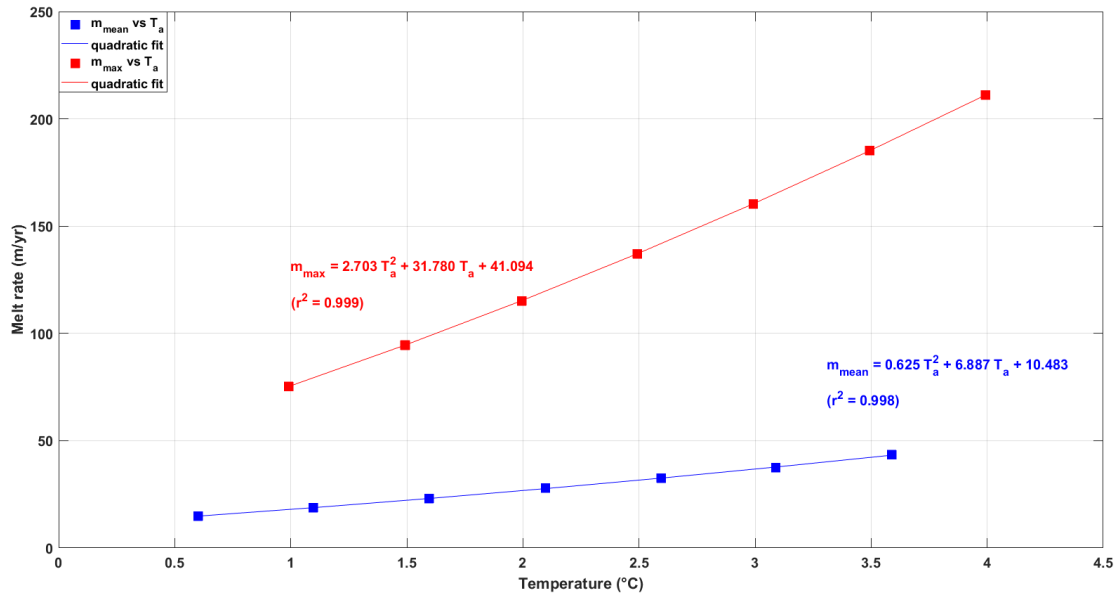
Figure 4.19: Mean (blue) and maximum (red) melt rate dependence on AW temperature along the centreline of the 79NG ice tongue for a warming ocean scenario as described in the text.

gradient varies between 0.4°C for the STANDARD (black) and 0.9°C for the warmest scenario (orange). Thus, the warmer AW the stronger the gradient in that region. Further downstream the temperature continuously falls. At the location where the plume reaches its level of neutral buoyancy the contrast in the plume temperature between the applied scenarios is smallest.

The salinity of the plume reveals a similar pattern as the plume temperature (Figure 4.20d). However, in contrast to the temperature evolution, the salinity decreases with warming of AW. The plume is saltiest close to the GLZ and continuously freshens along the ice base due to the additional freshwater caused by melting (Figure 4.20a, d). The gradient in salinity along the ice base is about 0.66 psu in the STANDARD (black). For the warmest scenario (orange) it is much higher with about 1.16 psu.

The plume velocity increases steadily with increasing AW temperature due to more freshwater and, thus, buoyancy (Figure 4.20e). Along roughly the first km the increase is smallest. A change in the thickness of the plume (Figure 4.20f) is not evident within 60 km. Downstream from that location the thickness decreases with the warming. The maximum difference between the STANDARD case (black) and warmest case (orange) is on the order of 10 m.

Norske Trough - ECCOv4

In the following, results from simulations using the 1D ISW plume model with a range in AW properties in the Norske Trough from ECCOv4 for the period 1992-2015 are described. The response of the submarine melt rates to variations in the AW temperature and its presence in
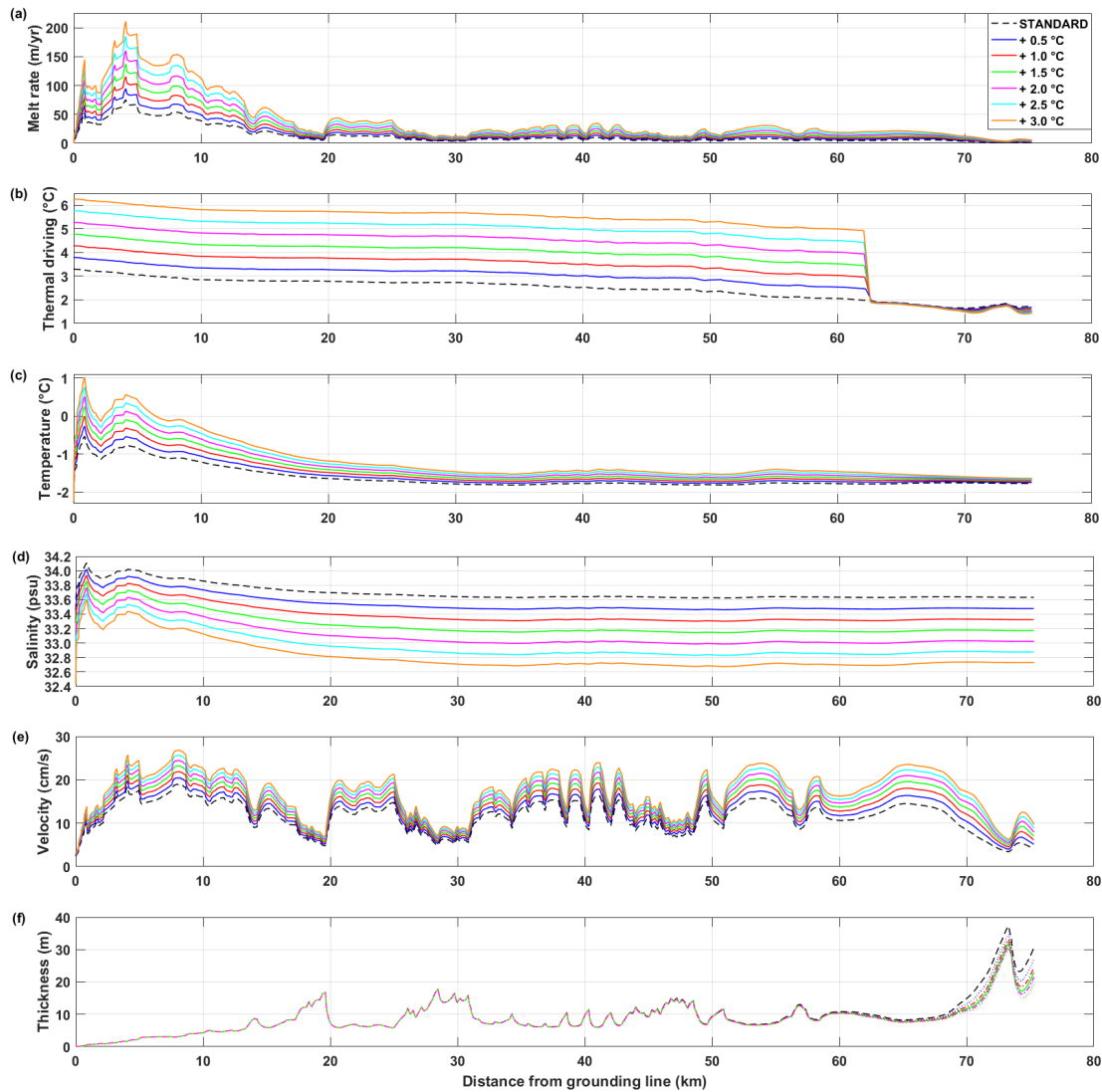
Figure 4.20: *Sensitivity of (a) submarine melt rate, (b) thermal driving (T_a-T_f), (c) plume temperature, (d) plume salinity, (e) plume velocity, and (f) plume thickness along the centreline of 79NG to a warming ocean.*

the water column (Figure 4.12 and Table 4.2) are investigated. It is assumed that the properties simulated in the Norske Trough are applicable to the hydrography in the cavity beneath the 79NG ice tongue because ECCOv4 does not have an ice tongue. The AW temperature at 300 m ranges between 0.1 °C (cold AW) and 1.3 °C (warm AW). Further, ECCOv4 simulated AW as shallow as 200 m (shallow AW) and as deep as 255 m (deep AW) in the Norske Trough. Corresponding to the ranges, the CTD profile taken in the rift was adjusted accordingly (Figure 4.21). The variation in AW salinity was not examined here.

The 1D ISW model simulates a range in mean submarine melt rates of 10 m yr^{-1} - 19 m yr^{-1} along the centreline of the 79NG ice tongue. Maximum melting occurs within the GLZ and varies between 55 m yr^{-1} and 98 m yr^{-1}. In the warm AW case (red) melting increased every-
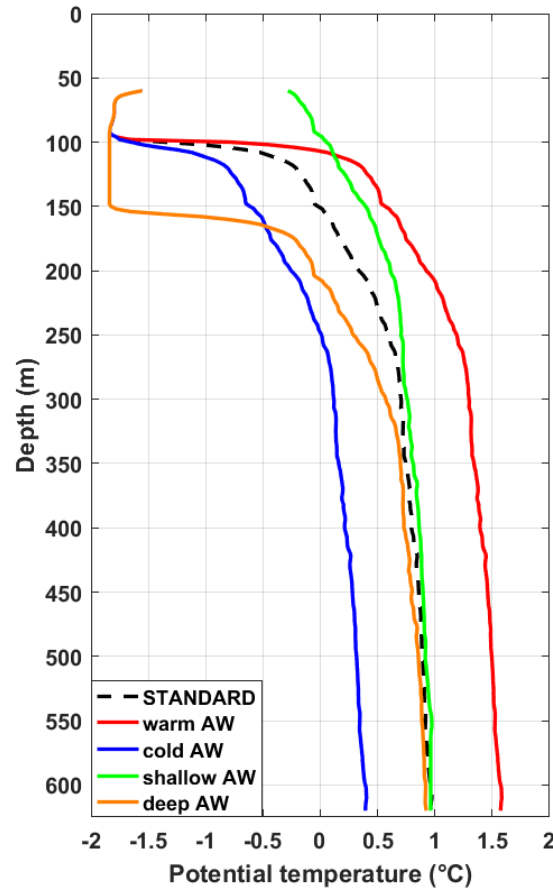
Figure 4.21: Potential temperature in the cavity below the 79NG ice tongue from the rift profile close to the northern front (black dashed). Warm AW (red), cold AW (blue), shallow AW (green), and deep AW (orange) as simulated by the ECCOv4 in the Norske Trough for the period 1992-2015. The locations of the CTD stations are shown in Figure 3.1. Temperatures > 0 °C and salinity > 34.3 psu (not shown) define AW.
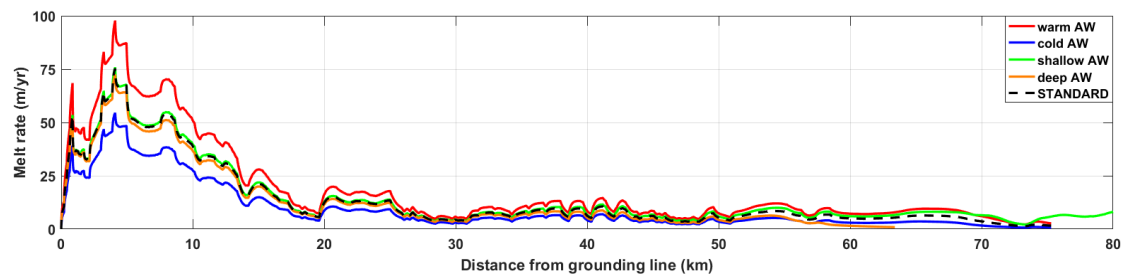
Figure 4.22: Submarine melt rates simulated by the 1D ISW plume model using variations in AW temperature and presence in the water column in the Norske Trough from the ECCOv4 for the period 19992-2015. The STANDARD CTD profile is the rift profile (black dashed). Warm AW (red), cold AW (blue), shallow AW (green), and deep AW (orange). The locations of the CTD stations are shown in Figure 3.1.

where along the ice base (Figure 4.22). The increase is most pronounced in the GLZ. The mean melt rate increased to about $19\,\mathrm{m\,yr^{-1}}$ (Table 4.2). In the cold AW case (blue) melting decreased,

Model run	Mean melt rate (m yr^{-1})	Maximum melt rate (m yr^{-1})	Point of detachment (km)	Final plume flux $(\text{m}^3\,\text{s}^{-1})$	Travel time (days)
Standard	14.8	75.3	75.3	38 100	8.7
warm AW	19.3	97.7	75.3	42 121	7.7
cold AW	10.2	54.5	75.3	33 474	10.2
shallow AW	15.1	75.8	80.0	41 735	8.3
deep AW	14.7	72.5	63.4	33 113	8.6

Table 4.5: Sensitivity of the model results along the centreline of the 79NG ice tongue due to variations in AW temperature and presence in the water column simulated in the Norske Trough by ECCOv4 for the period 1992-2015.

strongest within the GLZ. The mean melt rate decreased to about $10\,\text{m yr}^{-1}$. Bringing AW closer to the ice base (shallow AW, green) and deeper into the water column (deep AW, orange) alters the melting not significantly within 50 km (Figure 4.22 and Table 4.2). Further downstream, melting changes slightly with an increase in the shallow AW case and a decrease in the deep AW case.

4.4.4   Stability of the 79NG ice tongue

The simulated mean melt rates are used to asses the stability of the 79NG ice tongue. A very simple approach is followed that enables to estimate how long it takes for the ice tongue to completely melt down. In this case, it is assumed that ice flow from up-glacier is zero. In addition, the freshwater released onto the continental shelf of Northeast Greenland is quantified. Mean melt rates were simulated along three flow lines: the centreline of the ice tongue, the southern coast, and the northern coast (Figure 3.5). The mean melt rates are $14.8\,\text{m yr}^{-1}$, $11.6\,\text{m yr}^{-1}$, and $18.6\,\text{m yr}^{-1}$ (Table 4.6). The corresponding mean ice thicknesses, ice base plus ice elevation, along these lines are 255.5 m, 218.5 m, and 201.4 m. Applying the mean melt rates to the mean thickness is in such reasonable because even so a lot higher melt rates are found within the GLZ but the thickness is greater there. As a result, the 79NG ice tongue would completely melt within about 17.3 yr, 18.8 yr, and 10.8 yr (Table 4.6). Considering the mean melt rate along the centreline, the south coast, and the north coast, $15\,\text{m yr}^{-1}$, and the total mean ice thickness of the floating ice tongue, 223.2 m, results in a mean melt time of about 14.9 yr. Schaffer et al. (2017) observed AW warming in the Norske Trough. Taken this into account, the simulated mean melt rate of $18.9\,\text{m yr}^{-1}$ would lead to a complete melt down within 13.5 yr.

 Further, the variations in AW properties simulated from ECCOv4 yield melt rates between $10.2\,\text{m yr}^{-1}$ (cold AW) and $19.3\,\text{m yr}^{-1}$ (warm AW) (Table 4.6). The corresponding melt time ranges between 11.6 yr and 21.9 yr.

Melting along the ice base of ice tongue of 79NG leads to a freshwater flux which is transported

Model run	Mean melt rate (m yr^{-1})	Mean ice thickness (m)	Mean melt time (yr)	Freshwater flux (km^3 yr^{-1}) / (mSv)
centreline - STANDARD	14.8	255.5	17.3	27.6 / 0.9
south coast	11.6	218.5	18.8	21.7 / 0.7
north coast	18.6	201.4	10.8	34.7 / 1.1
mean	15.0	223.2	14.9	28.0 / 0.9
+0.5 °C	18.9	255.5	13.5	35.2 / 1.1
warm case	19.3	223.2	11.6	36.0 / 1.1
cold case	10.2	223.2	21.9	19.0 / 0.6
shallow AW	15.1	223.2	14.8	28.2 / 0.9
deeper AW	14.7	223.2	15.2	27.4 / 0.9

Table 4.6

in the plume. It is assumed that it enters the continental shelf of Northeast Greenland via the main front in the east and through Dijmphna Sund in the north. The freshwater flux (FWF) is calculated in a very simple way:

$$FWF = \frac{m_{mean} \times L \times (\frac{2}{3} \times width_{up} + \frac{1}{3} \times width_{down})}{31557600 \times 10^6}, \quad (4.1)$$

where m$_{mean}$ is the mean melt rate, L the length of the ice tongue, width$_{up}$ = 20 km the width that is representative for the upper 2/3 of the ice tongue, and width$_{down}$ = 30 km the width that is representative for the lower 1/3. The values in the denominator are used to convert from km^3 yr^{-1} into Sv. The range in the FWF is 19 km^3 yr^{-1} (0.6 mSv) to 36 km^3 yr^{-1} (1.1 mSv) (Table 4.6).

5. Discussion

5.1 Hydrography

5.1.1 Fram Strait and Continental Shelf

Observations obtained during FS2016 across Fram Strait were collected between the two recirculation pathways at approximately 78 °50′N and 80 °N suggested by Beszczynska-Möller et al. (2012) and Hattermann et al. (2016) (Figure 2.1 and 3.1). The data confirm that AW recirculates across Fram Strait.

The highest temperature is found at the surface offshore Spitsbergen and, thus, at the same location as the highest temperatures measured from moorings between 1997 and 2010 (Beszczynska-Möller et al., 2012). AW is observed to cool across Fram Strait. This is most likely due to heat loss to the atmosphere, interacting with sea ice, and mixing with cold and fresh PW (e.g., Beszczynska-Möller et al. (2012)).

Beszczynska-Möller et al. (2012) found a mean AW temperature of $3.1 \pm 0.1\,°\mathrm{C}$. The mean core AW temperature across Fram Strait measured during FS2016 is with about $2.5\,°\mathrm{C}$ much lower. However, direct comparison is not recommended. Observations from only a few CTD profiles obtained during a few days is not comparable to a long-term mean taking into account all seasons. Moreover, Beszczynska-Möller et al. (2012) define AW warmer than $2\,°\mathrm{C}$ in contrast to $0\,°\mathrm{C}$ used here.

The eddy-like feature offshore the Continental Shelf clearly shows AW properties and, hence, most likely causes the lateral mixing of warm AW across Fram Strait and onto the shelf as discussed by Hattermann et al. (2016). Maximum temperatures on the shelf are about $1.3\,°\mathrm{C}$. This water has the potential to reach the 79NG and the cavity below its ice tongue. Deep AW present on the Continental Shelf and offshore probably flows further south to the deep opening at the shelf break and into the Norske Trough (Figure 3.1). Surface and subsurface waters in the Norske Trough might also stem from the Continental Shelf.

5.1.2 Norske Trough

Water properties at about 250 m depth on the shelf and also just offshore are very similar to the AW present in the Norske Trough at this depth. This indicates the close connection between the recirculating AW, the AW present on the shelf, and AW in Norske Trough. Moreover, the waters in Norske Trough are found to be a product of mixing between recirculating AW and PW, and cooling. Thus, the observations obtained during FS2016 support the circulation pathways of AW suggested by, e.g., Schaffer et al. (2017).

The very cold mixed layer present between 40 m and 100 m might either be created by sea ice melting or glacial meltwater-modified water and/or glacial runoff-modified water which was also found by Mayer et al. (2000) and Wilson and Straneo (2015) during previous surveys. The outflow of these waters takes place through both the main front in the east and the front in the north facing Dijmphna Sund. These pathways are suggested by Wilson and Straneo (2015) and, to some extent, confirmed by the velocity measurements from the ITM5 (Section 4.2.1).

The strong stratification between the very cold mixed layer and the AW at depths may suppress upward heat flux supplied by AW. Thus, the sea ice that seasonally exists in this area is protected from getting in contact with warmer waters. In turn, the sea ice stabilizes the 79NG (Reeh et al., 2001; Straneo et al., 2012; Wilson and Straneo, 2015). The semi-permanent sea ice connected to the ice tongue makes it more stable towards calving events. In addition, sea ice melt stratifies the water column and, thus, upward heat transport is reduced (Mayer et al., 2000). In this context, Mayer et al. (2000) states that less or colder AW lead to less melting along the ice base of 79NG glacier. This is supported by results from the ISW plume model in this study (e.g. Sections 4.4.3 and 5.4.4). The mean melt rate obtained from applying the model to three flow lines along the 79NG ice tongue is $15.0 \, \mathrm{m \, yr^{-1}}$. Using Eq. 4.1 yields a freshwater flux of $28.0 \, \mathrm{km^3 \, yr^{-1}}$ (0.89 mSv) (Table 4.6). In the cold AW case based on the ECCOv4 mean melting is reduced to $10.2 \, \mathrm{m \, yr^{-1}}$ corresponding to a freshwater flux of $19.0 \, \mathrm{km^3 \, yr^{-1}}$ (0.60 mSv). This gives a reduction by about 32 %. As less meltwater is available to maintain a stratified water column the sea ice is more susceptible to melting due to the underlying AW, and, thus, the stabilization of the ice tongue might be reduced.

On the other hand, the AW is not very susceptible to heat loss toward the atmosphere and the sea ice above or due to mixing with the cold water. Consequently, AW with a maximum temperature of $1.8 \, ^\circ\mathrm{C}$ is probably the warmest water that potentially flow toward the main front of 79NG and into the cavity below. The high temperature is due to a warming of AW in Norske Trough by $0.5 \, ^\circ\mathrm{C}$ from the period 1979-1999 to 2000-2016 observed by Schaffer et al. (2017). However, maximum temperatures in the cavity from the rift profile are about $1.0 \, ^\circ\mathrm{C}$ (Wilson and Straneo, 2015) and, thus, colder. Waters are also fresher than found in Norske Trough. This might be evidence for AW cooling after all and probably mixing with colder and fresher water

from above. On the contrary, data in the cavity were obtained in September 2009 whereas the data from the Norske Trough in September 2016. Therefore, a possibility is that the water in the cavity have warmed during the last 7 years as also the maximum temperature in Norske Trough during that survey was below 1.5 °C. However, the profiles in Norske Trough in 2009 were performed north of the 79NG main front where Schaffer et al. (2017) generally find lower temperatures. This makes it once again clear that new and periodic measurements are needed. It is also possible that the deep AW in the cavity is colder and fresher than in Norske Trough due to mixing with freshwater released by submarine meltwater or with subglacial discharge. In this case, the measurements in the cavity might indicate that AW indeed reaches the grounding line and drives submarine melting.

5.1.3   Dijmphna Sund and Westwind Trough

During FS2016 Dimphna Sund was mostly sea ice free. This might have resulted in the very fresh and warm surface layer in the uppermost 20 - 30 m (Figure 4.4a, b and 4.6). Similar conditions were encountered by Mayer et al. (2000) which found high summer air temperatures (0 - 4 °C) and that solar radiation explained the warm surface layer. The low salinity values are probably due to released freshwater during sea ice melt or surface runoff.

The very cold mixed layer found between about 50 and 80 m (Figure 4.4a, b) is believed to be an indicator for MMW and/or RMW. This layer stratifies the water column and act as a barrier between the AW and the overlying PSW and PSWw. Such a layer was a also found by Mayer et al. (2000) and Wilson and Straneo (2015) and described as buoyant meltwater between the warm surface layer and the deep AW.

The deep AW fall along the meltwater mixing line (Figure 4.7). This indicates a mixture between AW and glacial meltwater-modified water and is most likely an evidence for AW driving melting in the cavity. The properties from the rift profile and in Dijmphna Sund obtained during AS2009 veer against the runoff mixing line (Figure 4.7 inlet and Section 2.4.1). This suggests that also RMW is present. The rift profile reveals veering starting at about 300 m indicating that glacial runoff-modified water exists above this depths (Wilson and Straneo, 2015). During FS2016, no clear evidence for glacial runoff-modified water was found in Dijmphna Sund based on this interpretation. However, it might be possible that the profiles during AS2009 were taken where some pools of RMW were present. The measurements during FS2016 were slightly taken at different locations (Figure 4.7 map). The surface of Dijmphna Sund was occupied by cold PSW (Figure 4.7). It might be that in 2009 sea ice was present limiting surface solar heating.

The surface layer in Westwind Trough consists of much colder PSW (Figure 4.4a, b and 4.6). During FS2016, sea ice was present in the trough which most likely explain the low temperatures. The AW properties are different for Dijmphna Sund and Westwind Trough. At 300 m depth

the contrast in temperature is 0.3 °C and in salinity 0.15 psu with Westwind Trough profiles being warmer and saltier at this depth (Figure 4.4c). The sill present at the mouth of Dijmphna Sund (Figure 2.10d and 4.6) has the potential to restrict the exchange of AW below between Dijpmhna Sund and the Westwind Trough. Most likely this is the reason for deep waters being largely different. It once hints to that AW enters the cavity via the main front in the east rather than through Dijmphna Sund. AW drives melting along the ice base and is transformed to a colder and fresher mixture of glacial meltwater-modified water and/or glacial runoff-modified water, consistent with Wilson and Straneo (2015) and Schaffer et al. (2017).

5.2 Ice-Tethered Mooring (ITM) and Tidal Analysis

5.2.1 Mean flow

Current velocities in the cavity are on the order of 5 to $10 \, \mathrm{cm \, s^{-1}}$ coinciding with findings from Schaffer et al. (2017). According to their results, AW is transported by a mean northwestward boundary current with velocities of $5 \, \mathrm{cm \, s^{-1}}$ from the continental shelf via the Norske Trough towards the main front of 79NG.

A westward directed flow during the first 30 days of the measurement period at 250 m, 370 m, and 500 m depth exist. This may indicate an inflow into the cavity through the main front. Most likely trough a more than 300 m deep channel as proposed by Schaffer et al. (2017) and evident in RTopo2 (Figure 2.10a). The average current strength is strongest at 250 m, suggesting that the majority of AW enters the cavity at this depth and reaches the grounding line within about 30 days. Further, the data might document that the flow follows the northern coast of the fjord for the remaining 60 days and leaves the cavity through Dijmphna Sund in the northeast. Wilson and Straneo (2015) also suggest a major part of the water to leave through Dijmphna Sund (Figure 2.9). At 165 m, periodically events exist where the flow is directed eastward indicating the existence of an outflow, probably of the plume, toward the main front. This is consistent with Wilson and Straneo (2015) (Figure 2.9). For the subsequent 60 days, a general outflow toward the main front at 165 m, 250 m, and 370 m is measured. At 500 m, the flow is directed toward south most likely influenced by the Coriolis force.

5.2.2 Tidal flow

The mean tidal flow is with 0.93 to $1.18 \, \mathrm{cm \, s^{-1}}$ quite weak. It is strongest in the north/south component. This is expected as the Greenland coast runs from south to north causing a weakening of the east/west component. Tides only explain a minor part of the variability in

the velocity field. Thus, the variability might be induced by the winds on the continental shelf. In addition, eddies propagating across Fram Strait and onto the continental shelf probably following the complex bathymetry along Norske Trough toward the main front of 79NG. Therefore, they potentially affect the current situation in the cavity, too.

Thomsen et al. (1997) measured tidal displacements of the floating ice tongue of about 1 m within 12 hours. This supports that the M2 tide with a frequency of 12.42 hours is the strongest component. Further, oscillations of the floating ice tongue of about 1.5 m were observed at the main front (Straneo F. (2017), personal communication).

Mean bedrock is 385.92 m.

These findings disagree with the calculated tidal flow in the cavity.

It is possible that parts of the ice base reaching deeper into the ater column block tidal effects. However, no evidence for that is presented. The most important tidal components, O1, K1, N2, M2, and S2, are fairly barotropic indicating good quality velocity data.

5.3   Ocean Reanalysis - ECCOv4

5.3.1   Fram Strait and Continental Shelf

The mean AW core temperature is with about $1.0\,^\circ$C much colder across Fram Strait in ECCOv4 compared to the observations during FS2016. During August and September 2016 AW might have been anomalous warm. De Steur et al. (2014) observed an anomalous warm recirculation in 2005 and 2007. Beszczynska-Möller et al. (2012) observed two periods of intensified warming and spreading of AW across Fram in late 1999-2000 and between late 2004 and 2008 (Figure 2.3). Temperatures on the Continental Shelf are comparable. However, direct comparison between a long-term mean which includes all seasons and a few CTD stations representative at best for two month is not recommended. Nonetheless, as ECCOv4 assimilates observations model drift is avoided (Forget et al., 2015) and, hence, results are trustworthy. Yet, data are rare in the study region, especially on the western side of Fram Strait and on the continental shelf of Greenland (Figure 3.7).

Many studies suggest a general warming trend of AW in that region. Onarheim et al. (2014) observed AW warming by $1.1\,^\circ$C along a section just south of Spitsbergen between 1979 - 2012 based on measurements from the upper 50 m - 200 m collected between August and October each year. The high temperatures observed during FS2016 exceed this trend. It is likely, that in 2016 surface and subsurface AW were anomalously high compared to the 20-year mean in ECCOv4 and to the linear trend stated by Onarheim et al. (2014). A possible explanation might be that waters were subject to elevated solar radiation and air temperatures. Beszczynska-Möller

et al. (2012) found a minimum in AW temperature in the West Spitsbergen Core of about 2.5 °C in 1997 and a maximum of about 3.6 °C in 2006. The highest temperature of 4.4 °C is found between the surface and 150 m (Figure 2.2b) compared to 3.1 °C in ECCOv4 and 7.5 °C in FS2016. This suggests that in 2016 temperatures were very high compared to the long-term mean found in ECCOv4 and from mooring data by Beszczynska-Möller et al. (2012).

ECCOv4 reproduces the location of the maximum temperatures in the surface layer offshore from Spitsbergen. Moreover, the cooling of AW across Fram Strait is reflected. In addition, the modeled EGC in upper 100 m to 200 m is similar to the one observed during FS2016. The large-scale eddy observed during FS2016 offshore the Continental Shelf is not found in ECCOv4. It is possible that eddies are not resolved in ECCOv4 due to the coarse grid. The horizontal spacing of the CTD profiles is about 40 km (Figure 3.1 and Forget et al. (2015)). The first baroclinic radius of deformation is about 2.6 km in the study area (Nurser and Bacon, 2014). Thus, eddies are not resolved but parameterized. However, Hattermann et al. (2016) found the eddy kinetic energy exceeding the mean kinetic energy in winter and, thus, the westward mixing of AW properties due to eddies strongest. The ECCOv4 section shows the mean situation for 24 years. Hence, eddies occuring during one season might be eroded by the mean flow. The situation during FS2016 might have been extraordinary and, therefore, eddies might have survived influences form the EGC and winters. In contrast, profiles during FS2016 where the eddy is found are more dense. Thus, eddies are resolved.

5.3.2 Norske Trough

Variations in both temperature and salinity in the upper 50 m of the Norske Trough are very likely driven by sea ice formation and melting (Figure 4.12). In ECCOv4, sea ice carries 0 °C and 4 psu salinity. Within 10 m from the surface other forcings such as solar heating, precipitation, and wind have great influences of the properties. The temperature and salinity vary approximately by 0.4 °C to 1.2 °C and 1.1 psu to 1.5 psu. This annual fluctuations make evident that the sea ice situation in Norske Trough is highly variable. During sea ice formation salt is incorporated into the ice skeleton. As a result, a layer of cold and fresh water is left behind just below the ice-ocean boundary. By time, brine is rejected in the underlying water layer. As a result, the salinity increases. The distribution of the brine in the water column is parameterized. It is possible for convection to start. In this case, the entire water column can be affected by the properties in the surface layer. If the stratification between the AW and the cold halocline is eroded AW losses its heat toward the upper layers and the atmosphere. On the other hand, during melting a large content of freshwater is added to the surface layer. This lead to the formation of a very stratified surface layer that acts as an barrier to the underlying water column. Thus, the presence of sea ice and its variation in the NT have major consequences for

the hydrographic situation and the heat loss of AW at depth. What is more, the AW that flows toward the main front of 79NG and into the cavity beneath its ice tongue is highly controlled by these processes. As AW present in the cavity drives melting along the ice base, it is crucial to determine the variations in AW properties.

The ECCOv4 yield a range in AW temperature of 0.1 °C to 1.3 °C at 300 m depth in the Norske Trough between 1992-2015 for both August and September (Figure 4.12). This gives a upper temperature limit of 1.3 °C for waters that can potentially flow into the cavity beneath the 79NG ice tongue. This limit is comparable with the observations during FS2016 in the Norske Trough (Figure 4.4).

The cold halocline between 50 m and 100 m in ECCOv4 is very similar to the observations taken during the FS2016 (Figure 4.4). Moreover, it is present every year making it to an constant feature in the Norske Trough. As mentioned above, this has major consequences for the heat loss of AW which is assumed to be rather small toward 79NG.

5.4   1D ISW plume model

5.4.1   The Centreline of the 79NG Ice Tongue - The STANDARD case

The submarine melting is thought to play a key role in the mass balance and stability of the 79Ng. Therefore, it has to be taken into account when estimating the global sea level rise. The freshwater that is released during melting is transported out of the 79N Fjord by the plume. On the continental shelf the enhanced freshwater content in the water column affects the stratification, and therefore how AW may melt sea ice. Further, the EGC flows along the continental shelf carrying this amount of freshwater southward (Figure 2.1) where it reaches three major locations of dense bottom water formation, the Greenland Sea, the Irminger Sea, and the Labrador Sea. The additional freshwater may have effects on the formation process and might even interrupt it leading to consequences for the global thermohaline circulation. Therefore, it is very important to constrain the submarine melt rates and, hence, the freshwater flux as best as possible.

The results for the melt rates are qualitatively comparable with melt rates obtained from Mayer et al. (2000) and Wilson et al. (2017). Wilson et al. (2017) found in general smaller melt rates. Near the grounding line they calculated maximum values of 50 - 60 m yr^{-1}. Downstream from 15 km along the rest of the ice tongue they found melt rates near zero. Mayer et al. (2000) found much smaller maximum melt rates and mean melt rates; near the GL maximum of about 40 m yr^{-1} and mean melting of about 8 m yr^{-1}. The distribution of melting along the ice base is however similar as Mayer et al. (2000) also find significantly less melting downstream of the GL.

Jenkins (2011) performed sensitivity experiments with dimensionless parameters and found an approximate linear relationship for mean melt rates being $\overline{m} = 1 + 0.1X$ near the GL region. This is consistent with the melt rate evolution here, caused by the plume that needs to initiate and accelerate.

The thermal forcing of the AW and the in-situ freezing point, T_a - T_f, is highest at the GL with about 3.3 °C (Figure 4.15c). Wilson et al. (2017) obtained a slightly higher thermal forcing of 3.4 °C. However, results are comparable.

5.4.2 Sensitivity Experiments

Entrainment Coefficient

The entrainment rate $\dot{e}$ is proportional to E_0 (Eq. 3.9). Hence, it plays a key role in determining the melt rates and plume dynamics along the ice base. Lower and higher values are applied to be able to assess how reasonable the choice of the STANDARD value of 1.8×10^{-2} (100 %) is. These experiments gave a good support for this choice.

The parameterization of $\dot{e}$ was suggested by Pedersen (1980). It was tested during laboratory and field studies of dense bottom currents yielding reasonably results, especially for ice base slopes of 0.01 and less (Jenkins, 1991). However, the slopes within the GLZ along the centreline of the 79NG ice tongue are much steeper (Figure 4.13). The mean slope is about 0.03 and the maximum about 0.06. This leads to the conclusion, that using Eq. 3.9 within the GLZ might yield an overestimate in the melting. To overcome this circumstance, the entrainment coefficient 1.8×10^{-2}, half the value used by Jenkins (1991), was applied. Indeed, implementing the 1D ISW plume model with a 200 % ($E_0 = 3.6 \times 10^{-2}$) entrainment coefficient results in highly elevated melt rates everywhere along the ice base, especially within the GLZ and TZ exceeding $100 \, \text{m} \, \text{yr}^{-1}$ (Figure 4.16a, red).

Further, Pedersen (1980) suggests to set E_0 to 7.2×10^{-2} which is 400 % of the STANDARD value. Jenkins (1991) argues that this number is an overestimate because the Coriolis force would sidetrack the plume towards the right in the Northern Hemisphere, thus, toward the South Coast in Nioghalvfjerdsfjorden. The slopes are much more gentle here (Figure 4.13)and, therefore, would lead to a reduced entrainment rate. However, in the 1D ISW plume model, the Coriolis effect is not included (Jenkins, 1991). As a consequence, Jenkins (1991) has chosen half the value stated by Pedersen (1980) to 200% ($E_0 = 3.6 \times 10^{-2}$) of the STANDARD value. Although, the value proposed by Pedersen (1980), 400% of the STANDARD value, was applied to show that the melt rates increase even more than for using 200% ($E_0 = 3.6 \times 10^{-2}$) (Figure 4.16a, green). In a more sophisticated plume model, Straneo and Cenedese (2015) used 722 % of the STANDARD value ($E_0 = 13.0 \times 10^{-2}$) for the entrainment coefficient. This most likely yields

much too high melt rates in the simplified 1D ISW plume model.

Drag Coefficient

A higher drag coefficient C_D slows the plume down and, thus, reduces the melting as less AW is entrained. In contrast, a lower drag accelerates the flow, consequently leading to higher entrainment rates and, hence, elevated melt rates.

The STANDARD value 9.7×10^{-3} (100 %) for the drag coefficient C_D was adopted from Jenkins et al. (2010) and assumed to be a good choice for studying ice-ocean interactions. Jenkins et al. (2010) derived this value from observations of the hydrography and submarine melt rates calculated from radar measurements at the Ronne Ice Shelf as well as values for $\gamma_{T,S}$ suggested by McPhee (1992).

Besides, 25 % of the STANDARD (2.5×10^{-3}) is used for a wide range of applications and was also tested. This value was measured at the coast of England when wind was blowing over grass (Nicholls K. W. (2017), personal communication). Applying this drag coefficient to the model yield higher melt rates everywhere along the ice base compared to the STANDARD (Figure 4.16b, magenta). However, a higher drag for water flowing along the ice base than for air blowing over grass is expected. Because the drag depends on the surface shape and the roughness, both of which are larger for an ice base than for grass. As a conclusion, the suggested value by Jenkins et al. (2010), 9.7×10^{-3} (100 %), was used as a good estimate for the 79NG ice tongue. Moreover, the value was recommended to apply to the 79NG ice tongue (Kimura S. (2017), personal communication).

Subglacial Discharge

A very wide range for the subglacial discharge was applied because it is highly unknown in general, and, in particular, at 79NG (Straneo F. (2017), de Fleurian (2017), personal communication). Values from 1.0×10^{-9} to $8.7 \, \text{m}^2 \, \text{s}^{-1}$ mostly likely cover the majority of possible scenarios. Increasing the subglacial discharge leads to higher mean melt rates. This finding is consistent with sensitivity experiments from Jenkins (2011) applying the 1D ISW plume model to various ice shelves in Antarctica, to Jakobshavn Isbræ, and to LeConte Glacier in Alaska. Further, the response is strongest within the GLZ because the melting is convection-driven in this region (Jenkins, 2011) and, therefore, determined by the subglacial discharge. Downstream, the convection is melt-driven (Jenkins, 2011) and controlled by additional freshwater input due to melting and, hence, less sensitive to variations in the subglacial discharge.

$1.0 \times 10^{-9} \, \text{m}^2 \, \text{s}^{-1}$ is very low and might be applicable for a winter situation where no subglacial discharge is assumed (Straneo et al., 2011). The STANDARD subglacial discharge used,

$1.0 \times 10^{-3}\,\mathrm{m^2\,s^{-1}}$, might be too low as melt rates and plume dynamics (thickness and velocity) remain nearly unaltered. Hence, this value does probably not correspond do a summer situation where a high subglacial discharge is expected (Straneo et al., 2011), and, therefore, not to the hydrography observed in summer 2009 during AS2009. Moreover, it is concluded that the melting and the plume dynamics are not sensitive to a lower limit of the subglacial discharge. The surface runoff obtained by Andersen et al. (2010) at Helheim Glacier of $174\,\mathrm{m^3\,s^{-1}}$ is most likely too low to apply to 79NG. Even though, 79NG is probably subject to less precipitation and colder air temperatures, it drains a much larger area of about $103\,314\,\mathrm{km^2}$ than Helheim Glacier with $48\,140\,\mathrm{km^2}$ (Rignot and Kanagaratnam, 2006). In addition, high geothermal heat fluxes are measured at NEGIS (Fahnestock et al., 2001). Thus, a much larger subglacial discharge is assumed. In this respect, the tenfold surface runoff from Helheim Glacier ($1740\,\mathrm{m^3\,s^{-1}}$) is applied to 79NG as subglacial discharge.

Tidal Flow

The tidal flow is with $1.18\,\mathrm{cm\,s^{-1}}$ too weak to have effects on the melting and plume dynamics. This is concluded from applying no tidal flow yielding the same results as with the tidal flow. As discussed in Section 5.2.2, tides might be low in the cavity because of ice blocking the flow. However, this explanation is speculative at best.

Mortensen et al. (2014) performed a tidal analysis at Godthåbsfjord in West Greenland also using moored current meter measurements. Maximum tidal velocities were associated with the M2 and S2 component and 4 - 5 $\mathrm{cm\,s^{-1}}$ and 1 - 2 $\mathrm{cm\,s^{-1}}$. The tidal flow in the cavity below the 79NG ice tongue is thus low compared to tidal velocities around Greenland.

Turbulent Transfer Coefficients for Heat and Salt

For the STANDARD case γ_T is in the mean about 27 times larger than γ_S. Mcphee et al. (2008) discuss that the ratio ought to be between 35 - 70. Using this, Jenkins et al. (2010) subsequently found values of 1.1×10^{-2} and 3.1×10^{-4} for γ_T and γ_S in combination with the drag coefficient 9.7×10^{-3} and their observations at Ronne Ice Shelf. The constant value 0.6×10^{-2} for $\gamma_{T,S}$ is proposed by McPhee (1992) applicable for sea ice. Applying these constant values yield much higher mean and maximum melt rates (Figure 4.16e and Table 4.4). However, using the more sophisticated velocity dependent formulation for the transfer coefficients in combination with the parameters discussed above yield comparable melt rates and their distribution to Mayer et al. (2000) and Wilson et al. (2017). Moreover, melt rates calculated by Jenkins et al. (2010) are very different as these were obtained form Ronne Ice Shelf. In this regard, the formulation in the STANDARD is believed to be most appropriate for the 79NG ice tongue.

Ice Base

The plume that flows along the south coast of the Nioghalvfjerdsfjorden reaches its level of neutral buoyancy already at about 60 km compared to 75 km and 78 km for the path along the centreline and the north coast (Figure 3.5). A plume initiated at the GL rises and flows along the Coriolis favored side of the fjord (Millgate et al., 2013), here the south coast. On the other hand, Wilson and Straneo (2015) suggest that the plume flows out at the northern terminus of the ice tongue and into Dijmphna Sund. The results of the ITM5 support this to some degree (Section 4.2.1 and 5.2.2). Obviously, the plume might also flow along the steepest gradient of the ice base. However, following this ended in a local maximum because of the noisy ice base. A steep but not the steepest gradient in the ice base was found to go directly from the deepest point at the GL toward the north coast. The plume is believed to flow along the north coast and out into Dimjphna Sund as suggested by Wilson and Straneo (2015). This is supported by Mayer et al. (2000) stating that the buoyant meltwater moves along the largest gradient at the underside of the ice base which is found to be the path along the north coast (Figures 3.5 and 4.14c).

The effect of the slope of the ice base needs further consideration. Near the GL where the ice base is deepest and the slope steepest (Figures 4.13 and 4.14) the highest melt rates are found (Figure 4.16f). This is consistent with results from Wilson et al. (2017) which found a significant correlation between melt rates and ice base slope at 79NG. Because the melt rate depends on the entrainment of AW (Eq. 3.7) and the entrainment rate is parameterized with the slope, higher melting at steeper slopes is expected. However, maximum slopes within the GLZ along the centreline, the north and south coast are about 0.06, 0.13, and 0.03 (Figure 4.13). According to Jenkins (2011), slopes of 0.01 are typical for the GLZ of ice shelves. The slopes for the centreline and the south coast are, thus, relatively gentle.

5.4.3   AW Temperature in the Cavity below the 79NG Ice Tongue

Rift Profile

To investigate the response on the submarine melt rates and the plume dynamics below the 79NG ice tongue to a warming ocean the AW temperature in the cavity was increased (Section 4.4.3). However, this study could also be performed by altering the ocean circulation, tuning it such that it would just transport more warm waters to 79NG instead of increasing its temperature as proposed by Holland et al. (2007).

The submarine melt rates response close to linearly with AW temperature (Figure 4.19). This

finding is comparable to many independent studies for Antarctic ice shelves and floating glaciers, e.g. by Jenkins (1991), Hellmer et al. (1998), and Holland et al. (2007). Jenkins (1991) used the same 1D ISW model, whereas Holland et al. (2007) achieved this result using a 3D ocean general circulation model. The quadratic relation is rooted in the linear dependence of the melt rate to both the velocity and the ocean temperature (Eq. 3.18 and 3.19).

However, melt rates might also be described partly with a quadratic dependence. However, the mean melt rate yields more reasonable results as a linear dependence with AW temperature than a quadratic one as suggested by Jenkins (2011). The dependencies were tested applying an ocean with AW temperature set to zero. As a result, a maximum melt rate of about $44 \, \mathrm{m \, yr^{-1}}$ and a mean melt rate of about $9 \, \mathrm{m \, yr^{-1}}$ were achieved which are well described by the fitted function (Figure 4.19). As the AW temperature is increased, warmer water is entrained with $\dot{e} \, T_a$ (first term on RHS in Eq. 3.7) and interacts with the ice-ocean boundary. This leads to higher melt rates (Figure 4.20a).

According to Jenkins (1991), to be able to explain the plume dynamics in a warming ocean, especially entrainment and melting processes have to be considered. Entrainment of warm and salty water leads to a denser plume. In contrast, due to higher temperatures melting is enhanced (Figure 4.20a). The increased freshwater that results from melting and is evident in the decreasing salinity of the plume (Figure 4.20d), acts to maintain the buoyancy of the plume. Hence, it is concluded that the latter process has a greater influence than the former because of the steady increase in the plume velocity with rising AW temperature (Figure 4.20e). In addition, as the water temperature is continuously increased, more ice is melted whereas the entrainment rate remains constant. The enhanced freshwater amount accelerates the plume (Figure 4.20e). Because the entrainment rate is parameterized with the plume velocity (Eq. 3.9) more entrainment of warm water is expected. This in turn leads to greater melt rates further downstream (Figure 4.20a and Table 4.4).

A 3°C warming of the AW appears unrealistic. Simulated mean and maximum melt rates are much higher than stated by Thomsen et al. (1997), Mayer et al. (2000), and Wilson et al. (2017) (Table 2.1). This was only adopted to obtain the response of melting to a temperature increase. Schaffer et al. (2017) observed an increase in the mean maximum AW temperature in the Norske Trough of 0.5°C. Therefore, the scenario where the AW temperature in the rift was increased by this value 0.5°C seems more realistic. As a result, mean and maximum melt rates increase to $19 \, \mathrm{m \, yr^{-1}}$ compared to $15 \, \mathrm{m \, yr^{-1}}$ in the STANDARD (Figure 4.20a and Table 4.4).

Norske Trough - ECCOv4

The sensitivity of submarine melt rates to AW temperature is once again examined. The range in temperature is dictated from ECCOv4 simulations (Table 4.2). Additionally, the variations in

the presence of AW in the water column are taken into account.

Increasing the AW temperature (warm AW) leads to significantly higher melt rates (Figure 4.22 and Table 4.5). Melt rates remain nearly constant within 50 km when AW is shallower. This is because the entrained AW is not warmer but only closer to the ice base. Further downstream, the base is shallower and, thus, subject to the cold mixed layer and colder AW (Figure 4.14a and 4.21). Shoaling of AW leads then to enhanced melting (Figure 4.22 green, and Table 4.5). Decreasing the AW temperature (cold AW) causes reduced melting. AW that is deeper in the water column affects the melting only slightly along most of the ice tongue. This is because the plume is still entraining AW. Noteworthy changes appear downstream from 35 km where the plume is encompassed by colder water and, thus, melting is reduced. From 50 km and further downstream, the cold mixed layer with temperatures near the in-situ freezing point causes a significant drop in melt rates.

5.4.4   Stability of the 79NG Ice Tongue

The focus here is devoted to the questions addressed of how long it takes for the ice tongue to completely melt down in a warming ocean and how much freshwater is exported to the continental shelf if that is the case. To investigate the first question, mean melting times are estimated as described in Section 5.4.4. In the following, considerations are restricted to the results obtained from ECCOv4 as these are most realistic. The observed warming of $0.5\,°\mathrm{C}$ in both the Norske Trough and Westwind Trough for the period 2000-2016 compared to 1979-1999 (Schaffer et al., 2017) is included in the latter.

The variations in AW temperature and presence in the water column drive melting between $10.2\,\mathrm{m\,yr^{-1}}$ and $19.3\,\mathrm{m\,yr^{-1}}$. In turn, this leads to a complete melt of the ice tongue within $13.2\,\mathrm{yr}$ to $25.0\,\mathrm{yr}$. These results clearly show that the ice tongue of 79NG undergoes rapid thinning. Based on high-resolution satellite imagery, Wilson et al. (2017) predict that the ice tongue will retreat in the future and become ungrounded. They found a total melt flux of $14.2 \pm 1.6\,\mathrm{km^3\,yr^{-1}}$ exceeding the inflow of ice of $10.2 \pm 0.59\,\mathrm{km^3\,yr^{-1}}$.

For the ECCOv4 cold and warm scenario, the freshwater flux ranges between $19.1\,\mathrm{km^3\,yr^{-1}}$ $(0.6\,\mathrm{mSv})$ and $36.1\,\mathrm{km^3\,yr^{-1}}$ $(1.1\,\mathrm{mSv})$. This is as much as about 2 to 3 times more as computed by Wilson et al. (2017). However, despite the model used is very simplified, results are comparable.

The values obtained for the freshwater flux are small compared to the annual freshwater input in the Arctic Ocean of $8\,500\,\mathrm{km^3\,yr^{-1}}$ $(269.3\,\mathrm{mSv})$ (Serreze et al., 2006). However, it is on the same order as freshwater fluxes resulted due to melting at other Greenland glaciers such as Helheim Glacier, Petermann Glacier $(11.7 \pm 1.4\,\mathrm{km^3\,yr^{-1}})$ (Wilson et al., 2017), Jakobshaven Isbræ, and Kanquersal Glacier.

The total freshwater discharge from the GrIS in 2012 was $1\,291 \pm 50\,\text{km}^3\,\text{yr}^{-1}$ ($41 \pm 2\,\text{mSv}$) (Straneo and Cenedese, 2015). In comparison, the estimated range in freshwater input for the 79NG ice tongue is very large. This might rely on the high mean melt rates for example in the standard case of $14.8\,\text{m}\,\text{yr}^{-1}$ compared to $8\,\text{m}\,\text{yr}^{-1}$ obtained by Mayer et al. (2000). Applying this number to Eq. 4.1 yields a freshwater flux of $14.9\,\text{km}^3\,\text{yr}^{-1}$ ($0.47\,\text{mSv}$) which is about half the STANDARD value. Freshwater flowing south acts as barrier for heat flux from AW toward the atmosphere. This might result in cooling dramatically changing the climate in the northern hemisphere. In addition, the enhanced freshwater may affect the sea ice condition and the local hydrography and circulation. Moreover, dense water formation in the Greenland Sea, Irminger Sea, and Labrador Sea might be altered.

It must be pointed out, that the melt rates and corresponding freshwater fluxes are results of a simplified ISW model.

6. Conclusions

Hydrographic data collected during a research cruise to the Fram Strait and the 79NG in August and September 2016 confirm recirculation of warm and salty AW across Fram Strait. Further, the AW flows along the C-shaped trough system on the continental shelf in front of 79NG. Maximum temperatures of $1.8\,^{\circ}\text{C}$ are found at depth in the Norske Trough in front of the 79NG. AW finally enters the cavity below the 79NG ice tongue via the main front in the east. This is concluded because profiles in the cavity and in the Norske Trough are similar. Moreover, a shallow sill at the mouth of a neighbored fjord in the north restricts the exchange of AW between the northern part of the trough system and the cavity. Large differences in water properties at depth down and upstream of the sill support this.

AW as warm as $1.0\,^{\circ}\text{C}$ is found in CTD profiles taken in a rift on the ice tongue during a research cruise in September 2009. AW reaches the grounding line and drives submarine melting along the ice base. This is confirmed by mixtures of AW and meltwater found in the cavity and in the neighbored fjord.

A 1D Ice Shelf Water plume model simulates mean and maximum malt rates of $15\,\text{m}\,\text{yr}^{-1}$ and 50 - $75\,\text{m}\,\text{yr}^{-1}$. Melt rates are comparable with, yet higher than results from Mayer et al. (2000) and Wilson et al. (2017) which used ice flux divergence calculations. The 1D Ice Shelf water model is simplified as properties are depth-integrated, no across flow variations are considered, and steady state is assumed. Moreover, properties are perfectly mixed and, thus, no stratification is present that would suppress heat fluxes. This explains most likely higher melting. The melt rates are also sensitive to model parameters. The tidal flow calculated from an Ice-Tethered Mooring is very weak and, hence, does not influence the melt rates.

Melt rates increase linearly with AW temperature and are sensitive to subglacial discharge. The temperature dependence on the melting is consistent with Jenkins (2011).

Ocean reanalysis provide a range in AW temperature and layer thickness close to 79NG for the period 1992 - 2015. Corresponding to this range, the 1D Ice Shelf Water plume model simulates mean melt rates between 10 - $19\,\text{m}\,\text{yr}^{-1}$. The resulting freshwater flux to the continental shelf ranges between $19\,\text{km}^3\,\text{yr}^{-1}$ ($0.6\,\text{mSv}$) and $36\,\text{km}^3\,\text{yr}^{-1}$ ($1.1\,\text{mSv}$). Compared to the total freshwater flux of the Greenland Ice Sheet, $3\,200 \pm 358\,\text{km}^3$ since 1995 (Bamber et al., 2012), this is

quite large, about 10 - 19 %.

Measurements from the mooring suggest the major inflow of AW into the cavity at 250 m and 370 m over a 30 day period. Over subsequent 60 days, the outflow is directed toward east at 165 m, toward northeast at 250 m, and toward southeast at 370 m. This is partly consistent with Wilson and Straneo (2015) and Schaffer et al. (2017). The velocity of the flow is between $5\,\mathrm{cm\,s^{-1}}$ - $10\,\mathrm{cm\,s^{-1}}$. A boundary current in the trough system found by Schaffer et al. (2017) has similar velocities.

The upper range in subglacial discharge applied in this study, is applied from surface runoff values at Helheim Glacier multiplied by the factor 10. It is fair to say that this is a rather rough estimate because 79NG is probably subject to colder air temperatures and less precipitation. However, the range used is believed to cover realistic scenarios. In the future, the value for the subglacial discharge might be constrained. An automatic weather station monitoring meteoro-logical parameters was recently installed at the neighbored Zachariæ Isstrøm (Khan A. (2017), personal communication). Using a surface-energy-balance model, the total surface runoff can be calculated as was done for Helheim Glacier by Andersen et al. (2010). Subsequently, this quantity was used for the subglacial discharge. It would be delightful and an important step to apply a similar method for 79NG. And to further constrain the submarine melt rates and, corresponding to these, the freshwater that is released to the continental shelf.

The CTD profile taken in the rift is assumed to be representative for the whole water column. However, it was taken close to the northern front of 79NG and, thus, far away from the ground-ing line. To further understand the processes, first of all the submarine melting, measurements of the water properties close or closer to the grounding line are essential. It could be achieved by sending an autonomous underwater vehicle into the cavity or by drilling a hole trough the ice tongue (similar to EGRIP).

Submarine melt rates of the 79NG have been examined here based on new observations of hydrography and ocean currents, an updated ocean reanalysis, and a 1D Ice Shelf Water plume model. The sensitivity of the model has been tested, and calculated melt rates are in the higher range compared to earlier studies. Our understanding of ice-ocean processes on the narrow and complex East Greenland shelf has thus been improved, and a clear influence of AW temperature is documented on the submarine melt rates.

7. Bibliography

Andersen, M. L., T. B. Larsen, M. Nettles, P. Elosegui, D. van As, G. S. Hamilton, L. A. Stearns, J. L. Davis, A. P. Ahlstrøm, J. de Juan, G. Ekström, L. Stenseng, S. A. Khan, R. Forsberg, and D. Dahl-Jensen (2010). Spatial and temporal melt variability at helheim glacier, east greenland, and its effect on ice dynamics. *Journal of Geophysical Research: Earth Surface 115*.

Arndt, J. E., W. Jokat, B. Dorschel, R. Myklebust, J. A. Dowdeswell, and J. Evans (2015). A new bathymetry of the northeast greenland continental shelf: Constraints on glacial and other processes: New bathymetric model for ne greenland. *Geochemistry, Geophysics, Geosystems 16*(10), 3733–3753.

Aure, J., J. Molvær, and A. Stigebrandt (1996). Observations of inshore water exchange forced by a fluctuating offshore density field. *Marine Pollution Bulletin 33*(1), 112–119.

Bamber, J., M. Den Broeke, J. Ettema, J. Lenaerts, and E. Rignot (2012). Recent large increases in freshwater fluxes from greenland into the north atlantic. *Geophysical Research Letters 39*(19).

Bamber, J. L., J. A. Griggs, R. T. W. L. Hurkmans, J. A. Dowdeswell, S. P. Gogineni, I. Howat, J. Mouginot, J. Paden, S. Palmer, E. Rignot, and D. Steinhage (2013). A new bed elevation dataset for greenland. *The Cryosphere 7*(2), 499.

Benn, D. I. and D. J. A. Evans (2010). *Glaciers glaciation* (2nd ed. ed.). London: Hodder Education.

Beszczynska-Möller, A., E. Fahrbach, U. Schauer, and E. Hansen (2012). Variability in atlantic water temperature and transport at the entrance to the arctic ocean, 1997–2010. *ICES Journal of Marine Science 69*(5), 852–863.

Cenedese, C. and P. F. Linden (2014). Entrainment in two coalescing axisymmetric turbulent plumes. *752*.

Chu, V. W., L. C. Smith, A. K. Rennermalm, R. R. Forster, J. E. Box, and N. Reeh (2009). Sediment plume response to surface melting and supraglacial lake drainages on the greenland ice sheet. *Journal of Glaciology 55*(194), 1072–1082.

Church, J. A., N. J. White, L. F. Konikow, C. M. Domingues, J. G. Cogley, E. Rignot, J. M. Gregory, M. R. Van Den Broeke, A. J. Monaghan, and I. Velicogna (2011). Revisiting the earth's sea-level and energy budgets from 1961 to 2008. *Geophysical Research Letters 38*(18).

Das, S. B., I. Joughin, M. D. Behn, I. M. Howat, M. A. King, D. Lizarralde, and M. P. Bhatia (2008). Fracture propagation to the base of the greenland ice sheet during supraglacial lake drainage. *Science (New York, N.Y.) 320*(5877), 778.

De Steur, L., E. Hansen, C. Mauritzen, A. Beszczynska-Möller, and E. Fahrbach (2014). Impact of recirculation on the east greenland current in fram strait: Results from moored current meter measurements between 1997 and 2009. *Deep - Sea Research 92*, 26.

Depoorter, M. A., J. L. Bamber, J. A. Griggs, J. T. M. Lenaerts, S. R. M. Ligtenberg, M. R. V. D. Broeke, and G. Moholdt (2013). Calving fluxes and basal melt rates of antarctic ice shelves. *Nature 502*(7469), 89.

Enderlin, E. M., I. M. Howat, S. Jeong, M. Noh, J. H. Angelen, and M. R. Broeke (2014). An improved mass budget for the greenland ice sheet. *Geophysical Research Letters 41*(3), 866–872.

Fahnestock, M., R. Bindschadler, R. Kwok, and K. Jezek (1993). Greenland ice sheet surface properties and ice dynamics from ers-1 sar imagery. *Science 262*(5139), 1530–1534.

Fahnestock, M. A., I. Joughin, T. A. Scambos, R. Kwok, W. B. Krabill, and S. Gogineni (2001). Ice-stream-related patterns of ice flow in the interior of northeast greenland. *Journal of Geophysical Research: Atmospheres 106*(D24), 34035–34045.

Forget, G., J. M. Campin, P. Heimbach, C. N. Hill, R. M. Ponte, and C. Wunsch (2015). Ecco version 4: an integrated framework for non-linear inverse modeling and global ocean state estimation. *Geoscientific Model Development 8*(10), 3071.

Gade, H. G. (1979). Melting of ice in sea water: A primitive model with application to the antarctic ice shelf and icebergs. *Journal of Physical Oceanography 9*(1), 189–198.

Hattermann, T., P. E. Isachsen, W. Appen, J. Albretsen, and A. Sundfjord (2016). Eddy driven recirculation of atlantic water in fram strait. *Geophysical Research Letters 43*(7), 3406–3414.

Hellmer, H., S. S. Jacobs, and A. Jenkins (1998). Oceanic erosion of a floating antarctic glacier in the amundsen sea. *Ocean, Ice, and Atmosphere: Interactions at the Antarctic continental margin (S Jacobs, R Weiss, eds) Antarctic Research Series, AGU, Washington DC, USA 75*, 319–339.

Holland, D. and A. Jenkins (1999). Modeling thermodynamic ice-ocean interactions at the base of an ice shelf. *Journal of Physical Oceanography 29*(8), 1787–1800.

Holland, P. R., A. Jenkins, and D. M. Holland (2007). The response of ice shelf basal melting to variations in ocean temperature. *Journal of Climate 21*(11), 2558–2572.

Hátún, H., A. B. Sandø, H. Drange, B. Hansen, and H. Valdimarsson (2005). Influence of the atlantic subpolar gyre on the thermohaline circulation. *Science 309*(5742), 1841–1844.

Jackson, H. R., F. Straneo, and A. D. Sutherland (2014). Externally forced fluctuations in ocean temperature at greenland glaciers in non-summer months. *Nature Geoscience*.

Jenkins, A. (1991). A one-dimensional model of ice shelf-ocean interaction. *Journal of Geophysical Research: Oceans 96*(C11), 20671–20677.

Jenkins, A. (2011). Convection-driven melting near the grounding lines of ice shelves and tidewater glaciers. *Journal of Physical Oceanography 41*(12), 2279–2294.

Jenkins, A. and A. Bombosch (1995). Modeling the effects of frazil ice crystals on the dynamics and thermodynamics of ice shelf water plumes. *Journal of Geophysical Research: Oceans 100*(C4), 6967–6981.

Jenkins, A., K. Nicholls, and H. Corr (2010). Observation and parameterization of ablation at the base of ronne ice shelf, antarctica. *Journal of Physical Oceanography 40*(10), 2298–2312.

Jung-Rothenhäusler, F. (1998). Fernerkundungs- und gis-studien in nordostgrönland. *Berichte zur Polarforschung 280*, 1–161.

Kader, B. A. and A. M. Yaglom (1972). Heat and mass transfer laws for fully turbulent wall flows. *International Journal of Heat and Mass Transfer 15*(12), 2329–2351.

Kader, B. A. and A. M. Yaglom (1977). Turbulent heat and mass transfer from a wall with parallel roughness ridges. *International Journal of Heat and Mass Transfer 20*(4), 345–357.

Kimura, S., P. Holland, A. Jenkins, and M. Piggott (2014). The effect of meltwater plumes on the melting of a vertical glacier face. *Journal of Physical Oceanography 44*(12), 3099–3117.

Krishfield, R., J. Toole, A. Proshutinsky, and M.-L. Timmermans (2008). Automated ice-tethered profilers for seawater observations under pack ice in all seasons. *Journal of Atmospheric and Oceanic Technology 25*(11), 2091–2105.

Mayer, C., N. Reeh, F. Jung-Rothenhäusler, P. Huybrechts, and H. Oerter (2000). The subglacial cavity and implied dynamics under nioghalvfjerdsfjorden glacier, ne greenland. *Geophysical Research Letters 27*(15), 2289–2292.

McPhee, M. (1992). Turbulent heat flux in the upper ocean under sea ice. *Journal of Geophysical Research: Oceans 97*(C4), 5365–5379.

Mcphee, M. G., J. H. Morison, and F. Nilsen (2008, June). Revisiting heat and salt exchange at the ice-ocean interface: Ocean flux and modeling considerations. *Journal of Geophysical Research: Oceans 113*(C6).

Millgate, T., P. R. Holland, A. Jenkins, and H. L. Johnson (2013). The effect of basal channels on oceanic ice-shelf melting. *Journal of Geophysical Research: Oceans 118*(12), 6951–6964.

Morlighem, M., E. Rignot, J. Mouginot, H. Seroussi, and E. Larour (2014). Deeply incised submarine glacial valleys beneath the greenland ice sheet. *Nature Geoscience 7*(6), 418.

Mortensen, J., J. Bendtsen, K. Lennert, and S. Rysgaard (2014). Seasonal variability of the circulation system in a west greenland tidewater outlet glacier fjord, godthåbsfjord (64n). *Journal of Geophysical Research: Earth Surface 119*(12), 2591–2603.

Mouginot, J., E. Rignot, B. Scheuchl, I. Fenty, A. Khazendar, M. Morlighem, A. Buzzi, and J. Paden (2015). Fast retreat of zachariæ isstrøm, northeast greenland. *Science (New York, N.Y.) 350*(6266), 1357.

Nortek AS, m. (2013). Aquadopp current meter - the most versatile 3d ocean current meter available.

Nurser, A. J. G. and S. Bacon (2014, November). The rossby radius in the arctic ocean. *Ocean Science 10*(6).

Onarheim, I. H., L. H. Smedsrud, R. Ingvaldsen, and F. Nilsen (2014). Loss of sea ice during winter north of svalbard. *Tellus. Series A, Dynamic meteorology and oceanography 66*(23933).

Orvik, K. A. and P. Niiler (2002). Major pathways of atlantic water in the northern north atlantic and nordic seas toward arctic. *Geophysical Research Letters 29*(19).

Pawlowicz, R., B. Beardsley, and S. Lentz (2002). Classical tidal harmonic analysis including error estimates in matlab using ttide. *Computers and Geosciences 28*(8), 929–937.

Pedersen, F. B. (1980). Dense bottom currents in rotating ocean. *Journal of the Hydraulics Division-Asce 106*(8), 1291–1308.

Pugh, D. and P. Woodworth (2014). *Sea-level science : understanding tides, surges, tsunamis and mean sea-level changes*. Cambridge University Press.

Reeh, N., C. Mayer, H. Miller, H. H. Thomsen, and A. Weidick (1999). Present and past climate control on fjord glaciations in greenland: Implications for ird-deposition in the sea. *Geophysical Research Letters 26*(8), 1039–1042.

Reeh, N., H. H. Thomsen, A. K. Higgins, and A. Weidick (2001). Sea ice and the stability of north and northeast greenland floating glaciers. *Annals of Glaciology 33*, 474–480.

Rignot, E. and P. Kanagaratnam (2006). Changes in the velocity structure of the greenland ice sheet. *Science (New York, N.Y.) 311*(5763), 986.

Rignot, E. and J. Mouginot (2012). Ice flow in greenland for the international polar year 20082009. *Geophysical Research Letters 39*(11).

Årthun, M. and T. Eldevik (2016). On anomalous ocean heat transport toward the arctic and associated climate predictability. *Journal of Climate 29*(2), 689–704.

Rudels, B., E. Fahrbach, J. Meincke, G. Budéus, and P. Eriksson (2002). The east greenland current and its contribution to the denmark strait overflow. *ICES Journal of Marine Science 59*(6), 1133–1154.

Rudels, B., R. Meyer, E. Fahrbach, V. Ivanov, S. Østerhus, D. Quadfasel, U. Schauer, V. Tverberg, and R. Woodgate (2000). Water mass distribution in fram strait and over the yermak plateau in summer 1997. *Annales Geophysicae 18*(6), 687–705.

Schaffer, J., R. Timmermann, J. E. Arndt, S. S. Kristensen, C. Mayer, M. Morlighem, and D. Steinhage (2016). A global high-resolution data set of ice sheet topography, cavity geometry and ocean bathymetry. *Earth System Science Data Discussions*, 1–21.

Schaffer, J., W.-J. Von Appen, P. A. Dodd, C. Hofstede, C. Mayer, L. de Steur, and T. Kanzow (2017). Warm water pathways toward nioghalvfjerdsfjorden glacier, northeast greenland. *Journal of Geophysical Research: Oceans*.

Schauer, U., E. Fahrbach, S. Osterhus, and G. Rohardt (2004). Arctic warming through the fram strait: Oceanic heat transport from 3 years of measurements. *Journal of Geophysical Research: Oceans 109*(C6).

Sciascia, R., C. Cenedese, D. Nicolì, P. Heimbach, and F. Straneo (2014). Impact of periodic intermediary flows on submarine melting of a greenland glacier. *Journal of Geophysical Research: Oceans 119*(10), 7078–7098.

Sciascia, R., F. Straneo, C. Cenedese, and P. Heimbach (2013). Seasonal variability of submarine melt rate and circulation in an east greenland fjord. *Journal of Geophysical Research: Oceans 118*(5), 2492–2506.

Sea-Bird Electronics, I. (2015). Sbe 9plus ctd user manual: For use with sbe 11plus v2 deck unit or sbe 17plus v2 searam memory and auto fire module. pp. 73.

Serreze, M. C., A. P. Barrett, A. G. Slater, R. A. Woodgate, K. Aagaard, R. B. Lammers, M. Steele, R. Moritz, M. Meredith, and C. M. Lee (2006). The large-scale freshwater cycle of the arctic. *Journal of Geophysical Research: Oceans 111*(C11).

Shepherd, A., E. R. Ivins, G. A, V. R. Barletta, M. J. Bentley, S. Bettadpur, K. H. Briggs, D. H. Bromwich, R. Forsberg, N. Galin, M. Horwath, S. Jacobs, I. Joughin, M. A. King, J. T. M. Lenaerts, J. Li, S. R. M. Ligtenberg, A. Luckman, S. B. Luthcke, M. McMillan, R. Meister, G. Milne, J. Mouginot, A. Muir, J. P. Nicolas, J. Paden, A. J. Payne, H. Pritchard, E. Rignot, H. Rott, L. S. Sørensen, T. A. Scambos, B. Scheuchl, E. J. O. Schrama, B. Smith, A. V. Sundal, J. H. van Angelen, W. J. van de Berg, M. R. van Den Broeke, D. G. Vaughan, I. Velicogna, J. Wahr, P. L. Whitehouse, D. J. Wingham, D. Yi, D. Young, and H. J. Zwally (2012). A reconciled estimate of ice-sheet mass balance. *Science (New York, N.Y.) 338*(6111), 1183.

Skogseth, R., M. G. McPhee, F. Nilsen, and L. H. Smedsrud (2013). Creation and tidal advection of a cold salinity front in storfjorden: 1. polynya dynamics. *Journal of Geophysical Research: Oceans 118*(7), 3278–3291.

Smedsrud, L. H. and A. Jenkins (2004). Frazil ice formation in ice shelf water plume.

Stigebrandt, A. (2012). *Hydrodynamics and Circulation of Fjords*, pp. 327–344. Dordrecht: Springer Netherlands.

Straneo, F. and C. Cenedese (2015). The dynamics of greenland's glacial fjords and their role in climate. *Annual Review of Marine Science 7*(1), 89–112.

Straneo, F., R. G. Curry, D. A. Sutherland, G. S. Hamilton, C. Cenedese, K. Våge, and L. A. Stearns (2011). Impact of fjord dynamics and glacial runoff on the circulation near helheim glacier. *Nature Geoscience 4*(5), 322.

Straneo, F. and P. Heimbach (2013). North atlantic warming and the retreat of greenland's outlet glaciers. *Nature 504*(7478), 36.

Straneo, F., D. A. Sutherland, D. M. Holland, C. Gladish, G. Hamilton, H. L. Johnson, E. Rignot, Y. Xu, and M. Koppes (2012). Characteristics of ocean waters reaching greenland's glaciers. *Annals of Glaciology 53*(60), 202–210.

Thomas, R., E. Frederick, W. Krabill, S. Manizade, and C. Martin (2009). Recent changes on greenland outlet glaciers. *Journal of Glaciology 55*(189), 147–162.

Thomsen, H. H., N. Reeh, O. B. Olesen, C. E. Bøggild, W. Starzer, A. Weidick, and A. K. Higgins (1997). The nioghalvfjerdsfjorden glacier project, north-east greenland: a study of ice sheet response to climatic change. *Geology of Greenland Bulletin 176*, 95–103.

Timmermann, R., A. Brocq, T. Deen, E. Domack, P. Dutrieux, B. Galton-Fenzi, H. Hellmer, A. Humbert, D. Jansen, A. Jenkins, A. Lambrecht, K. Makinson, F. Nieder Jasper, F. Nitsche, O. Nøst, L. Smedsrud, and W. Smith (2010). A consistent data set of antarctic ice sheet topography, cavity geometry, and global bathymetry. *Earth System Science Data 2*(2), 261.

Toole, J., R. Krishfield, A. Proshutinsky, C. Ashjian, K. Doherty, D. Frye, T. Hammar, J. Kemp, D. Peters, M.-L. Timmermans, K. von der Heydt, G. Packard, and T. Shanahan (2006). Ice-tethered profilers sample the upper arctic ocean. *Eos, Transactions American Geophysical Union 87*(41), 434–438.

Warrick, R. A., C. Le Provost, M. F. Meier, J. Oerlemans, and P. L. Woodworth (1996). Climate change 1995: The science of climate change. *Contribution of working group I to the second assessment report of the Intergovernmental Panel on Climate Change. eds: Houghton, et al. Cambridge University Press 572.*

Weatherall, P., K. M. Marks, M. Jakobsson, T. Schmitt, S. Tani, J. E. Arndt, M. Rovere, D. Chayes, V. Ferrini, and R. Wigley (2015). A new digital bathymetric model of the world's oceans. *Earth and Space Science 2*(8), 331–345.

Wilson, N., F. Straneo, and P. Heimbach (2017). Submarine melt rates and mass balance for greenland's remaining ice tongues. *The Cryosphere Discuss. 2017*, 1–17.

Wilson, N. J. and F. Straneo (2015). Water exchange between the continental shelf and the cavity beneath nioghalvfjerdsbrae (79 north glacier). *Geophys. Res. Lett. 42*(18), 7648–7654.

Xu, Y., E. Rignot, I. Fenty, D. Menemenlis, and M. M. Flexas (2013). Subaqueous melting of store glacier, west greenland from three-dimensional, high-resolution numerical modeling and ocean observations. *Geophysical Research Letters 40*(17), 4648–4653.